



Department of Aerospace Engineering
University of Cincinnati

AN INVESTIGATION OF VISCOUS LOSSES IN
RADIAL INFLOW TURBINE NOZZLES

BY

I. KHALIL, W. TABAKOFF AND A. HAMED

(NASA-CR-137942) AN INVESTIGATION OF
VISCOUS LOSSES IN RADIAL INFLOW TURBINE
NOZZLES Interim Report (Cincinnati Univ.)
87 p HC A05/MF A01 CSCL 20D

N77-17394

Unclass.

G3/34 14987

Supported by:

NATIONAL AERONAUTICS AND SPACE ADMINISTRATION

Ames Research Center

Contract No. NAS2-7850

REPRODUCED BY
NATIONAL TECHNICAL
INFORMATION SERVICE
U.S. DEPARTMENT OF COMMERCE
SPRINGFIELD, VA. 22161

An Investigation of Viscous Losses in Radial Inflow Turbine Nozzles

I. Khalil, et al

University of Cincinnati
Cincinnati, Ohio

NOTICE

THIS DOCUMENT HAS BEEN REPRODUCED FROM THE BEST COPY FURNISHED US BY THE SPONSORING AGENCY. ALTHOUGH IT IS RECOGNIZED THAT CERTAIN PORTIONS ARE ILLEGIBLE, IT IS BEING RELEASED IN THE INTEREST OF MAKING AVAILABLE AS MUCH INFORMATION AS POSSIBLE.

1 Report No NASA CR 137942		2 Government Accession No		3 Recipient's Catalog No	
4 Title and Subtitle An Investigation of Viscous Losses in Radial Inflow Nozzles				5 Report Date	
				6 Performing Organization Code	
7 Author(s) I. Khalil, W. Tabakoff and A. Hamed				8 Performing Organization Report No	
				10 Work Unit No	
9 Performing Organization Name and Address Department of Aerospace Engineering & Applied Mechanics University of Cincinnati Cincinnati, Ohio 45221				11 Contract or Grant No NAS2-7850	
				13 Type of Report and Period Covered Contractor Report	
12 Sponsoring Agency Name and Address National Aeronautics & Space Administration Washington, D.C. 20546, and U.S. Army Air Mobility Research & Development Lab. Moffett Field, California 94035				14 Sponsoring Agency Code	
15 Supplementary Notes Interim Report. Project Manager, LTC Dwain Moentmann, U.S. Army Air Mobility Research and Development Laboratory, Ames Research Center, Moffett Field, California 94035.					
16 Abstract A theoretical model is developed to predict losses in radial inflow turbine nozzles. The analysis is presented in two parts. The first one evaluates the losses which occur across the vane region of the nozzle, while the second part deals with the losses which take place in the vaneless field. It is concluded that the losses in a radial nozzle would not be greatly affected by the addition of a large vaneless space.					
17 Key Words (Suggested by Author(s)) Turbomachinery Losses Radial Turbine				18 Distribution Statement Unclassified - unlimited	
19 Security Classif (or this report) Unclassified		20 Security Classif (or this page) Unclassified		21 No of Pages 83	
				22 Price*	

* For sale by the National Technical Information Service Springfield Virginia 22161

AN INVESTIGATION OF VISCOUS LOSSES IN
RADIAL INFLOW TURBINE NOZZLES

by

I. Khalil, W. Tabakoff and A. Hamed

Supported by:

NATIONAL AERONAUTICS AND SPACE ADMINISTRATION

Ames Research Center

Contract No. NAS2-7850

TABLE OF CONTENTS

	<u>Page</u>
SUMMARY	1
INTRODUCTION	2
PART ONE: FRICTION AND MIXING LOSSES IN THE VANED REGION	4
Analysis	4
Sudden Mixing Analysis	8
Results and Discussion	10
PART TWO: FRICTION LOSSES IN THE VANELESS FIELD	13
The Three Dimensional Flow In The End Walls Boundary Layer	14
Calculation Of The Main Flow Properties In The Vaneless Field	17
Formulation Of Relations Describing The Variation of Flow Properties Along The Flow Path	19
Procedure For The Numerical Solutions of Governing Equations	23
Evaluation of Loss Coefficients Across the Vaneless Field	25
Results and Discussion	27
CONCLUSIONS	30
REFERENCES	31
NOMENCLATURE	33
FIGURES	36
APPENDIX A - Formulation of Relations Between Integral Quantities and Boundary Layer Characteristic Parameters	67

SUMMARY

A theoretical model is developed to predict losses in radial inflow turbine nozzles. The analysis is presented in two parts. The first one evaluates the losses which occur across the vaned region of the nozzle, while the second part deals with the losses which take place in the vaneless field.

In the vaned region, equations are derived to relate the losses to the boundary layer characteristic parameters on the vane surfaces and over the two end walls. The effects of vanes geometry, flow conditions and boundary layer characteristic parameters, at exit from the nozzle channel, on the level of losses are investigated. Results indicate that the portion of the losses incurred due to the end walls boundary layer may be significant especially when these boundary layers are characterized by a strong cross flow component.

In the vaneless field, the governing equations for the flow are formulated using the assumptions of the first order boundary layer theory. The viscous losses are evaluated through the introduction of a wall shear stress that takes into account the effects of the three dimensional end walls boundary layer. The resulting governing equations are solved numerically and the effects of some operating conditions and the nozzle geometry are studied.

It is concluded that the losses in the vaneless region may be looked at as a secondary factor in the determination of the overall efficiency of the turbine nozzle assembly.

INTRODUCTION

In recent studies dealing with the flow patterns in radial inflow turbines, the flow is assumed to be isentropic with a viscous loss coefficient introduced to account for actual flow effects. The studies of Ref. [1, 2] were based on the assumption that the viscous losses within the flow passages are proportional to the average kinetic energy in the passage. A proportionality constant was chosen such that the viscous losses matched the values determined from the experimental results. Other studies [3], estimate losses using approximations based upon flat plate or pipe-flow analogies. Although in the past, approximate and semi-empirical solutions for the losses have been adequate for engineering purposes, the present sophistication of fluid machinery demands a closer view of the problem.

The real flow in the radial type machines is very complex because it is viscous, unsteady and three dimensional. An insight into the real flow processes can be achieved by breaking the complex flow pattern into several regions. Existing flow theories can then be used to obtain a solution to the flow together with some reasonable simplifying assumptions in each of these regions. Following this approach, and referring to Figure 1, the flow field in a radial turbine nozzle can be divided into the following subdomains:

- a. The passage between the blades, in which the flow is partially guided.
- b. The throat region where the flow is directed from the closed channel conditions to the vane outlet free conditions.
- c. The region just at the exit of the channel, which will be referred to as the zone of rapid adjustment. In this region, a considerable portion of the overall stator losses take place.
- d. The vaneless space region.

In the present work a theoretical model is developed to predict the losses in the flow regions mentioned above. The

investigation is presented in two parts. The first part deals with the flow losses in the vaned regions and the second part with the losses in vaneless field. In the first part, the friction losses which result from the boundary layers development along the vane surfaces and over the end walls are considered. Mixing losses, due to the nonuniform flow conditions at exit from the vaned region, are also taken into account. The analysis establishes relations that provide the description of the flow properties at the entrance to the vaneless field, in terms of the boundary layer characteristic parameters over the flow surfaces. From these relations the various factors influencing the losses in the vaned region are determined, and their relative effects are evaluated.

In the second part of this study, the viscous flow in the vaneless field is analyzed. The influence of the three dimensional end wall boundary layers on the steady nozzle flow is taken into consideration. The effect of the nozzle geometry and the flow characteristics on the losses in the vaneless region are determined.

Under the stipulation of the developed model, the overall losses between the inlet of the radial nozzles and the impeller periphery may be considered as the sum of friction and mixing losses in the vaned region, plus the friction losses in the vaneless field. For an actual expansion process, the mechanism of all these losses are coupled. The model adopted however, provides a simple guide for better understanding and estimating radial nozzles loss data.

PART I

FRICITION AND MIXING LOSSES IN THE VANED REGION

ANALYSIS

The purpose of the radial turbine nozzles is to convert the pressure energy into flow kinetics energy. In the vaned region, a torque is imposed on the flow by means of the vanes following the scroll and hence, the angular momentum of the fluid changes more rapidly than in the vaneless field. The design objective remains the same, however, to achieve the highest possible efficiency. The thin untwisted vanes forming the nozzle channels, are arranged around the circumferential direction, with equal spacing and orientation (Fig. 1). In order to maintain a sufficiently high vane chord Reynolds number, the length to width ratio of the passages between the vanes ranges between 1 and 3, and the vanes aspect ratio is often less than 1.

As the flow passes through the vaned region, it suffers a loss in total pressure and kinetic energy. This may be attributed to the decrease in the flow momentum within the boundary layers, which are developed over the flow surfaces, and to their mixing with the main flow. It can be seen from Figure 2, which is taken from Reference [4], that the magnitude and the direction of the flow velocity, as well as the other flow properties are nonuniform in both the axial and the tangential directions at nozzle inlet. These nonuniform flow conditions which constitute an additional source of the losses are caused by the three dimensional flow behavior in the scroll.

Another possible mechanism that contributes to the losses is the secondary flow, which tends to move the boundary layer material across the channel from the pressure side of a vane to the suction side of the adjacent vane, as shown in Figure 3.

To obtain an exact solution of the real flow in the vaned region, with all the aforementioned effects included, would be impractical. These factors can be examined separately to determine how they affect the losses in the radial turbines. The work presented here is a study of the losses, which result from boundary layer development along the vanes surfaces and over the end walls.

Referring to Figure 1, the total pressure of the flow entering the nozzle at radius r_0 , is P_{t0} . As it leaves the nozzle at r_1 , there is a variation in the flow properties in both the circumferential and the axial directions due to the axial directions due to the boundary layer development over the end walls and the vane surfaces. It is assumed that due to the mixing effects, the properties of the air stream are homogeneous at station 2, downstream from the vanes exit. The loss coefficients, expressed in terms of the total pressures at stations 0 and 2, will hence represent the overall losses across the vaned region, resulting from the friction and mixing mechanisms. The pressure and enthalpy loss coefficients are given respectively by the following relations:

$$\bar{Y} = \frac{1 - P_{t2}/P_{t0}}{1 - P_2/P_{t0}} \quad , \quad \bar{\zeta} = \frac{(P_{t0}/P_{t2})^{(\gamma-1)/\gamma} - 1}{(P_{t0}/P_2)^{(\gamma-1)/\gamma} - 1} \quad (1)$$

In order to determine these coefficients in terms of the main flow properties and the boundary layer parameters at station 1, the equations governing the flow motion between stations 1 and 2 are derived in the following sections.

The Governing Equations

Consider a control volume with an axial depth, $2b$, equal to the nozzle depth, that extends circumferentially between two consecutive mid-channel stream surfaces as shown in Figure 4. The equations of conservation of mass, energy, angular momentum and linear momentum in the Y - Y direction are written under the following assumptions:

- a. The total temperature is constant during the expansion and the mixing processes.
- b. The static pressure is independent of z and θ at station 1.
- c. The flow pattern is similar in all the flow channels, between two neighboring vanes of angular spacing equal to $2\pi/Z$.

The Conservation of Mass

For steady flow conditions, the following continuity equation applies for the control volume of Figure 4:

$$\int_{-b}^{+b} \int_{-\pi/Z}^{+\pi/Z} (\rho V r \cos \alpha)_1 d\theta dz = \int_{-b}^{+b} \int_{-\pi/Z}^{+\pi/Z} \rho_2 V_2 r_2 \cos \alpha_2 d\theta dz \quad (2)$$

If the left hand side of the above equation is expressed in terms of the boundary layer characteristic parameters at station 1 by using equation (A24) of Appendix A, the following relation is obtained:

$$(\rho V)_{\infty_1} r_1 \cos \alpha_1 [1 - \delta^* - \delta_{te} - \lambda \theta^{**}] = \rho_2 V_2 r_2 \cos \alpha_2 \quad (3)$$

In the above equation, the subscript ∞_1 refers to the conditions outside the boundary layer regions at exit from the nozzle channels, α_1 is the angle between the velocity vector and the inward radial direction, δ^* is the total nondimensional displacement thickness over the vane surfaces at station 1 and δ_{te} denotes the trailing edge blocking factor. θ^{**} is the streamwise total nondimensional momentum thickness over the two end walls at station 1, and λ is a parameter given by Equation (A23) that depends on the end wall boundary layer profiles.

Conservation of Angular Momentum

If the equation of conservation of angular momentum is written for the same control volume, the following expression is obtained:

$$\int_{-b}^{+b} \int_{-\pi/Z}^{+\pi/Z} \rho_2 r_2^2 V_2^2 \cos \alpha_2 \sin \alpha_2 d\theta dz - \int_{-b}^{+b} \int_{-\pi/Z}^{+\pi/Z} (\rho r^2 V^2 \cos \alpha \sin \alpha)_1 d\theta dz = 0 \quad (4)$$

Using Equation (A23) of Appendix A, Equation (3) can be written as follows:

$$\rho_2 V_2^2 \cos \alpha_2 \sin \alpha_2 r_2^2 - (\rho V^2)_{\infty_1} \cos \alpha_1 \sin \alpha_1 r_1^2 [1 - \delta^* - \delta_{te} - \theta^* - \eta \theta^{**}] = 0 \quad (5)$$

In the above equation, θ^* is the total nondimensional momentum thickness over the vane surfaces and η is a parameter to be determined from the end wall boundary layer velocity profile at station 1, using Eq. (A31).

Conservation of Linear Momentum

Referring to Fig. 4 the momentum equation in the Y-Y direction is expressed as follows:

$$\begin{aligned}
 & - \int_{-b}^{+b} \int_{-\pi/Z}^{+\pi/Z} [\rho V^2 \cos \alpha \, r \cos(\alpha + \theta)]_1 \, d\theta dz \\
 & + \int_{-b}^{+b} \int_{-\pi/Z}^{+\pi/Z} \rho_2 V_2^2 r_2 \cos \alpha_2 \cos(\alpha_2 - \beta + \theta) \, d\theta dz \\
 & = \int_{-b}^{+b} \int_{-\pi/Z}^{+\pi/Z} p_1 r_1 \cos \theta \, d\theta dz - \int_{-b}^{+b} \int_{-\pi/Z}^{+\pi/Z} p_2 r_2 \cos(\beta - \theta) \, d\theta dz + Q + C
 \end{aligned} \tag{6}$$

The first and second terms in the right hand side of Equation (6) represent the component of pressure forces acting on the surfaces CD and FE of Fig. 4, in the Y-Y direction. The next term Q, is the resultant of the pressure forces on the two mid channel stream surface CE and DF in the same direction. The contribution of the body forces is represented by C and the flow turning angle is equal to β . When the first term on the left hand side of Equation (6) is expressed in terms of boundary layer characteristic parameters according to Equation (A41), Equation (6) reduces to:

$$\begin{aligned}
 & 2\rho_2 V_2^2 r_2 \cos \alpha_2 \cos(\alpha_2 - \beta) \sin \frac{\pi}{Z} - (\rho V^2)_{\infty 1} \cos^2 \alpha_1 \frac{2\pi}{Z} r_1 \\
 & \left\{ \frac{\sin \frac{\pi}{Z}}{\frac{\pi}{Z}} (1 - \Gamma \theta^{**}) - (\delta^* + \delta_{te} + \theta^*) \cos \frac{\pi}{Z} \right\} \\
 & = 2p_1 r_1 \sin \frac{\pi}{Z} - 2p_2 r_2 \cos \beta \sin \frac{\pi}{Z} + \frac{Q}{2b} + \frac{F}{2b} + \frac{C}{2b}
 \end{aligned} \tag{7}$$

where Γ is a parameter that depends on the end wall boundary layer profiles as given by Eq. (A42).

The Energy Equation

Assuming no heat or work exchange between the flow in the control volume and the surroundings and using the equation of state for a perfect gas we obtain:

$$\frac{(\rho_t)_{\infty 1}}{(P_t)_{\infty 1}} = \frac{\rho_{t2}}{P_{t2}} \quad (8)$$

Where the subscript, t, refers to the total conditions. Assuming the viscosity effects to be negligible in the free stream between stations 0 and 1, P_{t1} will be equal to P_{t0} and the energy equation can be written as follows:

$$\frac{(\rho_{t1})}{(\rho_{t2})} = \frac{P_{t0}}{P_{t2}} \quad (9)$$

Equations (3), (5), (7) and (9) will be used to calculate flow properties at station 2 in terms of the free stream and the boundary layer characteristic parameters at station 1. In order to carry out a solution the radius, r_2 , at which complete mixing has occurred is to be known. Moreover, the detailed flow conditions within the control volume are also needed in order to evaluate the quantities P, Q and the angle β in Equation (7).

SUDDEN MIXING ANALYSIS

The results obtained from the experimental investigation of Ref. [4] indicate that the nozzle wakes almost disappear near the zone of rapid adjustment, which is shown in Fig. 1. Assuming complete mixing to occur at a radius r_2 which is very close to r_1 is therefore an authentic model of reality.

For the limiting case of r_2 approaching r_1 , the flow deflection angle, the contributions of pressure forces acting on the mid-channel stream surfaces CE; DF as well as the body forces in the Y-Y direction will diminish. Consequently, the terms Q, C and the angle β in Equation (7) will tend to zero, and the governing equations are simplified to the following form:

$$\frac{P_{t2}}{P_{to}} = \frac{\cos \alpha_1 \rho_1^* M_1^* (1 - \delta^* - \delta_{te}^* - \lambda \theta^{**})}{\cos \alpha_2 \rho_2^* M_2^*} \quad (10)$$

$$M_2^* \sin \alpha_2 [1 - \delta^* - \delta_{te}^* - \lambda \theta^{**}] = M_1^* \sin \alpha_1 [1 - \delta^* - \delta_{te}^* - \theta^* - \eta \theta^{**}] \quad (11)$$

$$\begin{aligned} M_2^* \cos \alpha_2 \{ M_1^{*2} \cos^2 \alpha_1 [1 - \Gamma \theta^{**}] - \frac{(\delta^* + \delta_{te}^* + \theta^*) \frac{\pi}{Z}}{\tan \frac{\pi}{Z}} \} + \frac{\gamma+1}{2\gamma} (1 - \frac{\gamma-1}{\gamma+1} M_1^{*2}) \} \\ = M_1^* \cos \alpha_1 (1 - \delta^* - \delta_{te}^* - \lambda \theta^{**}) [M_2^{*2} \cos^2 \alpha_2 + \frac{\gamma+1}{2\gamma} (1 - \frac{\gamma-1}{\gamma+1} M_2^{*2})] \end{aligned} \quad (12)$$

where

$$M_1^* = \left(\frac{V_1}{V_{cr1}} \right)_{\infty}, \quad \rho_1^* = \left(\frac{\rho}{\rho_t} \right)_1, \quad M_2^* = \frac{V_2}{V_{cr2}}, \quad \rho_2^* = \left(\frac{\rho}{\rho_t} \right)_2 \quad (13)$$

Equations (11) and (12) can be solved simultaneously to determine the axisymmetric flow properties M_2^* and α_2 , providing that the flow conditions and the boundary layer characteristics are defined at the nozzle exit. Once M_2^* is obtained the density ratio ρ_2^* could be calculated from the following identity:

$$\rho_2^* = (1 - \frac{\gamma-1}{\gamma+1} M_2^{*2})^{\frac{1}{\gamma-1}} \quad (14)$$

If a similar expression for ρ_1^* in terms of M_1^* is used together with Equation (14) into Equation (10), the ratio between the total pressures P_{t2} and P_{to} is obtained. These pressure ratios are substituted into Equation (1) to determine the overall loss coefficient \bar{Y} , $\bar{\zeta}$, across the nozzle vanes. These loss coefficients will hence depend upon the nozzle geometry, the flow conditions M_1^* , α_1 , and the boundary layer characteristics δ^* , θ^* , θ^{**} , Γ , λ and η at the nozzle channel exit.

RESULTS AND DISCUSSION

The results of the present analysis show the effects of variation in nozzle geometry, flow conditions M_1 , α_1 , and the boundary layer characteristics δ^* , θ^* , θ^{**} , Γ , λ and η on the level of losses across the vanned region. A series of figures in which the variation of the loss coefficients \bar{Y} , $\bar{\zeta}$ with only two of the afore mentioned variables are presented at specified values for the rest of the parameters.

Figures 5, 6 and 7 represent the overall loss coefficient \bar{Y} and $\bar{\zeta}$ at flow discharge angle, α_1 , of 45° , 60° and 75° . Each figure demonstrates that the overall loss coefficients increase with increased nondimensional vane surface boundary layer momentum thickness, θ^* , for different values of the streamwise nondimensional momentum thickness of the end wall boundary layer, θ^{**} . It can also be seen from these figures that the losses decrease with the decrease in the end wall momentum thickness θ^{**} , with the minimum values corresponding to $\theta^{**} = 0$. This lower limit represents the losses in a nozzle channel of infinite aspect ratio. The nondimensional momentum thicknesses θ^{**} and θ^* are defined by Equations (A22) and (A27) and are both evaluated at exit from the nozzle channels.

Equation (A27) shows that the nondimensional momentum thickness, θ^* , is inversely proportional to the cosine of the flow discharge angle α_1 . For a specified value of the vane surface boundary layer momentum thickness, θ^* will increase with increased α_1 . Figures 5, 6 and 7 can therefore be used to show that the losses increase with increased flow discharge angles. This effect becomes more significant at higher values of α_1 . An accurate estimation of the exit flow angles is hence essential for loss evaluation.

Figure 8 shows the effect of the streamwise shape parameter, H_x , on \bar{Y} for the case of small cross flows. It is obvious the \bar{Y} is a weak function of H_x , which is known not to exceed 2, for unseparated turbulent boundary layers [6]. For all values of θ^{**} presented, the loss coefficients were found to increase not more than 5% for a corresponding increase in H_x from 1.2 to 2.

Since the vane trailing edge thickness, t_e , is increased when cooling of the radial turbine is considered, it would be desirable to examine the effect of t_e on the overall losses in some detail. This effect is investigated through the use of the parameter $t_e + \delta_s + \delta_p / \frac{2\pi Z}{r_1}$. The results are presented in Figure 9 as the ratio between the loss coefficient, \bar{Y} , at a finite value of t_e to \bar{Y} , calculated for zero trailing edge thickness. Figure 9 shows that the increase in the losses can be considerable for larger values of the trailing edge thickness. Under normal operating conditions corresponding to $\theta^* = 0.02$ and $\theta^{**} = 0.015$ in a conventional turbine with trailing edge thickness parameter, $t_e + \delta_s + \delta_p / \frac{2\pi Z}{r_1}$, of about 0.03 the trailing edge contribution to the losses is about 25 percent. If the parameter, $t_e + \delta_s + \delta_p / \frac{2\pi Z}{r_1}$, is increased to 0.07, the portion of the losses due to the finite trailing edge is increased to 82 percent.

The effect of compressibility on the overall loss coefficients are shown in Figures 10 and 11. It can be seen from Figure 10 that the enthalpy loss coefficient, $\bar{\zeta}$, remains practically constant with increased free stream Mach number, for the different values of the boundary layer parameters considered. On the other hand, the overall total pressure loss coefficient, \bar{Y} , increases significantly with increased Mach number, Figure 11. Due to the large sensitivity of the pressure loss coefficient to Mach number variations, it is recommended to use the overall enthalpy loss coefficient, $\bar{\zeta}$, in describing the loss performance characteristics of the radial turbine nozzles.

The effects of the end wall boundary layer cross flow on the losses are shown in Figures 12 and 13. Figure 12 illustrates the variation of \bar{Y} with θ^* , for the different end wall velocity profiles A, B, C and D of Table A-1 in Appendix A. Since it was found previously that the loss coefficients are weak functions of H_x it may be concluded, by examining Figure 12, that the cross flow profile parameters K and L (see Equation A9 and A10) have a significant effect on the losses. As an example, for a value of the nondimensional

streamwise momentum thickness, θ^{**} , of 0.03 a variation in the magnitude of losses up to 25% can result by considering different profiles.

Figure 13 shows the contribution of the cross flow to the losses which were calculated using the end wall velocity profile, B. It is clear from the figure that the minimum losses are obtained for the case of collateral end wall boundary layers $\epsilon = 0$. The losses increase appreciably for strong cross flow cases corresponding to higher values of ϵ .

PART II

FRICITION LOSSES IN THE VANELESS FIELD

The vaneless nozzle in a radial turbine consists of a smooth walled axisymmetric passage with radial or conical surfaces. The passage depth may change with radius, but a little influence on both the pressure and velocity distribution is noticed, since the angular component of the fluid momentum is predominant. Basically the flow in the vaneless nozzle can be treated as a vortex motion, except for the skin friction which acts upon the flow boundaries. In overcoming the resistance along its path the flow loses part of its total pressure. The pressure loss occurs at the expense of both static and dynamic pressure [8].

Loss analysis for the turbine vaneless nozzle may be treated using the same methods developed for the compressor vaneless diffuser, provided that the area changes as well as the flow direction are taken into consideration. Conventional flow analyses for the vaneless diffuser [9, 10, 11] were based on the assumption of one dimensional flow. Total pressure losses were determined using a constant friction coefficient. In a recent study, Jansen [12] arrived at a more accurate evaluation for the friction coefficient and its variation along the flow path. His analysis however, requires much more detailed knowledge of the flow conditions than can actually be realized in practice.

In the following study, the governing equations for the flow in the vaneless space are formulated using three dimensional end wall boundary layer theory [6]. The resulting differential equations are solved numerically to obtain the flow properties within the vaneless field. The losses are evaluated taking into account both the wall friction and the momentum flux changes due to velocity-profile variation along the flow path. The effects of some parameters representing the operating conditions and nozzle geometry on the losses incurred within the vaneless field are also investigated.

THE THREE DIMENSIONAL FLOW IN THE END WALLS BOUNDARY LAYER

Flow Pattern

As the flow in the vaneless field proceeds towards the impeller tip, the main streamlines turn as shown in Fig. 14. A balance is established in the main stream between the static pressure gradients and the centrifugal forces caused by the flow turning. The unbalance between the externally imposed pressure gradients and the centrifugal forces of low momentum end wall boundary layers, produces an acceleration component normal to the main stream direction in the boundary layer fluid. Consequently, the velocity in end wall boundary layers is different from the mainstream velocity, V , not only in magnitude but also in direction. The velocity profiles in this skewed boundary layer is shown in Fig. 15. Taylor [13] noticed that the polar plot of the velocity vector in a skewed boundary layer follows a triangular form such as shown in Fig. 15. Thus, any analysis of such boundary layer is usually carried out using different formulation in the inner and outer sublayers.

The Inner Sublayer

Referring to Fig. 15, the following linear relation between the cross flow velocity component, w , and the streamwise velocity component, v , holds good:

$$w = v \tan \psi_{\max} \quad (15)$$

The angle ψ_{\max} in the last equation is invariant within the collateral inner sublayer. Accordingly, it can be estimated at the wall using the following relation

$$\tan \psi_{\max} = \lim_{z \rightarrow 0} \frac{w}{v} = \epsilon \quad (16)$$

Since the skin friction is in the same direction as the velocity vector at the wall, therefore it will deviate by the angle, ψ_{\max} , from the main flow direction. If the wall shear stress and the friction coefficient are denoted by τ_0 and C_f respectively

and if their components in the main flow direction by τ_x and C_{fx} , then:

$$C_f = C_{fx}(1 + \epsilon^2)^{1/2} \quad (17)$$

where

$$C_f = \frac{\tau_o}{\frac{1}{2} \rho V^2} \quad (18)$$

and

$$C_{fx} = \frac{\tau_x}{\frac{1}{2} \rho V^2} \quad (19)$$

Ludwieg and Tillman [14] deduced an accurate semi-empirical expression for the wall friction of two dimensional flows in the presence of favorable pressure gradients. Johnston [6] showed that in a skewed boundary layer, the relation of Ref. [14] can be used to determine the component of the skin friction coefficient in the main flow direction according to the following relation:

$$C_{fx} = 0.246 [\text{Exp}(-1.561 H_x)] R_{\theta x}^{-0.268} \quad (20)$$

where H_x is the streamwise shape factor, and $R_{\theta x}$ is the Reynolds number based on the streamwise momentum thickness.

Referring to Fig. 16, the components of shear stresses in the tangential and the radial directions are

$$\tau_\theta = \tau_o \sin(\alpha - \psi_{\max}) \quad (21)$$

$$\tau_r = \tau_o \cos(\alpha - \psi_{\max}) \quad (22)$$

When Equations (16), (17) and (18) are substituted in Equations (21) and (22), the following relations are obtained:

$$\tau_\theta = \frac{1}{2} \rho V^2 C_{fx} [\sin \alpha - \epsilon \cos \alpha] \quad (23)$$

$$\tau_r = \frac{1}{2} \rho V^2 C_{fx} [\cos \alpha + \epsilon \sin \alpha] \quad (24)$$

In the above equations, the values of α and ϵ will depend on the main flow variables. The expressions which are used in evaluating these parameters are given in the outer sublayer analysis that follows.

The Outer Sublayer

The two velocity components in the non-collateral outer sublayer, namely the cross flow component, w , and the streamwise component, v , are related by the following equation,

$$w = A(V - v) \quad (25)$$

The parameter A depends on the main flow turning angle (β), which is shown in Fig. 14, and is given by the following expression:

$$A = - 2V^2 \int_{\beta_0}^{\beta} \frac{d\beta}{V^2} \quad (25a)$$

where V is the main flow velocity.

The tangent, ϵ , of the limiting angle, ψ_{\max} , can be expressed in terms of the parameter A and the streamwise friction coefficient, C_{fx} , according to the analysis of Ref. [6] as:

$$\frac{\epsilon}{A} = 0.1 \left[\frac{(1 + \epsilon^2)^{1/4}}{\sqrt{C_{fx}}} \right] - 1 \quad (25b)$$

Equations (20), (25) and (25b) can be substituted into Equations (23) and (24) to predict the variation of shear components τ_θ , τ_r along the flow path in terms of main flow variables. The details of the computation procedure used for this prediction is presented in the section dealing with the Numerical Solution of the Governing Equations.

CALCULATION OF THE MAIN FLOW PROPERTIES IN THE VANELESS FIELD

Analysis

The vaneless space geometry, together with the velocity triangles and the coordinate system are shown in Fig. 17. It is assumed that the flow enters the vaneless field at the radius, r_2 , in a steady uniform axisymmetric pattern, with specified flow conditions. These inlet flow properties are determined from the vanes friction and mixing loss analysis presented in Part I of this study.

As the flow passes through the vaneless field, there will be a variation in its properties in both radial and axial directions. The variation in the axial direction, z , results from the development of boundary layer over the two end walls. The static pressure distribution and the radial and tangential velocity components will be determined along the main flow path, using the assumptions of the first order boundary layer theory. An equivalent one dimensional flow will be considered in a nozzle with an effective depth of $2b_e$, which is equal to the actual nozzle depth, $2b$, minus the displacement thicknesses of the two end wall boundary layers at any radius, r (see Fig. 18). The components of the velocity, V , and the pressure, p , of the flow passing through this equivalent nozzle, vary only along the radial direction, and are independent of z and θ . The total pressure loss due to friction will be calculated using the values of τ_r and τ_θ developed in the previous section and given by Equations (23) and (24).

Equations of Motion

The control volume of Fig. 19 will be used in the following derivation. The magnitude of the velocity, V , is considered to increase as the flow proceeds inward in the vaneless nozzle. Furthermore, the flow will be assumed to be steady and adiabatic.

Conservation of Angular Momentum:

Setting the net efflux of angular momentum through the control volume, equal to the external torque due to the shear force in the tangential direction, we obtain the following relation:

$$\rho b_e V \cos \alpha \frac{d}{dr} (r V \sin \alpha) = \tau_\theta r \quad (26)$$

Substituting for τ_θ from Equation (23) into Equation (24), we get:

$$\frac{V \cos \alpha}{r} \frac{d}{dr} (r V \sin \alpha) + V \cos \alpha \frac{d}{dr} (V \sin \alpha) = \frac{C_{fx} V^2}{2b_e} r [\sin \alpha - \epsilon \cos \alpha] \quad (26a)$$

Conservation of Linear Momentum in Radial Direction:

$$-\rho b_e V \cos \alpha \frac{d}{dr} (V \cos \alpha) = b_e \frac{d}{dr} (p) - \tau_r - \frac{\rho b_e V^2 \sin^2 \alpha}{r} \quad (27)$$

The left hand side of the above equation is equal to the net radial momentum flux. The first two terms on the right hand side are the radial components of the pressure forces and the wall friction forces, while the third term represents the centrifugal forces.

Substituting for τ_r from Equation (24) into (27) and rearranging we obtain:

$$-V \cos \alpha \frac{d}{dr} (V \cos \alpha) = \frac{1}{\rho} \frac{dp}{dr} - \frac{C_{fx}}{2b_e} V^2 [\cos \alpha + \epsilon \sin \alpha] - \frac{V^2 \sin^2 \alpha}{r} \quad (27a)$$

Conservation of Mass:

From continuity considerations, the following differential equation is obtained:

$$\frac{1}{\rho} \frac{d\rho}{dr} + \frac{1}{V \cos \alpha} \frac{d(V \cos \alpha)}{dr} + \frac{1}{r} + \frac{1}{b_e} \frac{db_e}{dr} = 0 \quad (28)$$

Equation of State:

The pressure density temperature relation for a perfect gas is used in the following differential form:

$$\frac{1}{p} \frac{dp}{dr} = \frac{1}{\rho} \frac{d\rho}{dr} + \frac{1}{T} \frac{dT}{dr} \quad (29)$$

Energy Equation:

Since the total temperature remains constant during the expansion process in the vaneless field, the differential form of the energy equation may be written as:

$$\frac{1}{T} \frac{dT}{dr} = - \frac{\frac{\gamma-1}{2} M^2}{1 + \frac{\gamma-1}{2} M^2} \frac{1}{M^2} \frac{dM^2}{dr} \quad (30)$$

Which, when combined with the definition of the Mach number reduces to:

$$\frac{1}{V^2} \frac{dV^2}{dr} = \frac{1}{M^2} \frac{dM^2}{dr} \left[\frac{1}{1 + \frac{\gamma-1}{2} M^2} \right] \quad (30a)$$

Formulation of Relations Describing the Variation of Flow Properties Along the Flow Path

Equations (26) through (30) will be manipulated to obtain the following relations which are used to calculate the pressure, Mach Number and the main flow angle.

Pressure Distribution

Combining Equations (29) and (30a), the following relation is obtained

$$\frac{1}{\rho} \frac{d\rho}{dr} = \frac{1}{p} \frac{dp}{dr} + \frac{\frac{\gamma-1}{2} M^2}{1 + \frac{\gamma-1}{2} M^2} \frac{1}{M^2} \frac{dM^2}{dr} \quad (31)$$

Dividing Equation (27a) by $V^2 \cos^2 \alpha$ and using the identity,

$$\rho V^2 = \gamma p M^2 \quad (32)$$

one gets an expression describing the variation of the tangential velocity component with radius as

$$-\frac{1}{V \cos \alpha} \frac{d}{dr} (V \cos \alpha) = \frac{1}{\gamma M^2 \cos^2 \alpha} \frac{1}{p} \frac{dp}{dr} - \frac{C_{fx}}{2b_e} \frac{(\cos \alpha + \epsilon \sin \alpha)}{\cos^2 \alpha} - \frac{\tan^2 \alpha}{r} \quad (33)$$

Substituting for $\frac{1}{p} \frac{dp}{dr}$ from Equation (31), $\frac{1}{V \cos \alpha} \frac{d}{dr} (V \cos \alpha)$ from Equation (33) into the continuity Equation (28), the variation of pressure with radius is deduced as:

$$\begin{aligned} \frac{1}{p} \frac{dp}{dr} = & \frac{M^2}{M^2 - \sec^2 \alpha} \left[-\frac{C_{fx}}{2b_e} \frac{(\cos \alpha + \epsilon \sin \alpha)}{\cos^2 \alpha} - \frac{\sec^2 \alpha}{r} \right. \\ & \left. - \left(\frac{\frac{\gamma-1}{2} M^2}{1 + \frac{\gamma-1}{2} M^2} \right) \frac{1}{M^2} \frac{dM^2}{dr} - \frac{1}{b_e} \frac{db_e}{dr} \right] \end{aligned} \quad (34)$$

Mach Number Distribution

In order to obtain the variation of Mach number along the flow path, an additional equation relating the pressure in terms of M and α is required. This relation is obtained by combining the equation of angular momentum (26a) with the equation of linear momentum (27a).

$$\frac{1}{V^2} \frac{1}{p} \frac{dp}{dr} = \frac{C_{fx}}{2b_e} \left(\frac{1}{\cos \alpha} \right) - \frac{1}{2V^2} \frac{dV^2}{dr} \quad (35)$$

Substituting Equations (30a) and (32), into the last equation, it reduces to:

$$\frac{1}{p} \frac{dp}{dr} = \frac{\gamma M^2}{2} \left[\left(\frac{-1}{1 + \frac{\gamma-1}{2} M^2} \right) \frac{1}{M^2} \frac{dM^2}{dr} + \frac{C_{fx}}{b_e \cos \alpha} \right] \quad (36)$$

Now, eliminating $\frac{1}{p} \frac{dp}{dr}$ between Equations (34) and (36), the Mach number variation along the radius, r , is obtained from the resultant expression.

$$\frac{1}{M} \frac{dM}{dr} = \frac{1 + (\frac{\gamma-1}{2})M^2}{M^2 - \sec^2 \alpha} \left[\frac{\sec^2 \alpha}{r} + \frac{C_{fx}}{2b_e} \sec \alpha (\gamma M^2 - \tan^2 \alpha + \epsilon \tan \alpha) + \frac{1}{b_e} \frac{db_e}{dr} \right] \quad (37)$$

Flow Direction

The differential equation of flow direction may be developed using the following relation:

$$\tan \alpha = \frac{V \sin \alpha}{V \cos \alpha} \quad (38)$$

This last equation, can be written in the following differential form:

$$\frac{1}{\tan \alpha} \frac{d(\tan \alpha)}{dr} = \frac{1}{V \sin \alpha} \frac{d(V \sin \alpha)}{dr} - \frac{1}{V \cos \alpha} \frac{d(V \cos \alpha)}{dr} \quad (38a)$$

Substituting Eq. (26a) and (33) into Equation (38a), the following relation is obtained:

$$\frac{1}{\tan \alpha} \frac{d(\tan \alpha)}{dr} = \frac{\sec^2 \alpha}{\gamma M^2} \frac{1}{p} \frac{dp}{dr} - \frac{\sec^2 \alpha}{r} \quad (39)$$

Substituting for $\frac{1}{p} \frac{dp}{dr}$ from Equation (34) and rearranging, the equation describing the variation of flow direction with radius takes the following form:

$$\frac{d\alpha}{dr} = \frac{-\tan \alpha}{M^2 - \sec^2 \alpha} \left\{ \frac{M^2}{r} + \frac{C_{fx} \sec \alpha}{2b_e} [1 + (\gamma-1)M^2 + \epsilon \tan \alpha] + \frac{1}{b_e} \frac{db_e}{dr} \right\} \quad (40)$$

Nondimensional Form of the Governing Equations:

Before solving the equations of motion, they will first be written in a nondimensional form. The nozzle dimensions will be normalized with respect to the inlet radius, r_2 , and the pressures with respect to the total inlet pressure, P_{t2} , as follows:

$$R = \frac{r}{r_2}, \quad B = \frac{2b_e}{r_2}, \quad ; \quad P = \frac{p}{P_{t2}}$$

Equations (34), (37) and (40) can therefore be written in the following nondimensional form using the above expressions.

$$\begin{aligned} \frac{1}{P} \frac{dP}{dR} = & \frac{\gamma M^2}{\gamma M^2 - \sec^2 \alpha} \left[-\frac{C_{fx}}{B} \frac{(\cos \alpha + \epsilon \sin \alpha)}{\cos^2 \alpha} - \frac{\sec^2 \alpha}{r} \right. \\ & \left. - \left(\frac{\frac{\gamma-1}{2} M^2}{1 + \frac{\gamma-1}{2} M^2} \right) \frac{1}{M^2} \frac{dM^2}{dR} - \frac{1}{B} \frac{dB}{dR} \right] \end{aligned} \quad (42)$$

$$\frac{1}{M} \frac{dM}{dR} = \frac{1 + \frac{\gamma-1}{2} M^2}{M^2 - \sec^2 \alpha} \left[\frac{\sec^2 \alpha}{R} + \frac{C_{fx}}{B} \sec \alpha (\gamma M^2 - \tan^2 \alpha + \epsilon \tan \alpha) + \frac{1}{B} \frac{dB}{dR} \right] \quad (43)$$

and

$$\frac{d\alpha}{dR} = \frac{-\tan \alpha}{M^2 - \sec^2 \alpha} \left[\frac{M^2}{R} + \frac{C_{fx} \sec \alpha}{B} (1 + (\gamma-1)M^2 + \epsilon \tan \alpha) + \frac{1}{B} \frac{dB}{dR} \right] \quad (44)$$

Furthermore, if the thicknesses of the boundary layers developed over the two end walls are taken to be equal, then, B , the depth ratio, and its derivative could be expressed as:

$$B = \frac{2b - 2\delta_x}{r_2}, \quad \frac{dB}{dR} = \frac{-2d\left(\frac{\delta_x}{r_2}\right)}{dR} \quad (45)$$

where δ_x is the streamwise displacement thickness.

PROCEDURE FOR THE NUMERICAL SOLUTION OF THE GOVERNING EQUATIONS

In order to determine the flow properties within the vaneless field, the system of nonlinear differential Equations (43), (44) and the algebraic Equations (20), (25a) and (25b) will be solved. A fourth order Runge-Kutta algorithm is used to solve the simultaneous first order differential Equations (43) and (44). The solution procedure consists of the following steps:

1. The values of M , α , at the vaneless nozzle inlet, are assumed to be known from the analysis given in Part I.

2. At any radius R_i , knowing M_i , α_i , C_{fx} , ϵ , B and $\frac{dB}{dR}$, the increments in M and α , over the radial distance $(-\Delta R)$ is computed using the following recursion formula:

$$M_{i+1} - M_i = -\frac{\Delta R}{6} (K_1 + 2K_2 + 2K_3 + K_4) \quad (46)$$

$$\alpha_{i+1} - \alpha_i = -\frac{\Delta R}{6} (KK_1 + 2KK_2 + 2KK_3 + KK_4) \quad (47)$$

where

$$K_1 = f(R_i, M_i, \alpha_i)$$

$$KK_1 = g(R_i, M_i, \alpha_i)$$

$$K_2 = f\left(R_i - \frac{\Delta R}{2}, M_i + \frac{K_1}{2}, \alpha_i + \frac{KK_1}{2}\right) \quad (48)$$

$$KK_2 = g\left(R_i - \frac{\Delta R}{2}, M_i + \frac{K_1}{2}, \alpha_i + \frac{KK_1}{2}\right)$$

$$K_3 = f\left(R_i - \frac{\Delta R}{2}, M_i + \frac{K_2}{2}, \alpha_i + \frac{KK_2}{2}\right)$$

$$KK_3 = g\left(R_i - \frac{\Delta R}{2}, M_i + \frac{K_2}{2}, \alpha_i + \frac{KK_2}{2}\right)$$

$$K_4 = f(R_i - \Delta R, M_i + K_3, \alpha_i + KK_3)$$

$$KK_4 = g(R_i - \Delta R, M_i + K_3, \alpha_i + KK_3)$$

Where f represents $\frac{dM}{dR}$ and g $\frac{d\alpha}{dR}$, and are evaluated according to Equations (43) and (44) respectively, using the known values of C_{fx} , A , ϵ , B and $\frac{dB}{dR}$ at the radius, R_i .

3. At the end of the interval, at the new radial location $R_i - \Delta R$, the quantities C_{fx} , A , ϵ , B and $\frac{dB}{dR}$ are evaluated using Equations (20), (25a) and (25b) respectively, as will be explained. The streamwise friction coefficient, C_{fx} , is calculated according to Equation (20). The boundary layer characteristic parameters, $R_{\theta x}$ and H_x , in this equation, can be evaluated using any method of boundary layer solution. In the present analysis, the method of Reference 15 was used for this purpose. Integrating Equation (25b) numerically, starting from the vaneless nozzle inlet, until any desired radius, where the mean flow turning angle, β , is known, gives the corresponding value of A at R_{i+1} . These values of C_{fx} and A are then substituted into Equation (25c), which is solved for ϵ using an iterative procedure.

4. Refined values for M_{i+1} , α_{i+1} at $(R_i - \Delta R)$ are obtained by substituting the arithmetic average between R_i and R_{i+1} of the variables C_{fx} , ϵ , B and $\frac{dB}{dR}$ in the recursion formula (46) and (47).

5. The corresponding values for C_{fx} , A , ϵ , B , $\frac{dB}{dR}$ at R_{i+1} are calculated as shown in Step 3, using the values of M_{i+1} , α_{i+1} obtained from Step 4.

6. Steps 4 and 5 are repeated until successive values of the computed flow variables are within the required accuracy. In the present study, an accuracy of 0.001 was maintained in the different variables, which was achieved after 2 iterations.

7. The whole procedure (Steps 2 through 6) is repeated for small values of $(-\Delta R)$ starting from the nozzle inlet up to the impeller tip. The numerical results reported herein were calculated using radial increments ΔR equal to 0.01.

EVALUATION OF LOSS COEFFICIENTS ACROSS THE VANELESS FIELD

Standard definitions of total pressure and enthalpy loss coefficients, in terms of the average pressures at inlet to and exit from the vaneless region are adopted. The total pressure loss coefficient is given by:

$$\bar{Y} = \frac{1 - \frac{P_{t3}}{P_{t2}}}{1 - \frac{P_3}{P_{t2}}} \quad (49)$$

while the enthalpy loss coefficient may be written as:

$$\frac{\left(\frac{P_{t2}}{P_{t3}}\right)^{\frac{\gamma-1}{\gamma}} - 1}{\left(\frac{P_{t2}}{P_3}\right)^{\frac{\gamma-1}{\gamma}} - 1} \quad (50)$$

It is clear from the above two equations that the flow conditions at station 3, the vaneless space exit, have to be known in order to calculate the loss coefficients.

In the previous chapter, it is explained how to determine, numerically, the Mach number, the flow angle and the effective nozzle depth variations along the flow path. Knowing the values of these variables at the nozzle exit (station 3), the static and total pressures, p_3 and P_{t3} , are computed using the equations derived below.

The conservation of mass between the vaneless diffuser inlet and exit, is expressed as:

$$\rho_2 V_2 \cos \alpha_2 r_2 b_2 = \rho_3 V_3 \cos \alpha_3 r_3 b_{e3} \quad (51)$$

where $2b_{e3}$ is the effective depth of the nozzle at station 3.

If the definition of Mach number and the equation of state are substituted into the above Equation (51), the following expression for p_3/p_2 is obtained:

$$\frac{p_3}{p_2} = \frac{b_2}{b_{e_3}} \frac{r_2}{r_3} \frac{\cos \alpha_2}{\cos \alpha_3} \frac{M_2}{M_3} \sqrt{\frac{1 + \frac{\gamma-1}{2} M_2^2}{1 + \frac{\gamma-1}{2} M_3^2}} \quad (52)$$

The total pressure at the vaneless space exit, P_{t3} , is then determined using the following relation:

$$\frac{P_{t3}}{P_{t2}} = \frac{p_3}{p_2} \left[\frac{1 + \frac{\gamma-1}{2} M_3^2}{1 + \frac{\gamma-1}{2} M_2^2} \right]^{\frac{\gamma}{\gamma-1}} \quad (53)$$

Equations (52) and (53) are sufficient to determine the loss coefficients $\bar{\gamma}$ and $\bar{\zeta}$, provided that the inlet flow conditions to the vaneless space are specified.

RESULTS AND DISCUSSION

The numerical examples worked out using the present method of analysis are presented in two groups. In the first group, the effects of inlet flow conditions on the flow behavior and losses in the vaneless field are investigated. The second set of results illustrate the influence of changing the end wall spacing on the same flow parameters.

1. Effects of Inlet Flow Conditions

The effect of two inlet flow parameters, namely the Mach number and the flow angle on the vaneless nozzle performance are considered first. Computations were carried out with an inlet Mach number of 0.8 and different inlet flow angles α_2 , the corresponding results are shown in Figures 20 to 22. On the other hand, the data obtained with different Mach numbers for a constant inlet flow angle of 70° are presented in Figures 23 to 25. The geometrical end wall spacing, $2b$, and the inlet radius to the vaneless field, r_2 , for this first set of results were chosen to be 0.339 and 3.93 inches respectively. The total temperature was held constant throughout the flow at 2000°R .

The change in angular momentum ratio, $r_3 V_3 \sin \alpha_3 / r_2 V_2 \sin \alpha_2$, with the normalized radius, R , is shown in Figure 20 for different values of inlet flow angles, α_2 . It can be seen that increasing α_2 causes a reduction in the angular momentum ratio everywhere. This effect becomes particularly predominant at high values of inlet flow angles. For example, at a normalized radius of 0.9, the angular momentum ratio changes from 0.992 to 0.987 corresponding to an increase in α_2 from 60° to 70° . Meanwhile, a further increase in α_2 from 70° to 80° results in a reduction of the same parameter from 0.987 to 0.973.

The radial variations of the ratio, M_3^2/M_2^2 , are shown in Figure 21 for three different values of inlet flow angle. It can be seen from the figure that increasing α_2 reduces M_3^2/M_2^2 at each radius. This is a consequence of the larger reduction in the tangential velocity component, due to viscosity, an influence that dominates the augmentation in the smaller radial velocity component. It can also be concluded that for all the values of α_2 the ratio M_3^2/M_2^2 increases as the flow proceeds inwards which is anticipated.

The variation in the pressure loss coefficient, $\bar{\gamma}$, and enthalpy loss coefficient, $\bar{\xi}$, are shown in Figures 22a and 22b respectively. It is clear that both coefficients increase with increased inlet flow angle, α_2 , at every radial location. If the results of Figure 22 are compared with those obtained in Part 1 it can be concluded that, even for the largest values of α_2 , the loss coefficients in the vaneless field are extremely low as compared to the losses in the vaned region. For example, the pressure loss coefficient of Figure 22b is as low as 0.0125 at $R = 0.90$ for values of α_2 and M_2 of 60° and 0.8, respectively. On the other hand, the pressure loss coefficient of Figure 8 is as high as 0.107 under the same operating conditions.

Briefly, one can conclude that increasing the inlet flow angle, α_2 , results in a larger reduction in the total pressure, Mach number and angular momentum at nozzle exit. This can be attributed to the longer path that the flow has to take to reach a certain radius if the inlet flow angle is increased.

The effect of changing the inlet Mach number, M_2 , on the angular momentum ratio is illustrated in Figure 23. It is evident that at any radius, the drop in angular momentum due to viscous losses, is smaller for high values of M_2 . Accordingly, high Mach numbers at inlet to the turbine vaneless field are recommended. The variation in the ratio M_3^2/M_2^2 is shown in Figure 24 for different values of inlet Mach number. It is obvious that the acceleration rate in vaneless field is higher for larger inlet Mach number.

The pressure and enthalpy loss coefficients $\bar{\gamma}$ and $\bar{\xi}$ are shown in Figures 25a and 25b respectively. It is clear that the pressure loss penalty paid due to viscous effects at any radius ratio, is not strongly affected by the inlet Mach number. Furthermore, the enthalpy loss coefficient at any radius remains practically constant for all the inlet Mach numbers investigated.

2. Effects of Nozzle and End Wall Spacing

The object of the second group of numerical examples is to study the effect of the geometrical passage depth, $2b$, on some flow

properties and on the loss characteristics in the vaneless field. For this purpose, the following values of the passage depth were considered: 0.262", 0.393" and 0.785" with an inlet radius to the vaneless field of 3.93". The corresponding values of the nondimensional parameter ($r_2/2b$) thus ranges between 15 and 5. The results were obtained at 0.8 inlet Mach number and 70° inlet flow angle with an inlet total temperature of 2000°R.

Figure 26 represents the radial variations of angular momentum ratio, $r_3 V_3 \sin \alpha_3 / r_2 V_2 \sin \alpha_2$, for the three values of the parameter ($r_2/2b$). Although the angular momentum ratio decreases at any radius, R , with the decrease in end wall spacing, $2b$, the curves indicate that there is only minor differences between smallest and largest values of the parameter ($r_2/2b$). The change in the ratio, M_3^2/M_2^2 , with R is shown in Figure 27. Increasing the passage depth, $2b$, results in an increase in M_3^2/M_2^2 at any radius ratio, R . The increase in M_3^2/M_2^2 results primarily from the reduction in the friction surface area compared to the total flow area as the wall spacing is increased. Figure 27 also indicates that the variation of nozzle end wall spacing, $2b$, has a small influence on the Mach number distribution within the vaneless space.

The influence of the end wall spacing on flow losses is shown in Figures 28a and 28b. It is clear that larger losses are incurred as the nozzle passage becomes narrower, corresponding to high values of $r_2/2b$. It is important to emphasize once more that, even for the large values of ($r_2/2b$), the losses in the vaneless field remain relatively low as compared to the vaned region losses.

CONCLUSIONS

An analytical model which is based on the observations obtained from an experimental study was developed to predict the losses in a radial nozzle annulus. The contributions of the end wall boundary layers to the losses was found to be several times that of the vane surface boundary layers. This influence is particularly significant when the end wall boundary layers are characterized by large cross flow components. Under the stipulation of the analytical model in which the mixing losses are lumped with the friction losses in the vanned region, a small portion of the overall losses were contributed by the viscous effect in the vaneless field. Experimental findings in which stator-rotor interaction effects are not considered show that the losses are influenced by flow nonuniformities at inlet to the nozzle channel and by secondary flow. These factors need further investigation if a realistic estimate for the losses is to be obtained analytically.

It is concluded that, generally the losses in a radial nozzle assembly would not be greatly affected by the addition of a large vaneless space. Also, if the nonuniformities of the flow discharged from the vanned region can be reduced, the efficiency of the assembly as a whole would be improved. Thus, the loss penalty paid during an expansion process, resulting in the required flow properties at rotor tip from a specified outlet flow condition from the scroll, could be minimized. Such minimization is achieved by a proper selection of vanes configurations in conjunction with a suitable vaneless space dimension. The application of the composite method of analysis presented allows one to differentiate between various suggested radial nozzle designs in order to select the optimum configuration.

REFERENCES

1. Todd, Carroll A. and Futral, Jr., Samuel M., "A FORTRAN IV Program to Estimate the Off-Design Performance of Radial Inflow Turbines," NASA TND-5059, 1969.
2. Futral, Jr., Samuel M. and Wasserbauer, C.A., "Off-Design Performance Prediction with Experimental Verification for a Radial-Inflow Turbine," NASA TND-2621, 1965.
3. Baljie, O.E., "A Contribution to the Problem of Designing Radial Turbomachines," Trans. ASME, Vol. 74, 1952, pp. 451-472.
4. Tabakoff, W. and Khalil, I., "Experimental Study on Radial Inflow Turbine, With Special Reference to Loss Prediction," University of Cincinnati, Department of Aerospace Engineering Report No. 75-50.
5. Stewart, W.L., "Analysis of Two-Dimensional Compressible-Flow Loss Characteristics Downstream of Turbomachine Blade Row in Terms of Basic Boundary-Layer Characteristics," NACA TN 3515, 1955.
6. Johnston, J.P., "On the Three Dimensional Turbulent Boundary Layer Generated by Secondary Flow," Trans. ASME, Journal of Basic Engineering, Series D, March 1960, pp. 233-247.
7. Dring, R.P., "A Momentum Integral Analysis of the Three-Dimensional Turbine End-Wall Boundary Layer," ASME Paper No. 71-GT-6.
8. Vavra, M., "Aero-Thermodynamics and Flow in Turbomachines," John Wiley, New York, 1960.
9. Polikovsky, V. and Nevelson, M., "The Performance of a Vaneless Diffuser Fan," NACA TM 1038, 1942 (Trans. of Report 224 of the Central Aero-Hydrodynamics Institute, Moscow, 1935).
10. Brown, W.B. and Bradshaw, G.R., "Method of Designing Vaneless Diffusers and Experimental Investigation of Certain Undetermined Parameters," NACA TN 1426, 1947.
11. Stanitz, John D., "One-Dimensional Compressible Flow in Vaneless Diffusers of Radial and Mixed-Flow Centrifugal Compressors," NACA TN 2610, January 1952.

12. Jansen, W., "Steady Flow in a Radial Vaneless Diffuser," Journal of Basic Engineering, Transactions of ASME, Series D, Vol. 86, 1964, pp. 607-619.
13. Mager, A., "Generalization of Boundary Layer Momentum Integral Equations to Three Dimensional Flow Including Those of Rotating Systems," NACA Report 1067, 1952.
14. Ludwig, H. and Tillmann, W., "Investigation of the Wall Shearing Stress in Turbulent Boundary Layers," NACA TM 1285, May 1950.
15. Truckenbrodt, E., "A Method of Quadrature for Calculation of the Laminar and Turbulent Boundary Layer in Case of Plate and Rotationally Symmetrical Flow," NACA TM 1379, May 1955.

NOMENCLATURE

Symbol

A	parameter (see Eq. 25b)
B	depth ratio defined as $2b_e/r_2$
2b	axial depth of the nozzle - distance between the two end walls, ft.
$2b_e$	effective depth of the nozzle
C_f	skin friction coefficient
G	streamwise profile function
g	cross-flow profile function (see Eq. A7)
H_x	streamwise shape factor for the end walls boundary layers (see Eq. A8)
K,L	profile parameter, for the end walls boundary layer (see Eq. A9, A10)
M	Mach number, dimensionless
M^*	critical Mach number, dimensionless
n	coordinate normal to the vane surface, ft.
P	pressure ratio defined as p/P_{t2}
p	static pressure, lb_f/ft^2
P_t	total pressure, lb_f/ft^2
r	radial coordinate, ft.
R	radius ratio defined as r/r_2
$R_{\theta x}$	Reynolds number based on momentum thickness of the main flow, dimensionless
T	temperature, °R
t_e	vane trailing edge thickness, ft.
v	streamwise velocity component in the boundary layer over the end walls, ft/sec

V	velocity, ft/sec
w	cross-flow velocity component in the boundary layer over the end walls, ft/sec
\bar{Y}	overall total pressure loss coefficient
z	axial coordinate, ft.
Z	number of vanes, dimensionless
α	angle between flow direction and inward radial direction, radians
β	main flow turning angle, radians (see Fig. 14)
γ	ratio of specific heats, dimensionless
Γ	parameter (see Eq. 6A)
δ	boundary layer displacement thickness, ft.
δ_{te}	trailing edge blocking factor defined as $te / (\frac{2\pi}{Z} r_1 \cos \alpha_1)$
δ^*	total nondimensional displacement thickness over the vane surfaces defined as $(\delta_s + \delta_p) / (\frac{2\pi}{Z} r_1 \cos \alpha_1)$
δ^{**}	streamwise total nondimensional displacement thickness, over the two end walls, defined as $(\delta_{ux} + \delta_{lx}) / 2b$
θ	boundary layer momentum thickness, ft.; or angular coordinate in plane normal to axis of rotation, radians
θ^*	total nondimensional momentum thickness over the vane surfaces, defined as $(\theta_s + \theta_p) / (\frac{2\pi}{Z} r_1 \cos \alpha_1)$
θ^{**}	streamwise total nondimensional momentum thickness over the two end walls, defined as $(\theta_{ux} + \theta_{lx}) / 2b$
λ	parameter (see Eq. A23)
ρ	density, lb/ft ³
η	parameter (see Eq. A31)
ψ_w	angle of limiting wall streamline and τ_o with respect to V_{fs}

τ_o shear stress at the wall
 $\bar{\zeta}$ overall enthalpy loss coefficient
 ϵ tangent of the limiting streamline defined as $\tan\psi_w$

Subscripts

0 inlet to radial nozzle, outlet from the scroll
1 nozzle exit
2 station at which uniform conditions are assumed to take place
3 inlet to rotor
c cross flow direction
cr critical conditions
 ∞ local conditions outside the boundary layer regions
l end wall lower surface
p vane pressure surface
s vane suction surface
t total conditions
u end wall upper surface
r radial direction
x streamwise direction

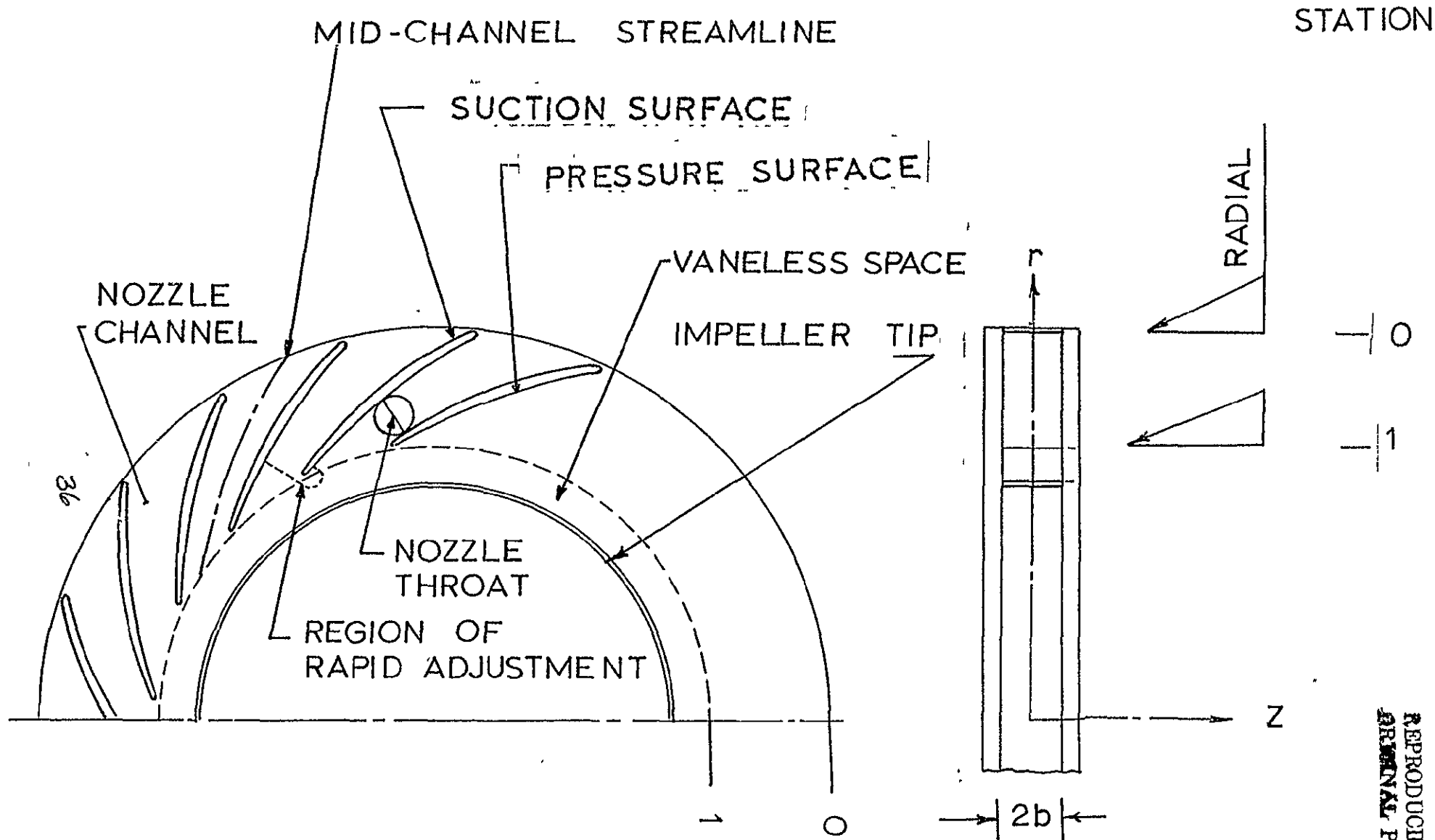
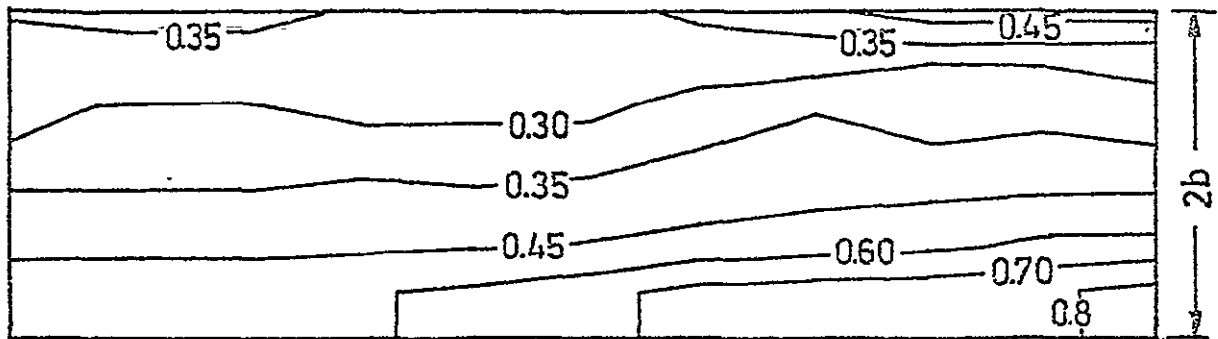
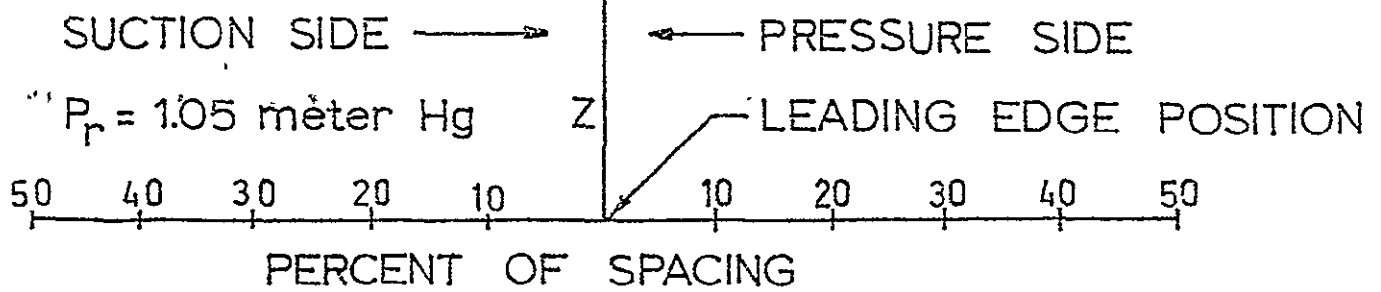
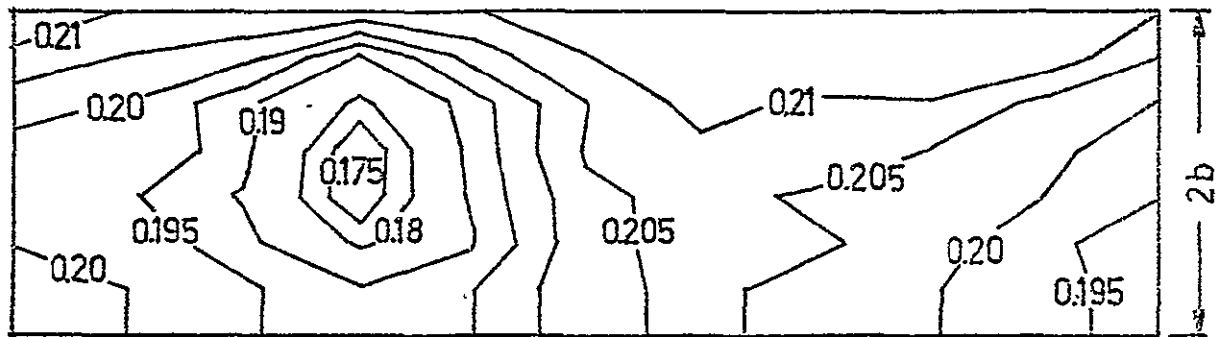


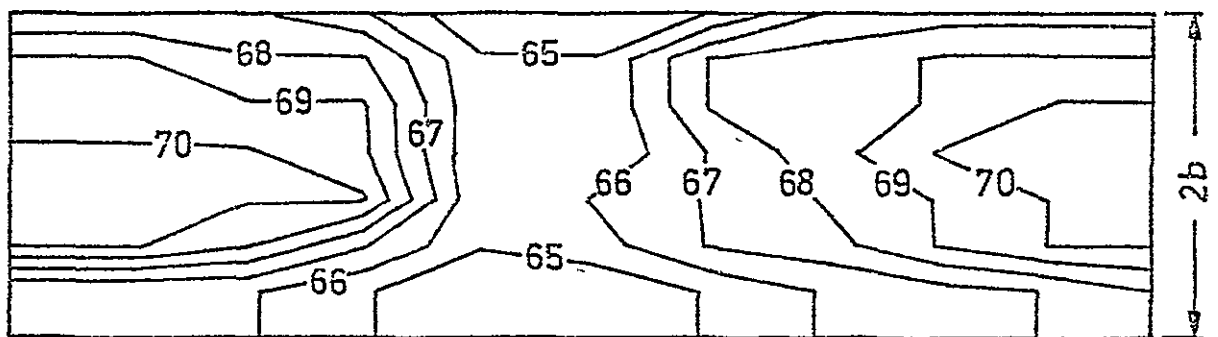
FIG. 1: FLOW REGIONS AND VELOCITY DIAGRAMS



a - TOTAL PRESSURE = $(P_r - P_{t_o}) / P_r$ PERCENT

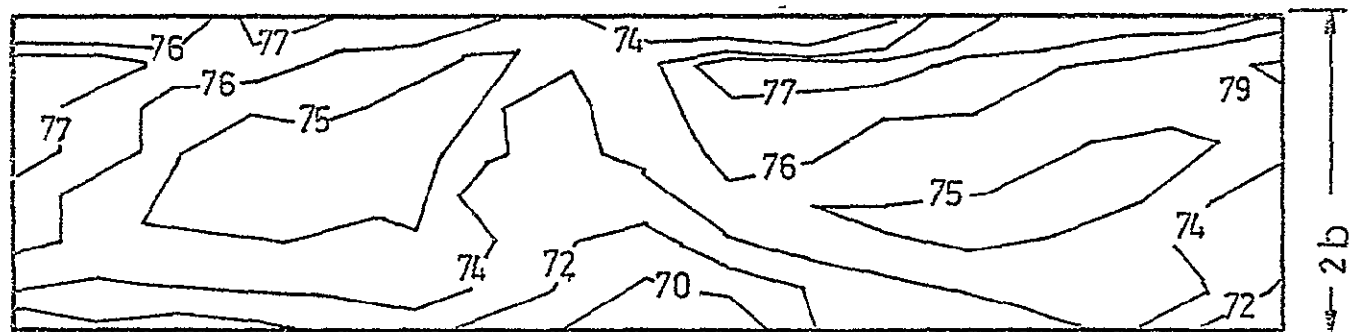
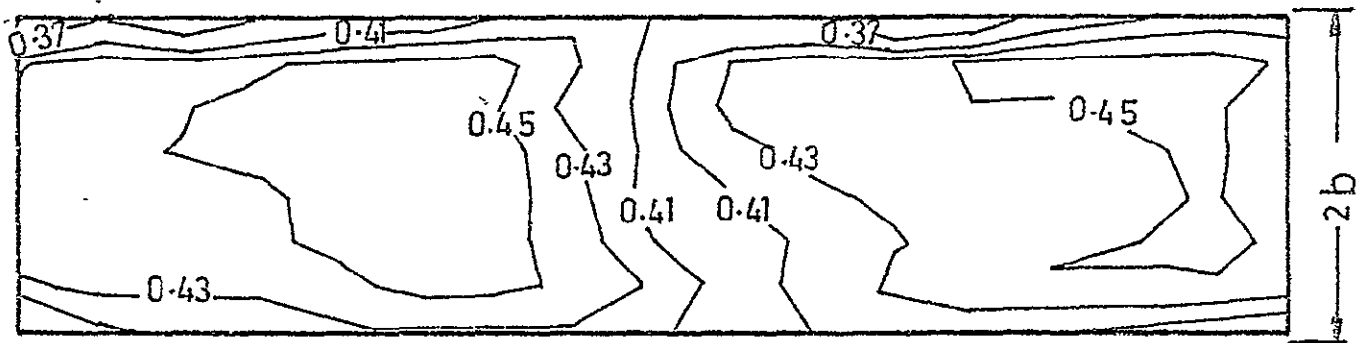
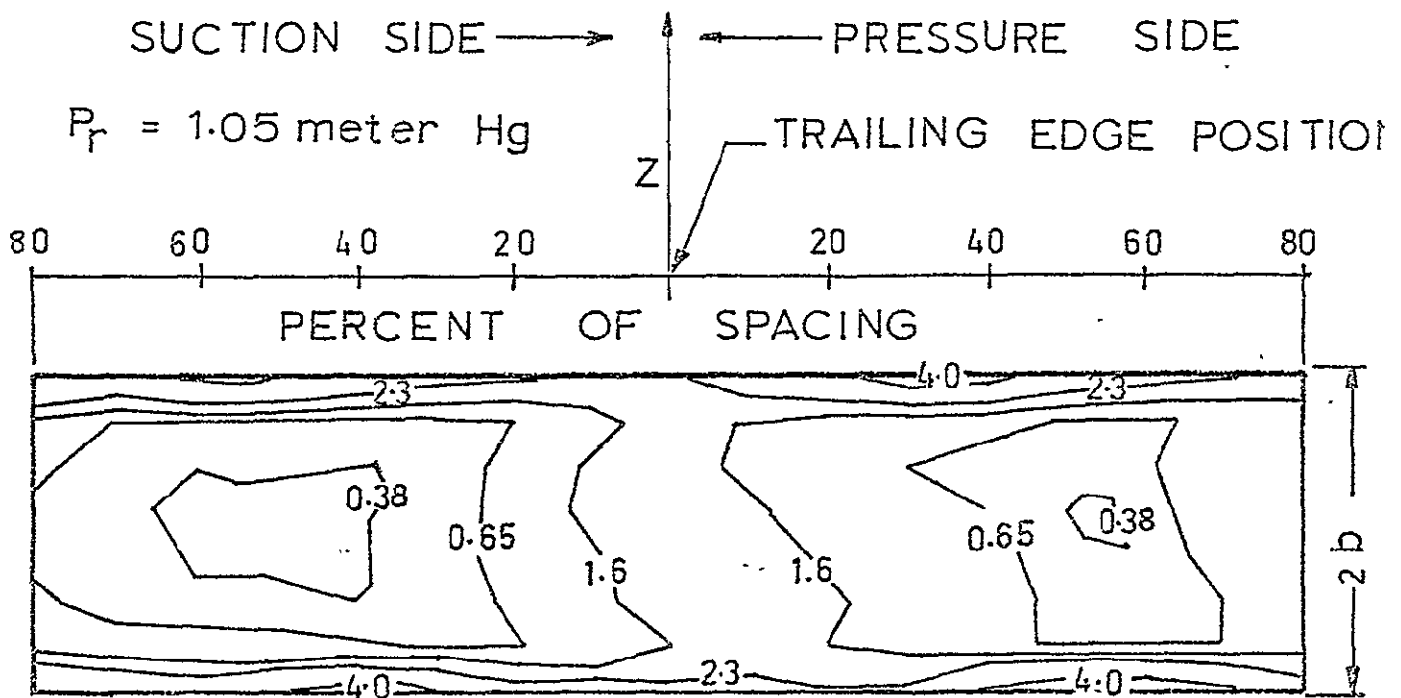


b - MACH NUMBER



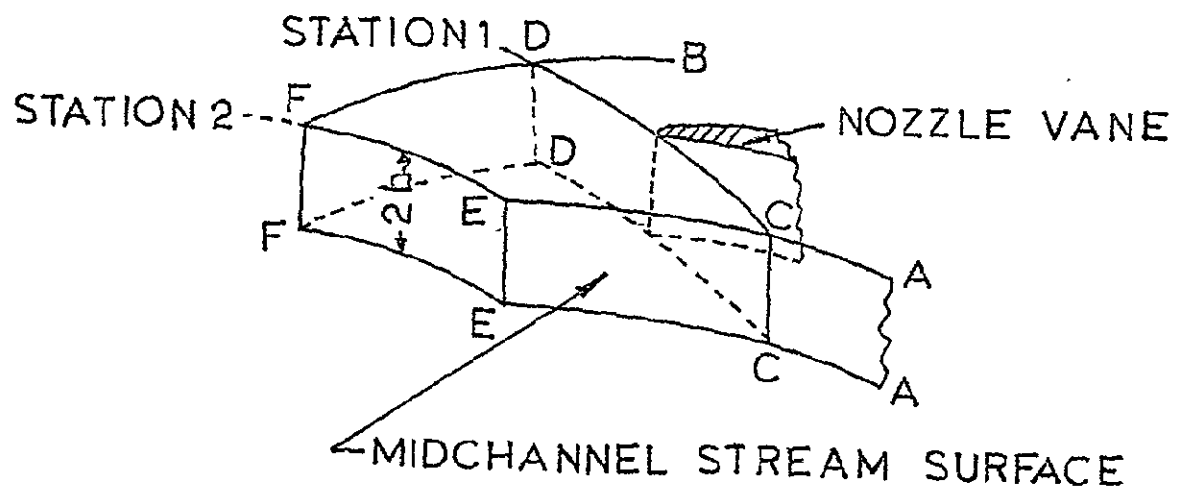
c - ANGLE α_0 (DEGREE)

FIG. 2 FLOW PROPERTIES AT STATION 0



REPRODUCIBILITY OF THE
ORIGINAL PAGE IS POOR

FIG. 3 FLOW PROPERTIES AT STATION 1



DEVELOPED VIEW

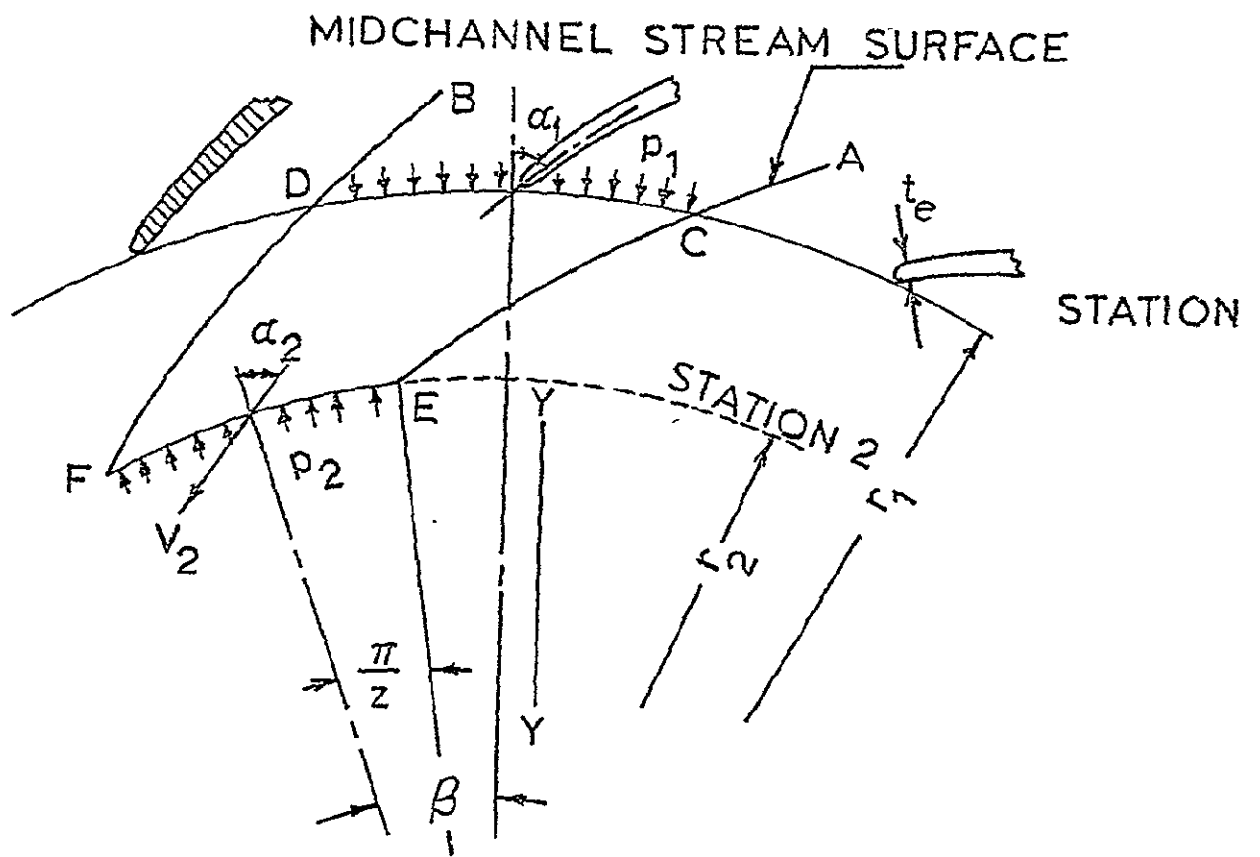


FIG. 4 CONTROL VOLUME

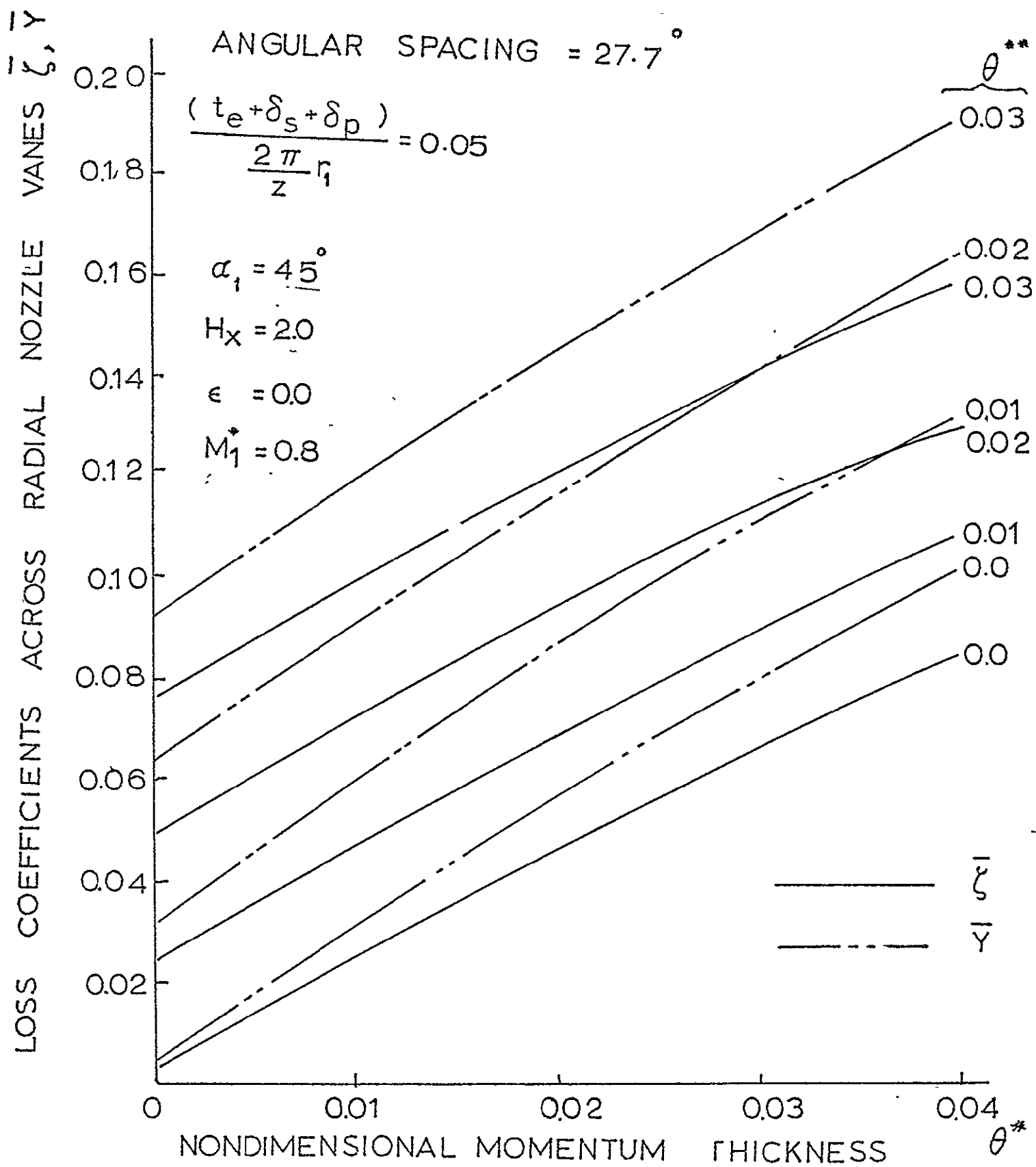


FIG. 5 LOSS COEFFICIENTS

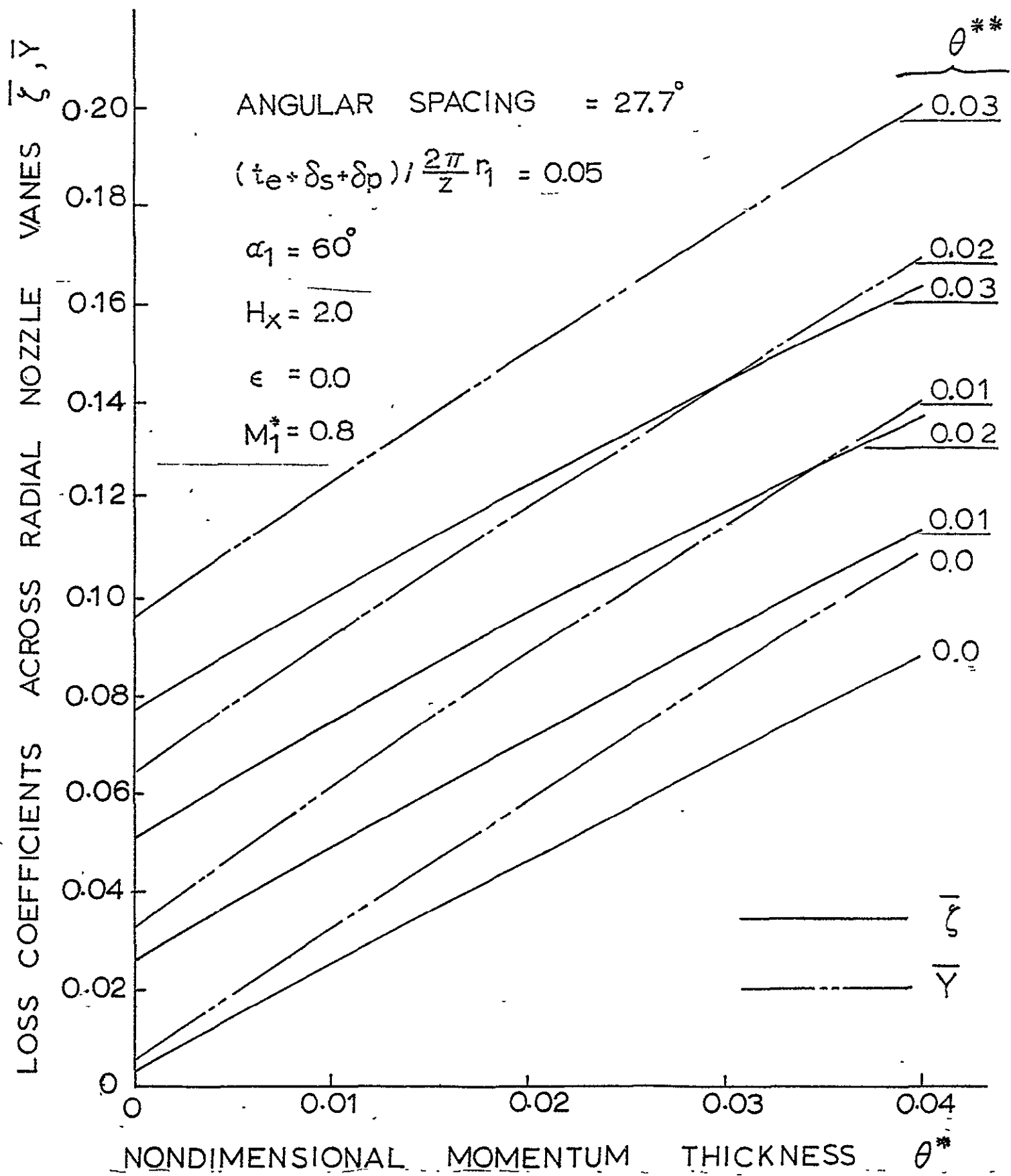


FIG. 6 LOSS COEFFICIENTS

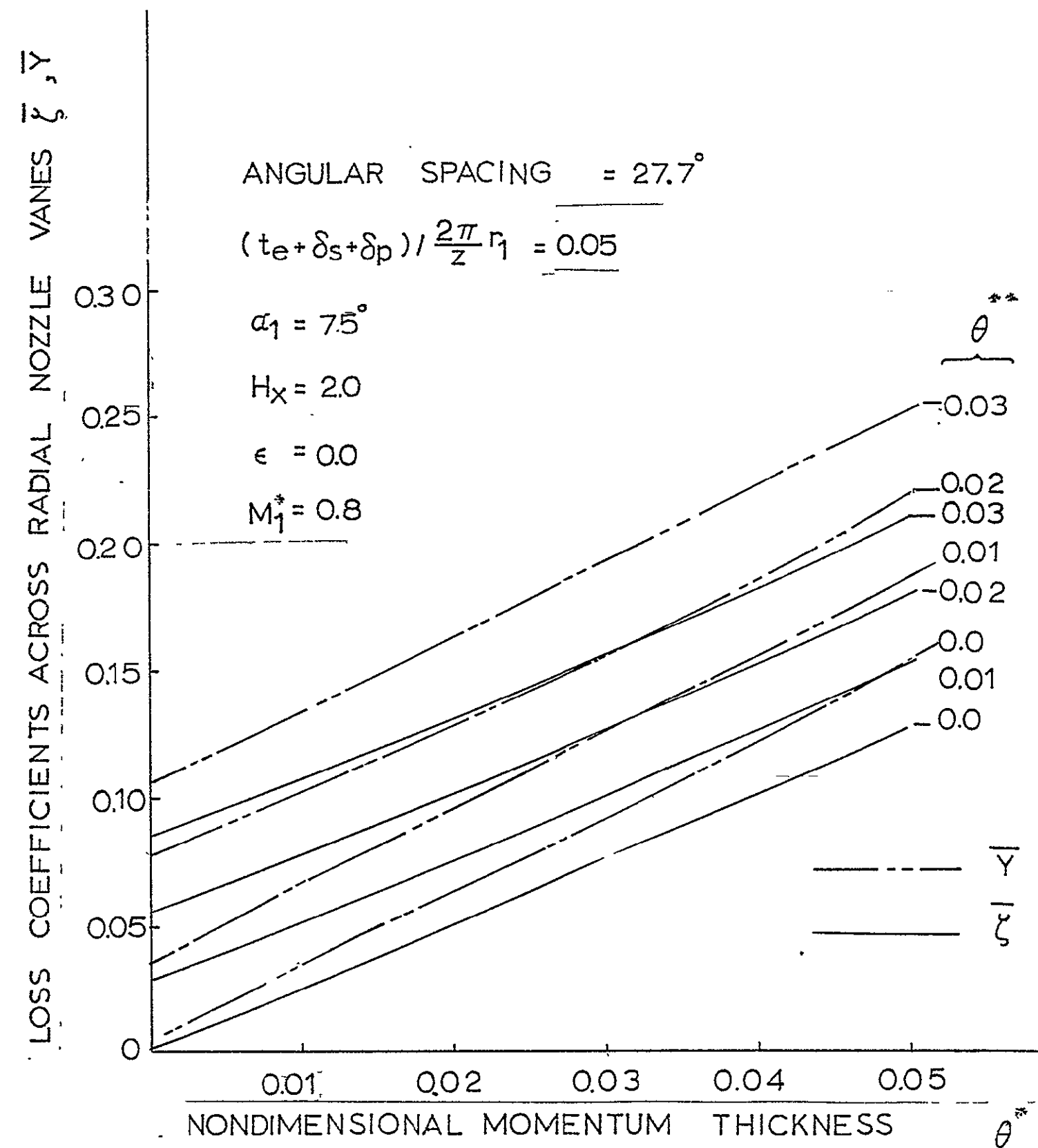


FIG. 7 LOSS COEFFICIENTS

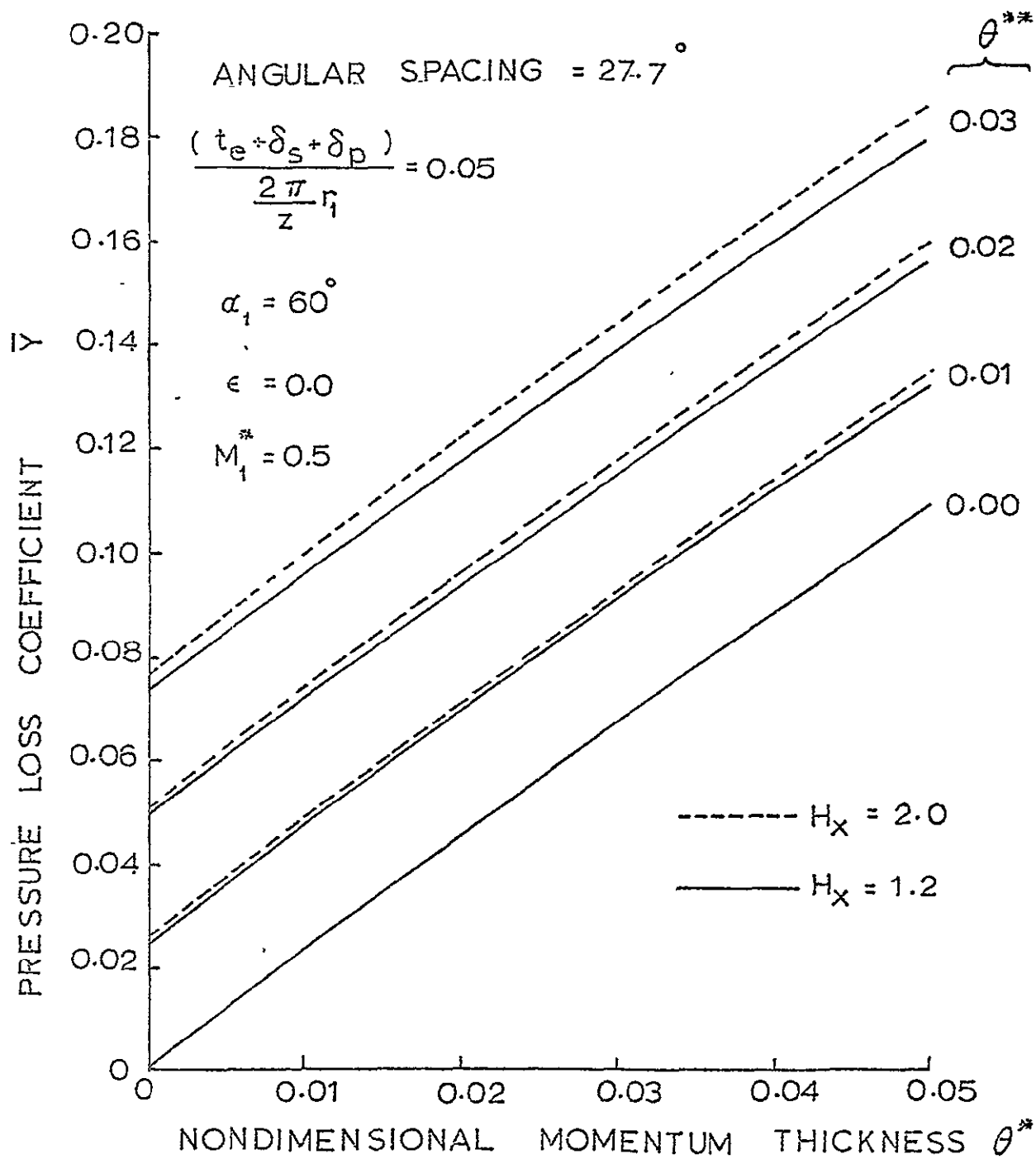


FIG. 8 EFFECT OF THE PARAMETER (H_x) ON THE LOSS COEFFICIENT \bar{Y}

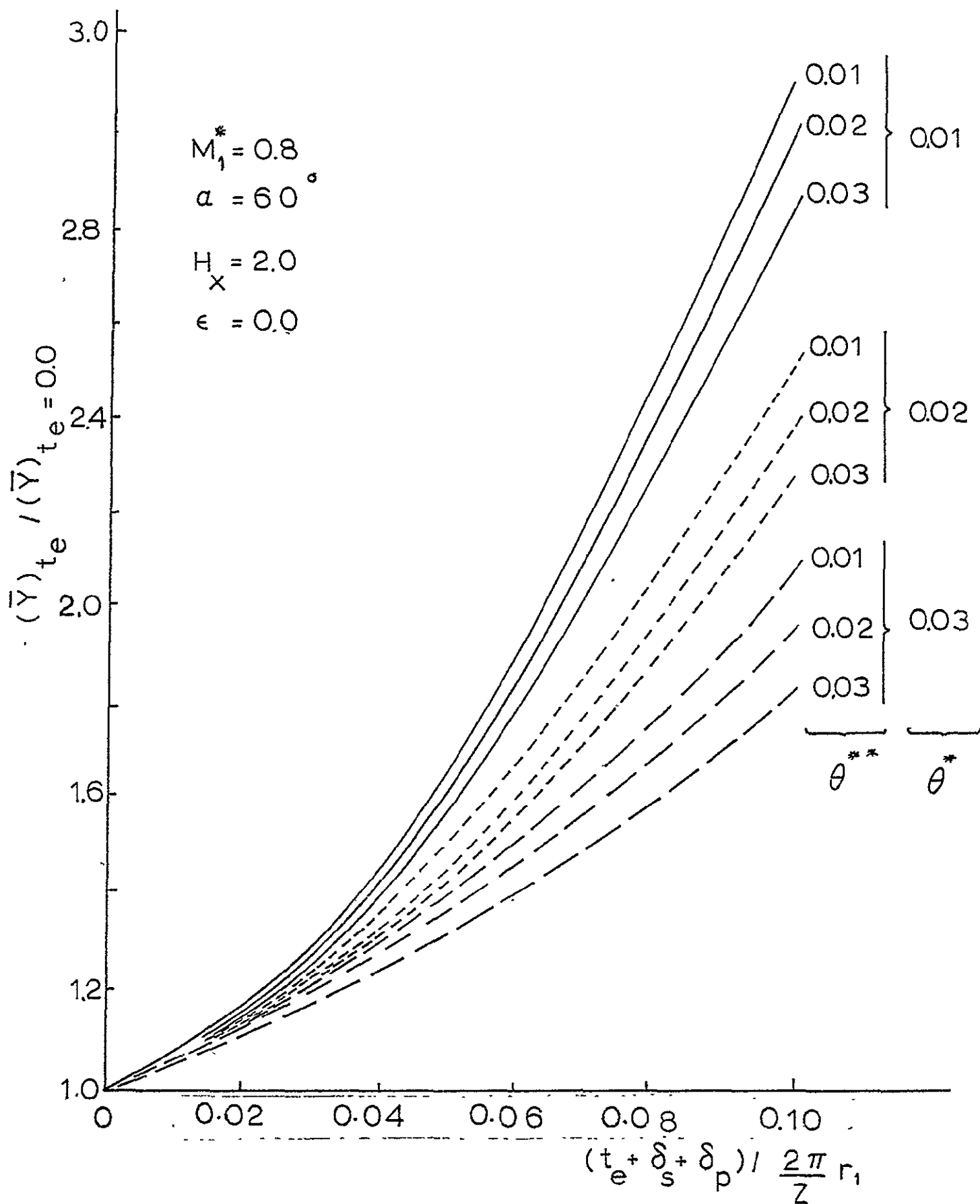


FIG.9 - EFFECT OF TRAILING EDGE THICKNESS

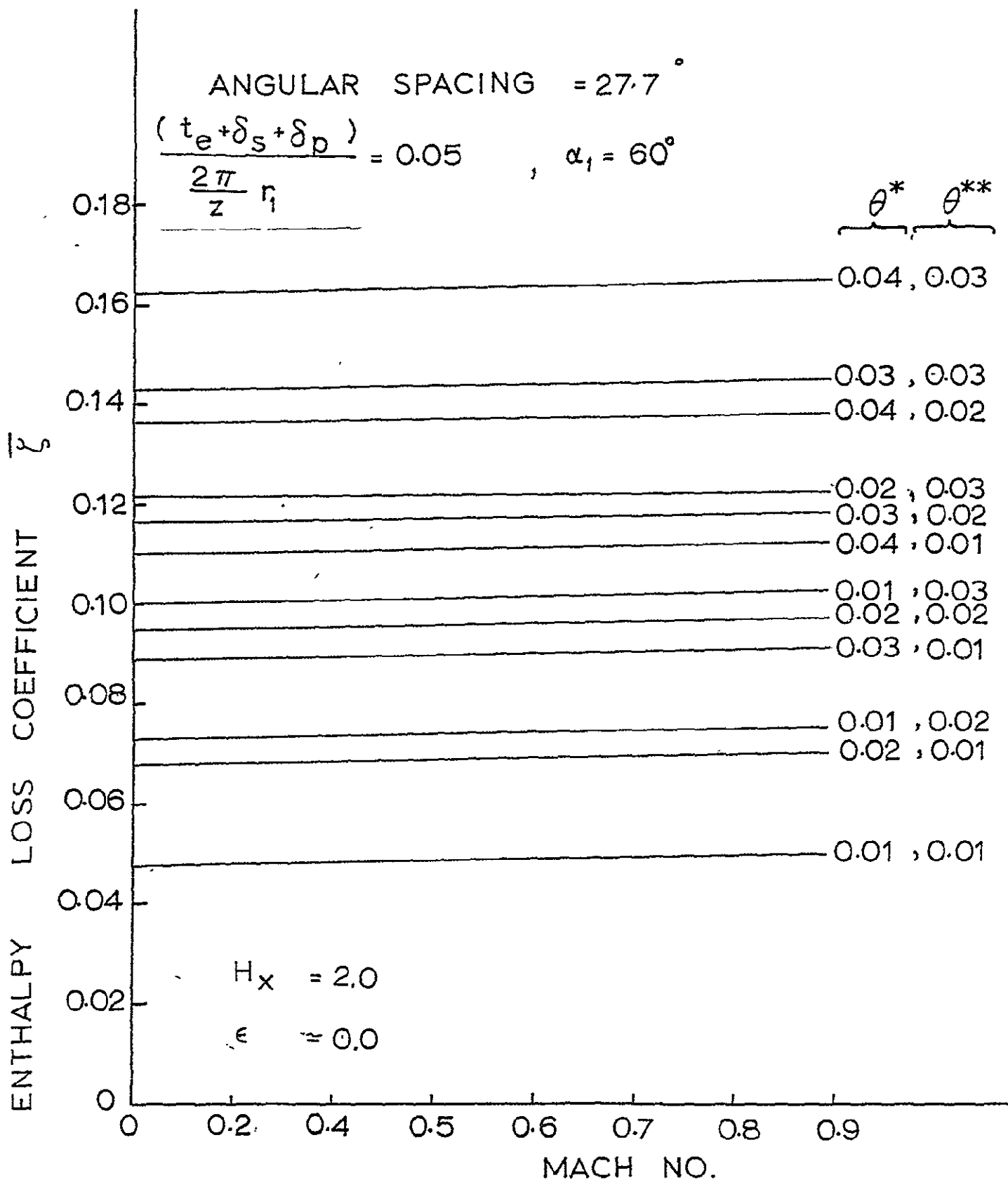


FIG.10 VARIATION OF ENTHALPY LOSS COEFFICIENT WITH MACH NO.

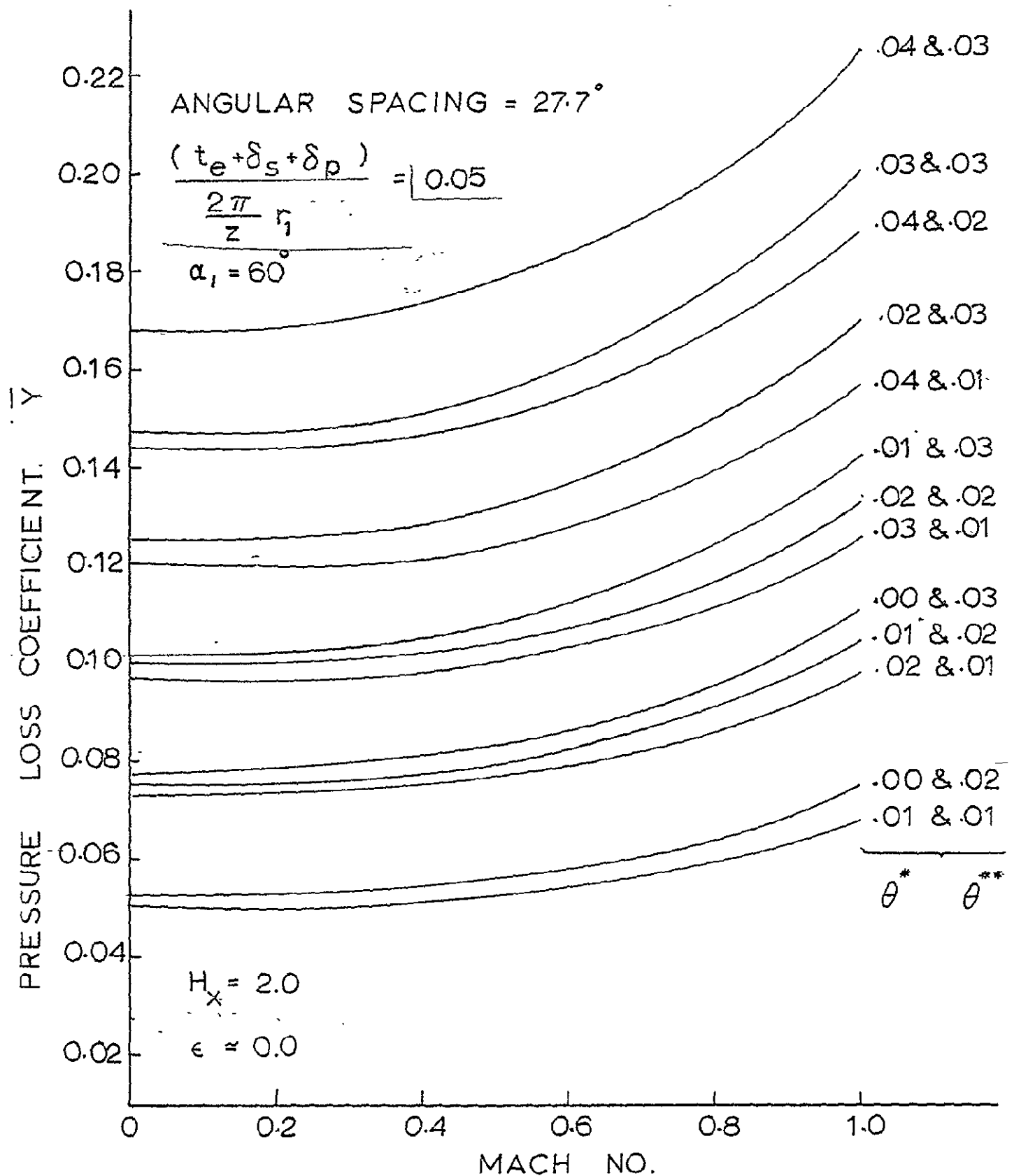


FIG. 11 : VARIATION OF PRESSURE LOSS COEFFICIENT WITH MACH NO.

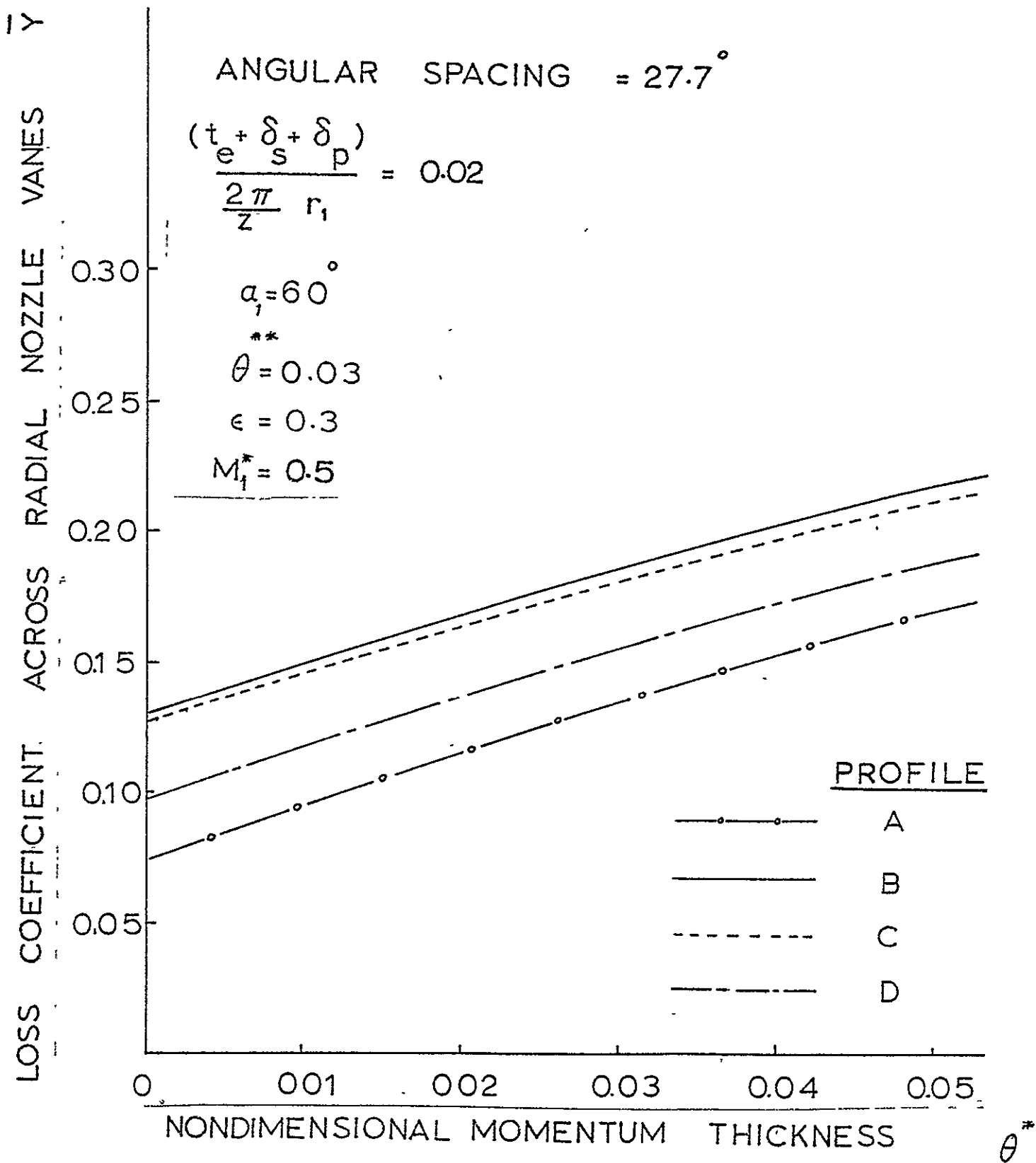


FIG 12 EFFECT OF END WALLS PROFILE
PARAMETERS ON LOSS COEFFICIENT

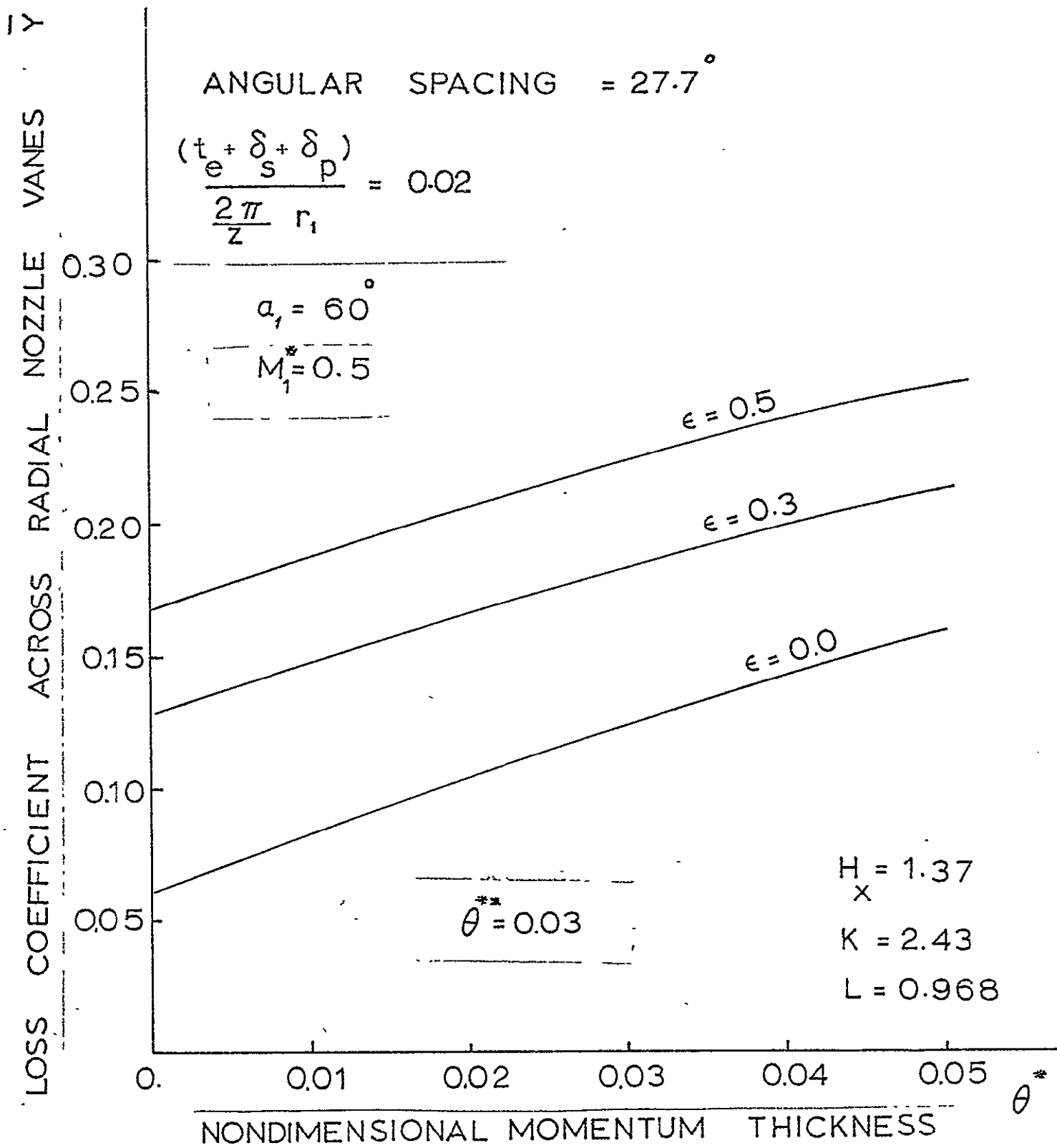


FIG.13 EFFECT OF END WALLS CROSS FLOW
PARAMETER (ϵ) - ON LOSS COEFFICIENT

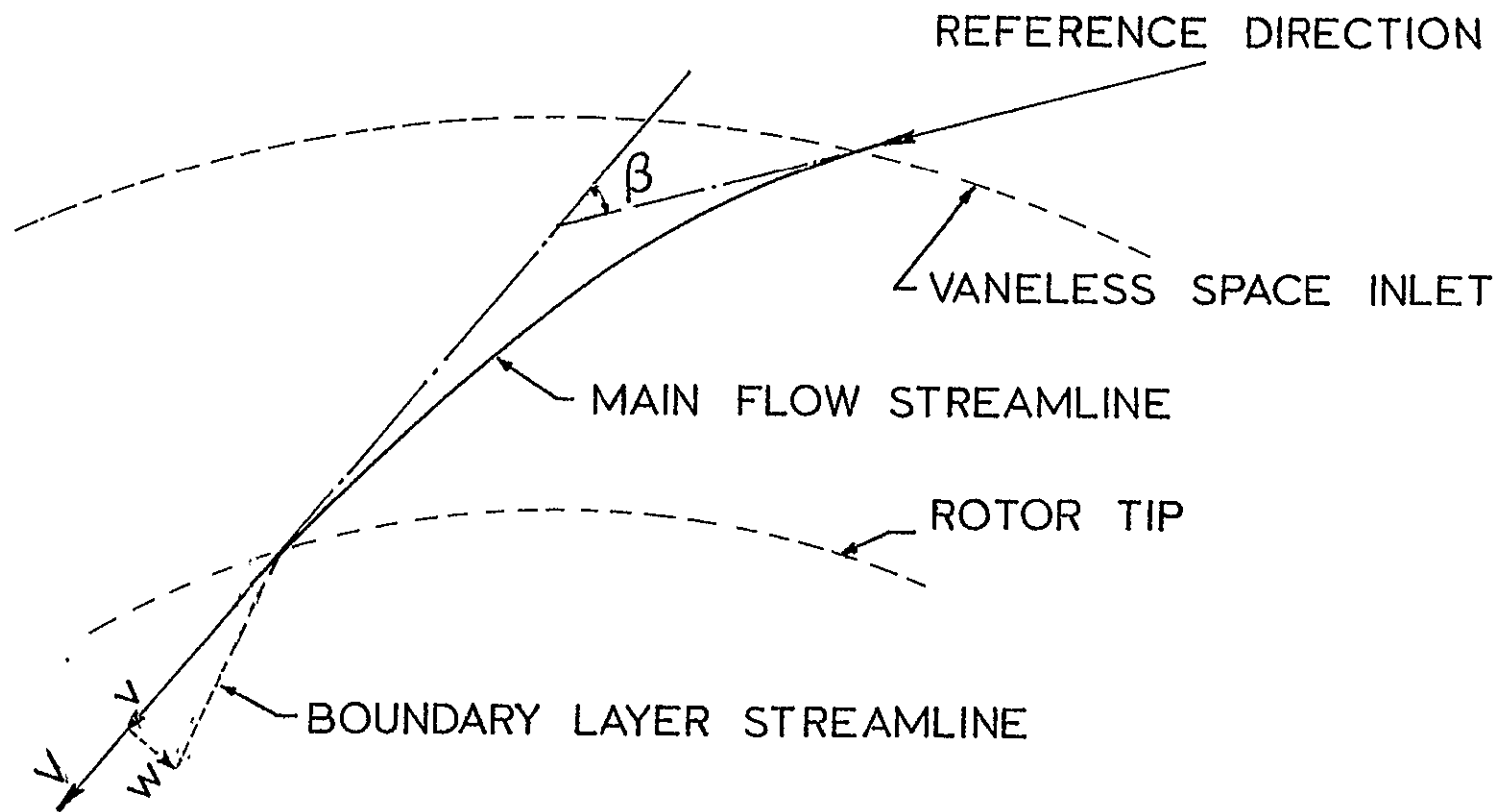
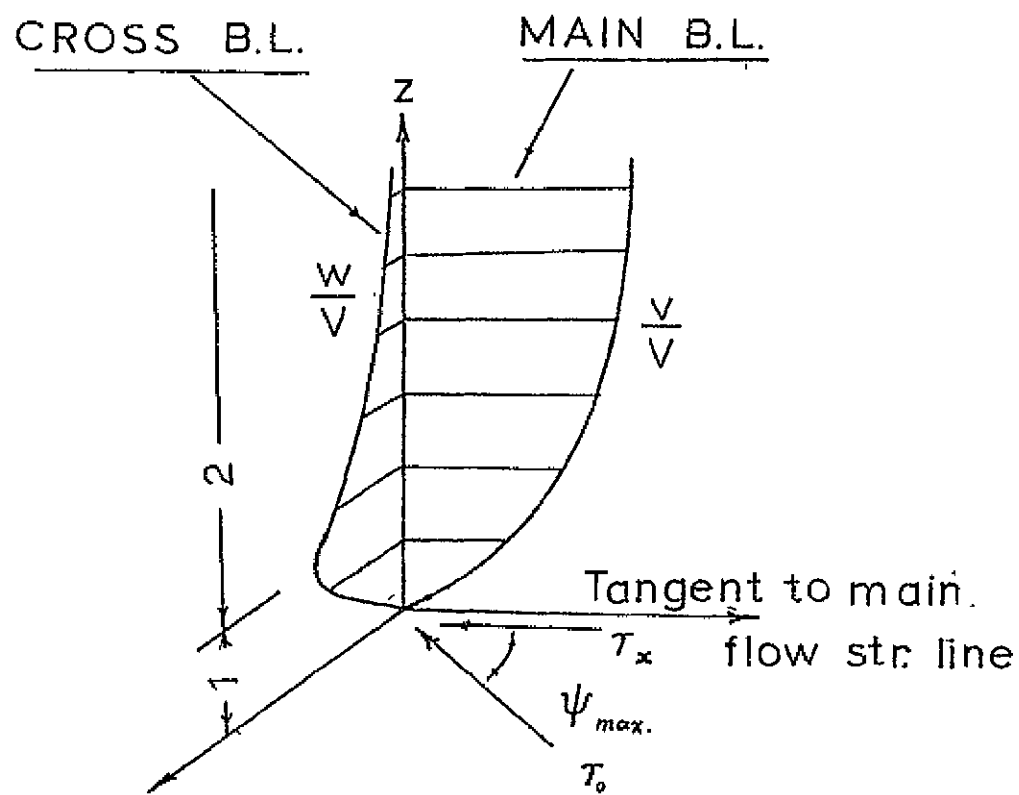
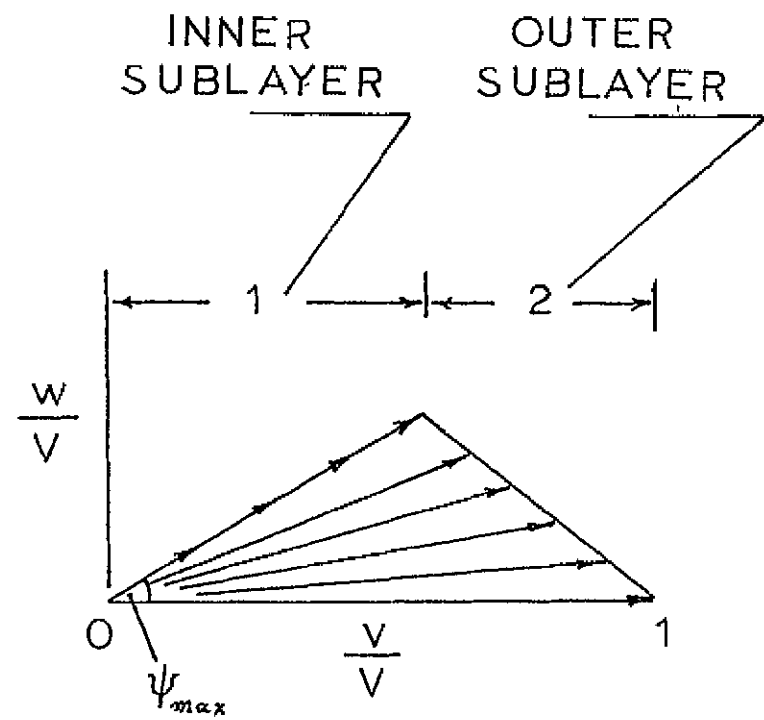


FIG.14 FLOW PATH IN THE VANELESS FIELD



a - VELOCITY PROFILES.



b - VELOCITY POLAR PLOT.

FIG. 15' END WALL BOUNDARY LAYER

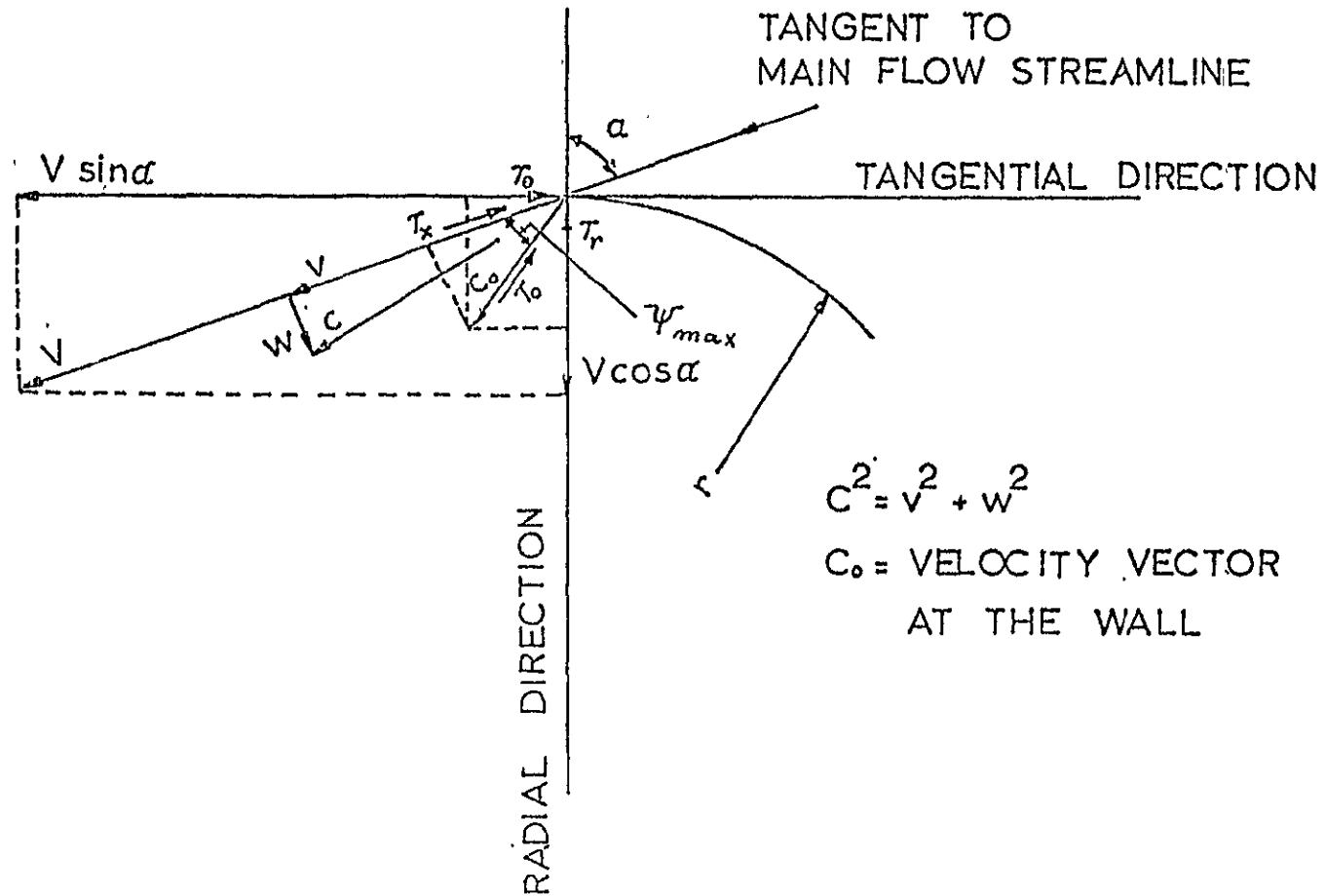


FIG. 16 VELOCITY AND WALL SHEAR STRESS COMPONENTS
IN THE SKEWED BOUNDARY LAYER

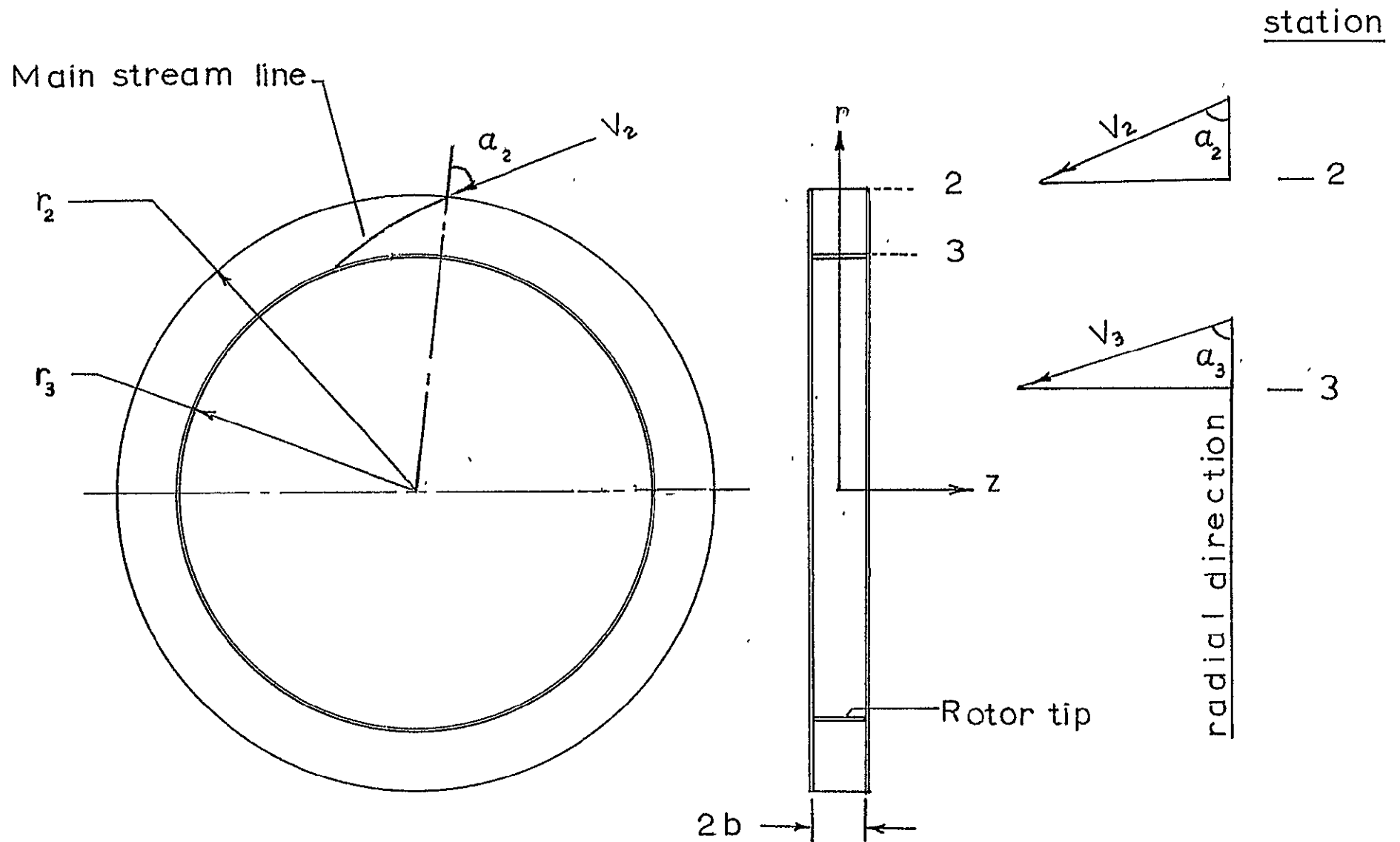
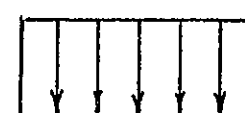
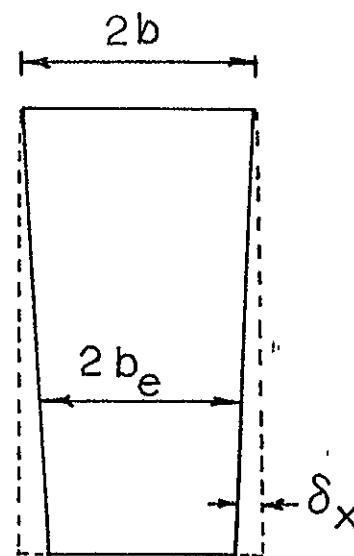
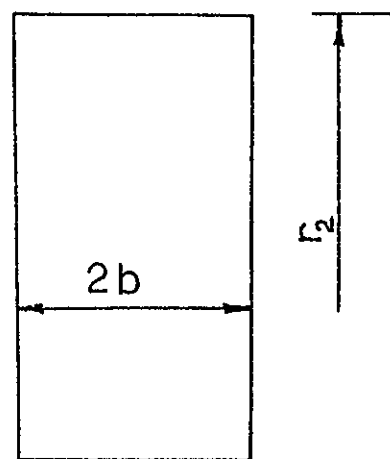
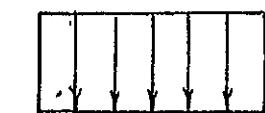
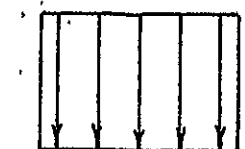


FIG 17 VANELESS SPACE GEOMETRY AND COORDINATE SYSTEM.

STATION



— r_2



— r_3

Velocity
distribution

Geometry

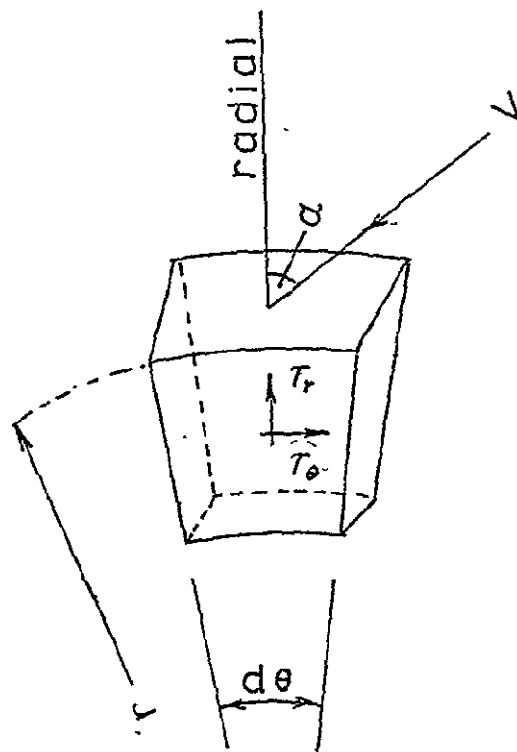
Geometry

Velocity
distribution

a - Actual case

b - Equivalent case

FIG. 18 ACTUAL AND EQUIVALENT VANELESS SPACE GEOMETRY.



Developed view

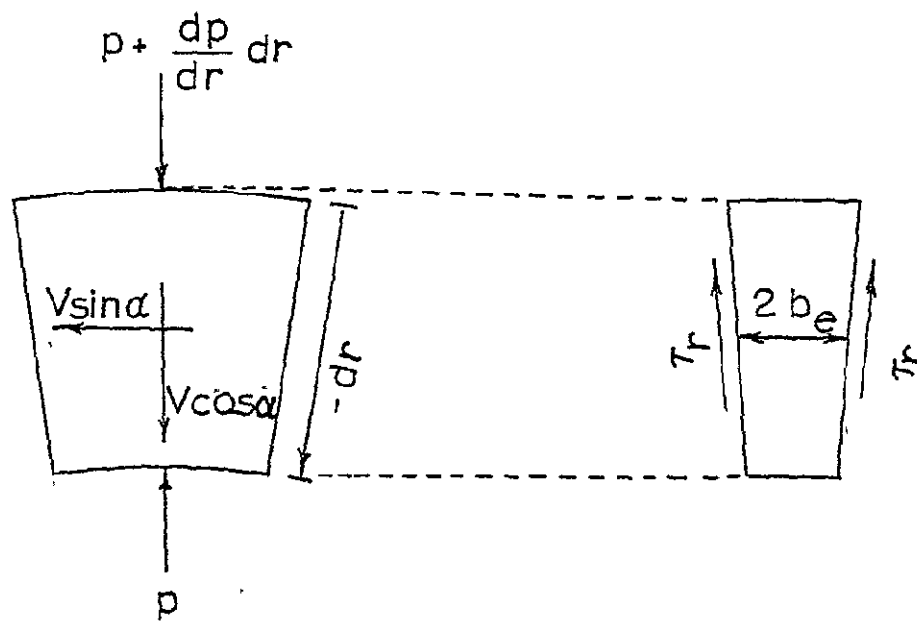


FIG. 19 CONTROL VOLUME

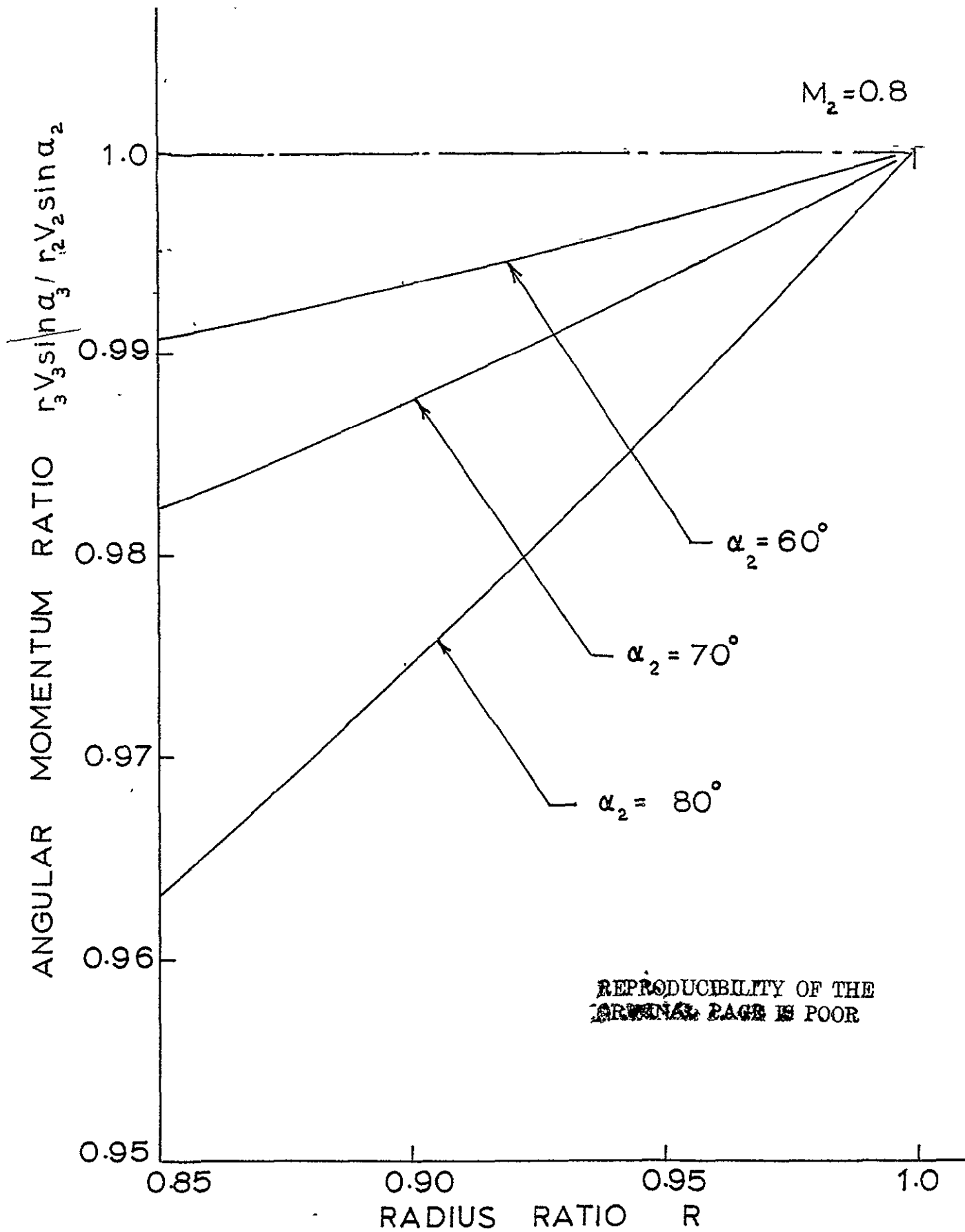


FIG. 20 EFFECT OF INLET FLOW ANGLE

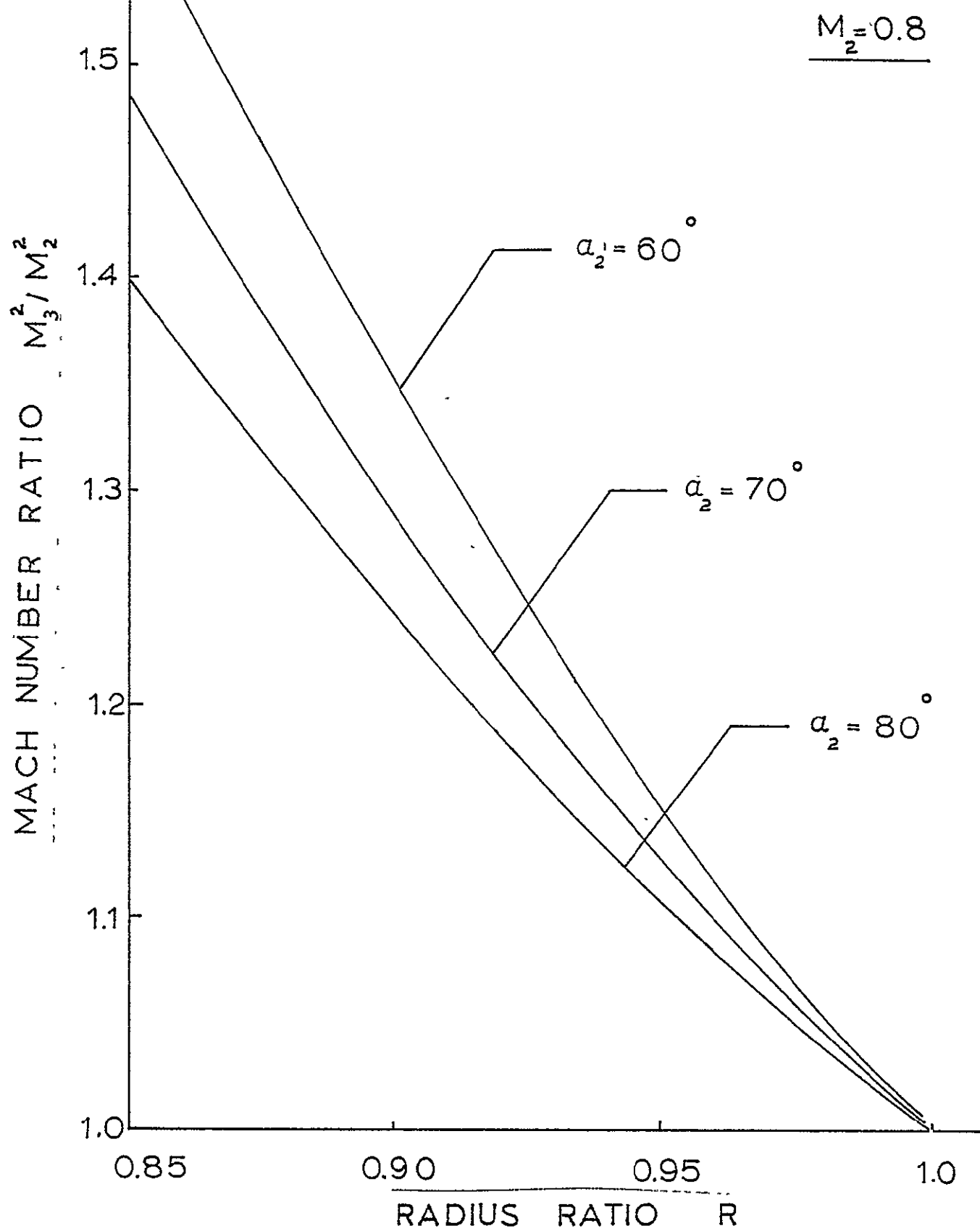


FIG. 21 : EFFECT OF INLET FLOW ANGLE

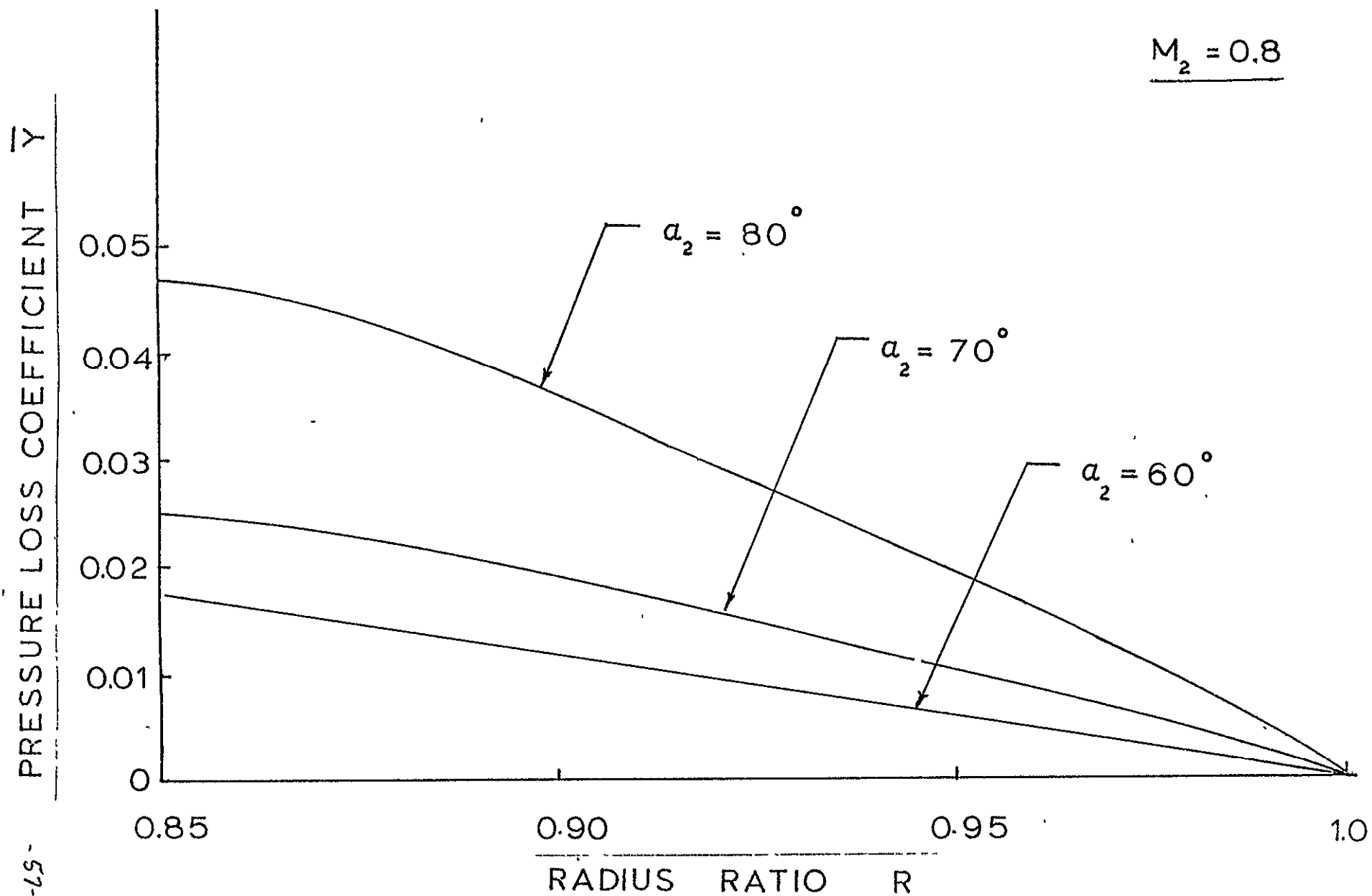


FIG. 22_a: EFFECT OF INLET FLOW ANGLE

$$M_2 = 0.8$$

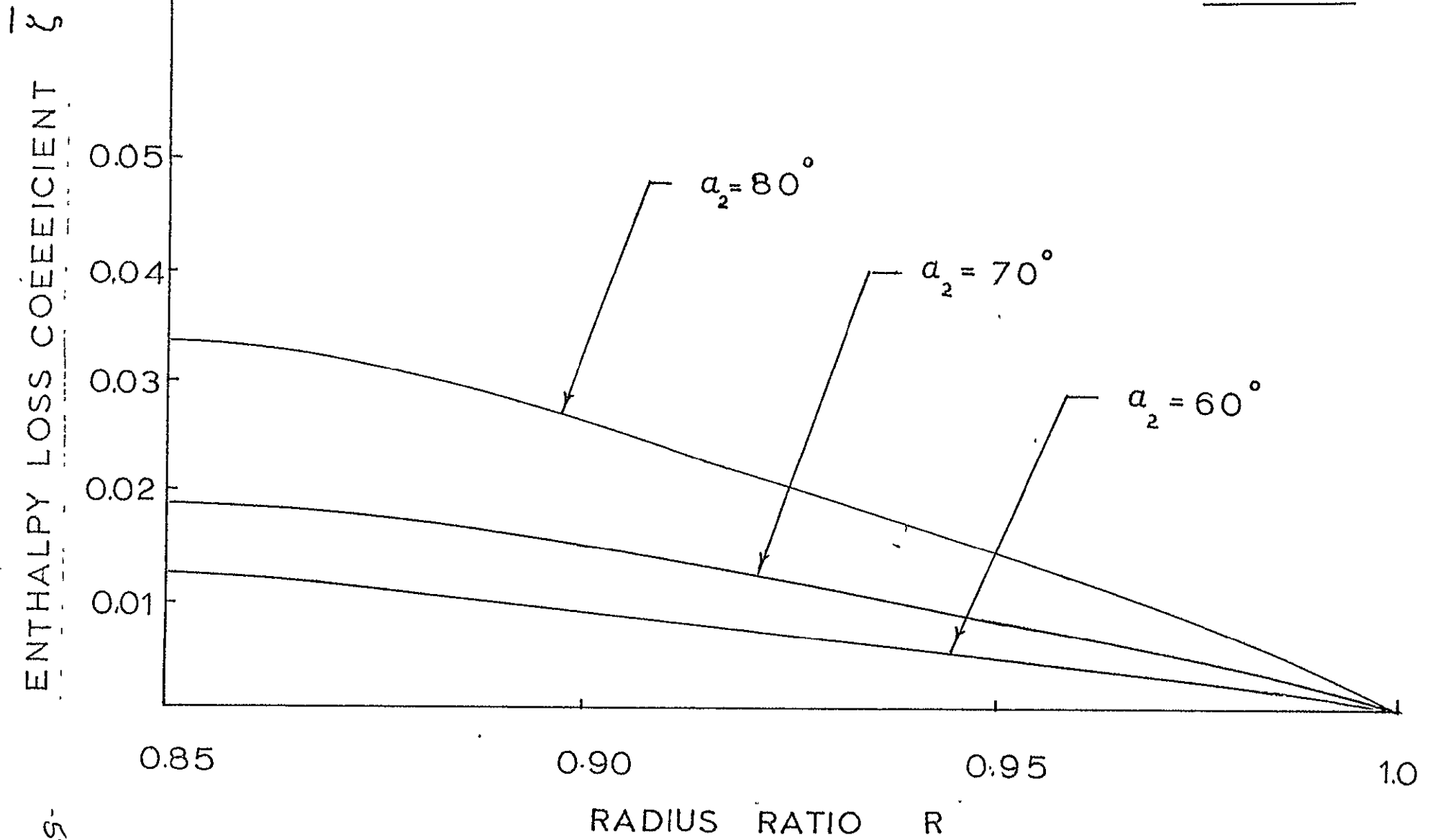


FIG. 22 b: EFFECT OF INLET FLOW ANGLE

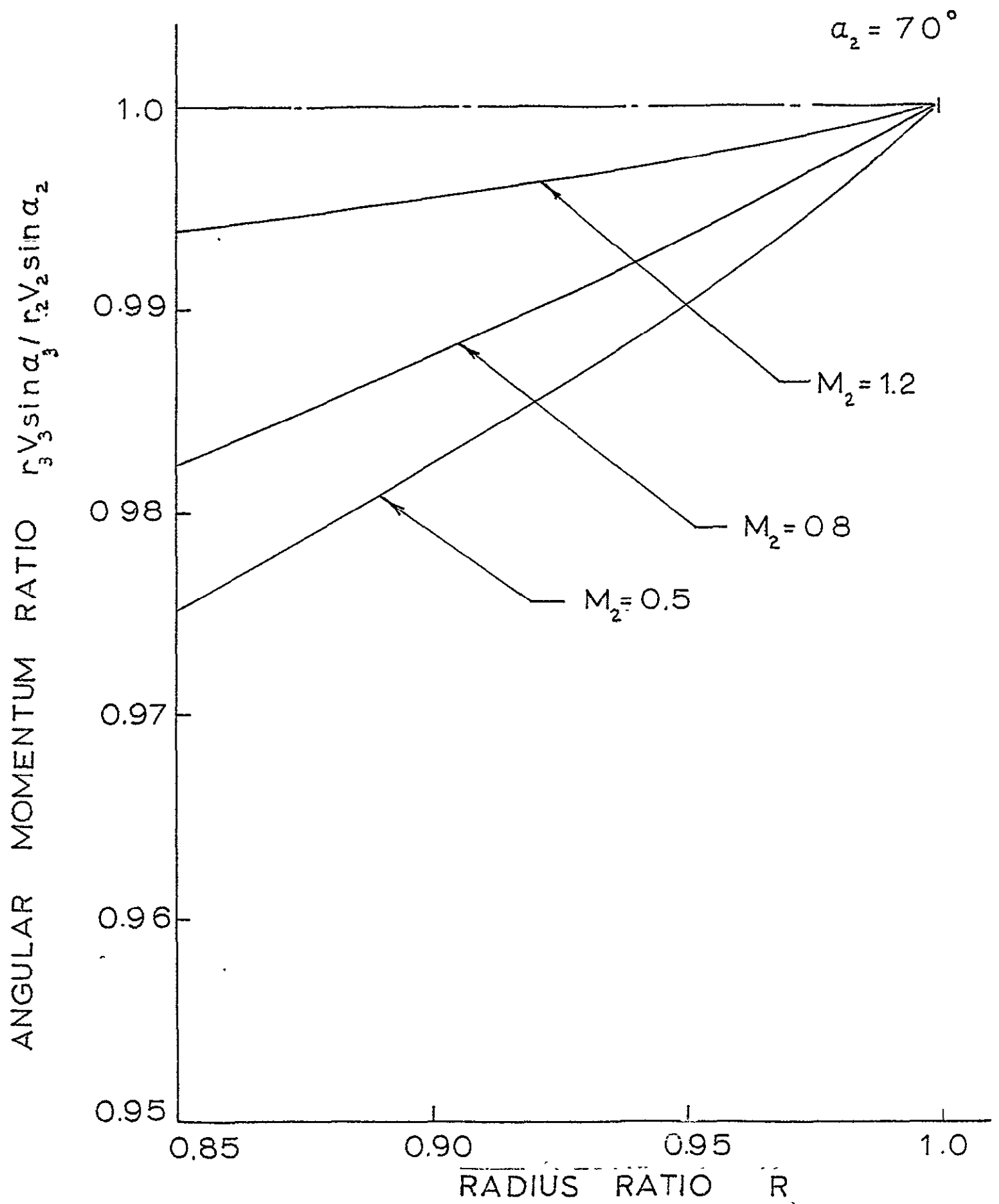


FIG. 23 : EFFECT OF INLET MACH NUMBER.

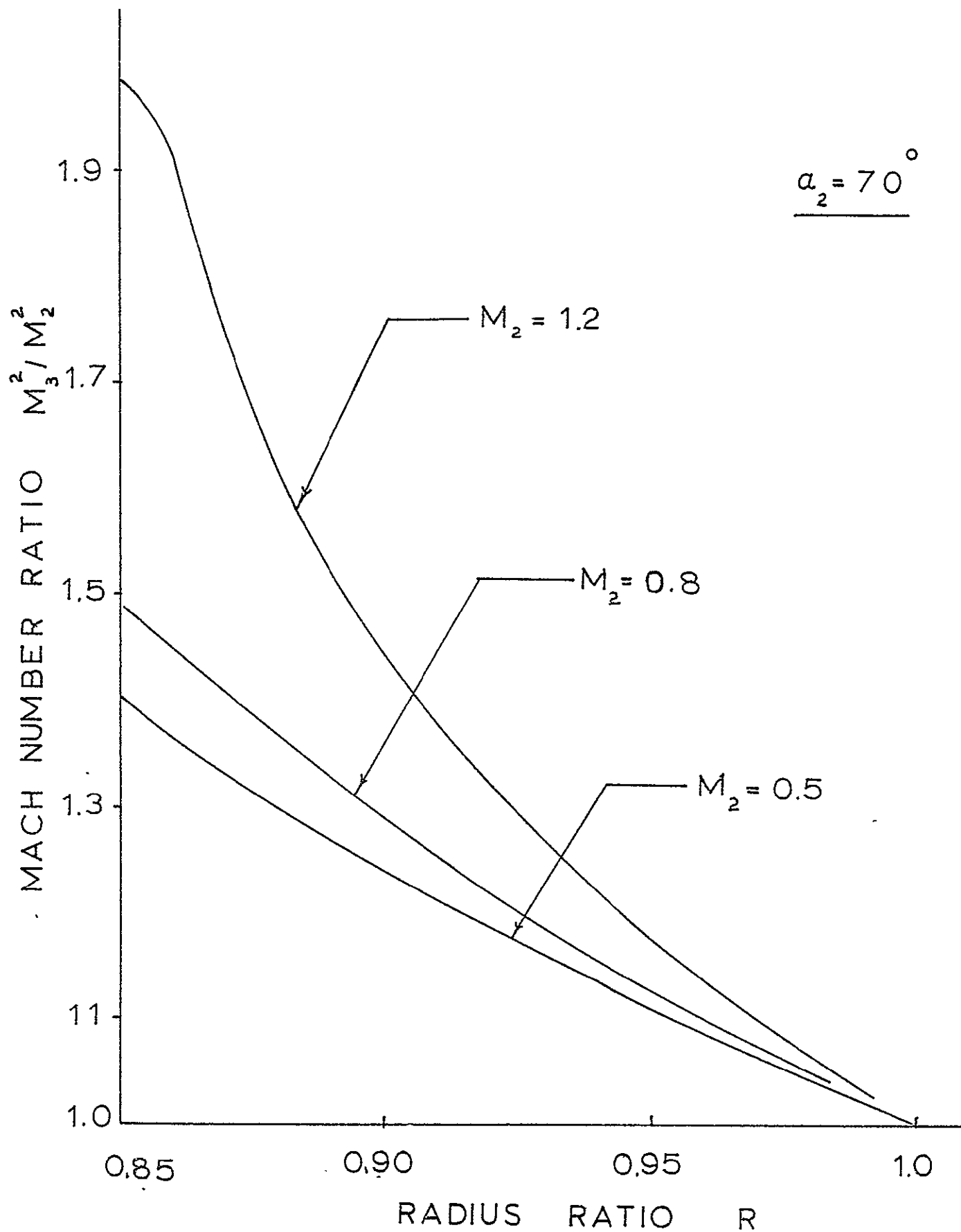


FIG. 24 EFFECT OF INLET MACH NUMBER.

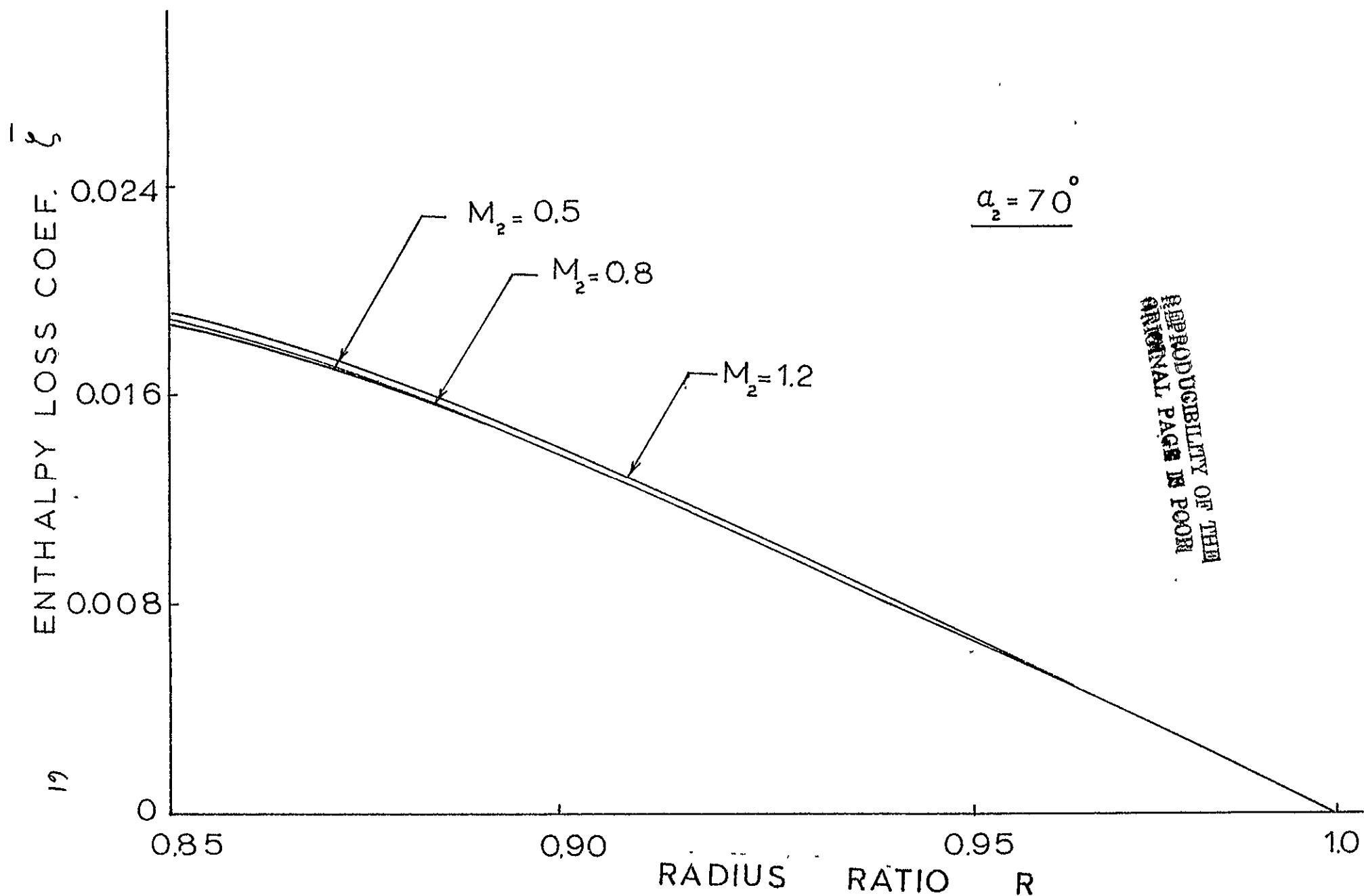


FIG.25 a: EFFECT OF INLET MACH NUMBER.

REPRODUCIBILITY OF THE
ORIGINAL PAGE IS POOR

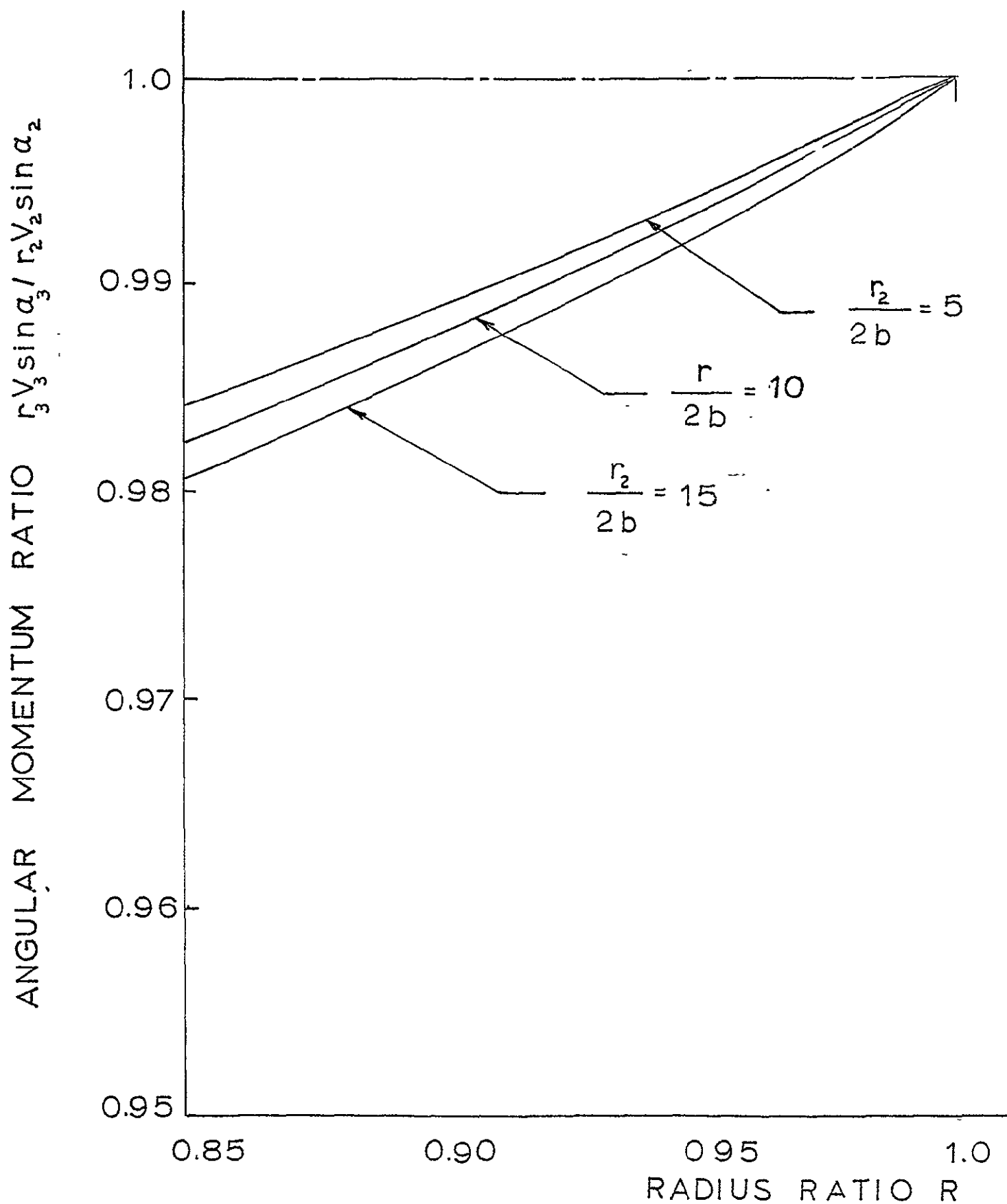


FIG. 26 : EFFECT OF END WALL SPACING.

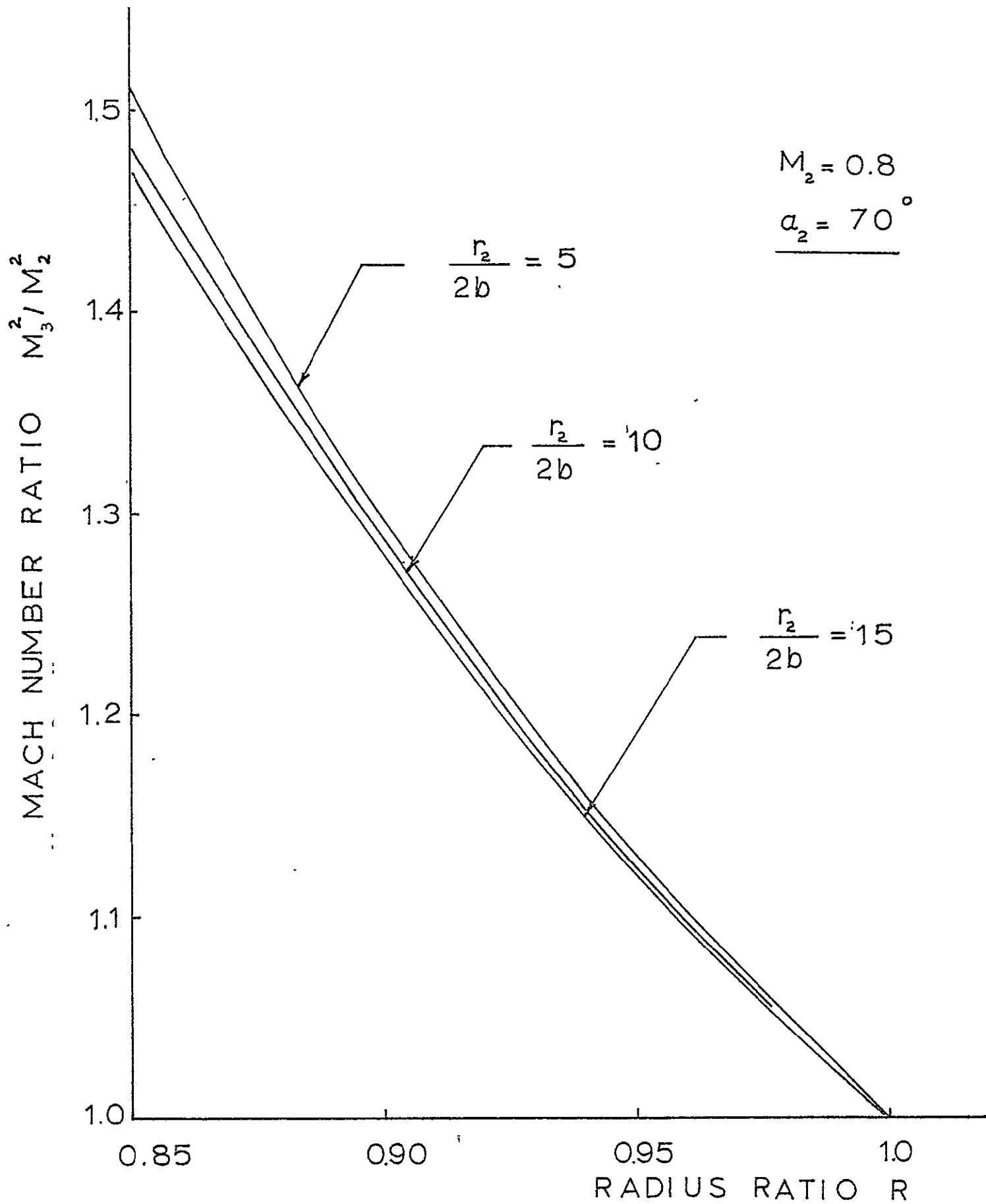


FIG. 27 : EFFECT OF END WALL SPACING.

ENTHALPY LOSS COEFFICIENT ζ

$$M_2 = 0.8$$

$$a_2 = 70^\circ$$

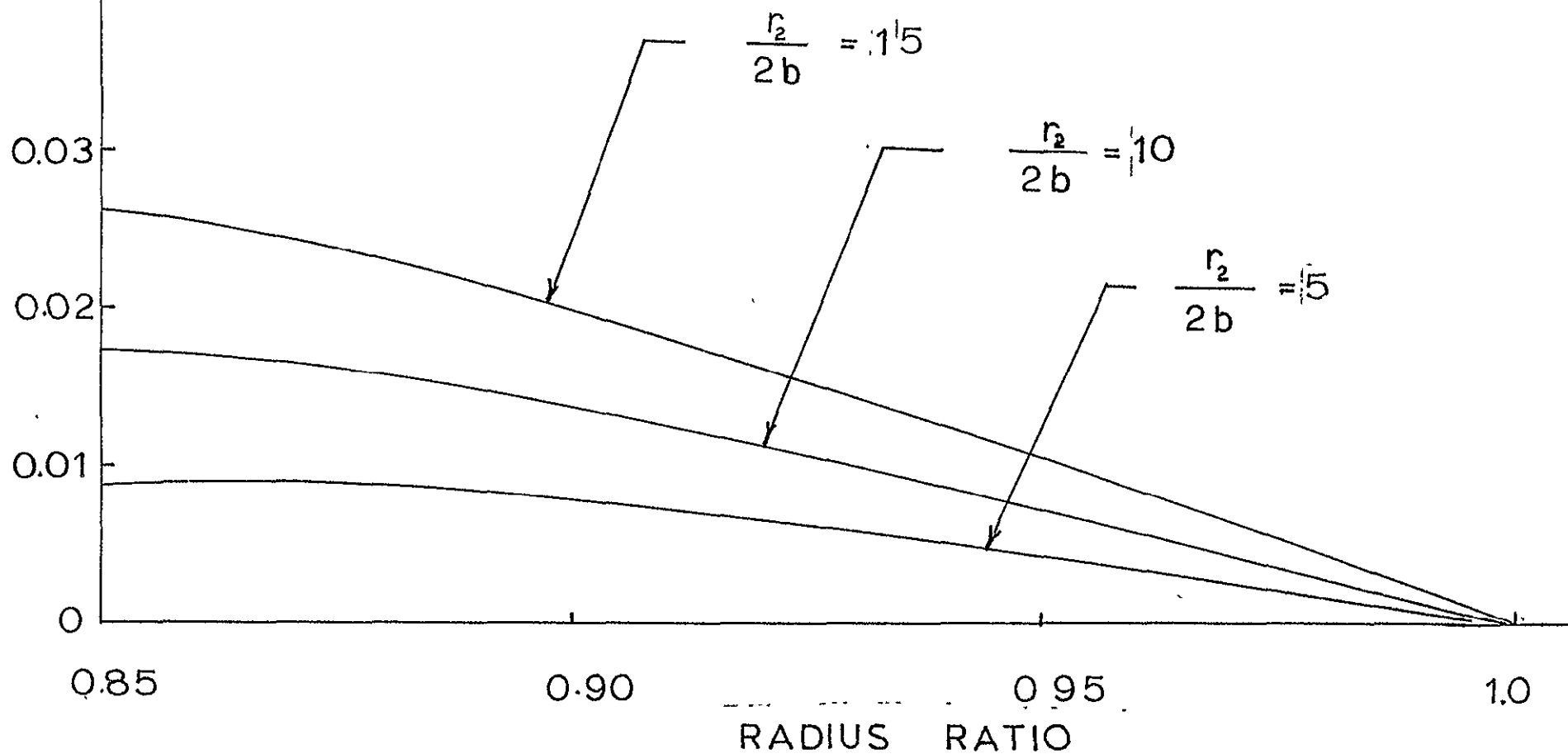


FIG. 28 a: EFFECT OF END WALL SPACING.

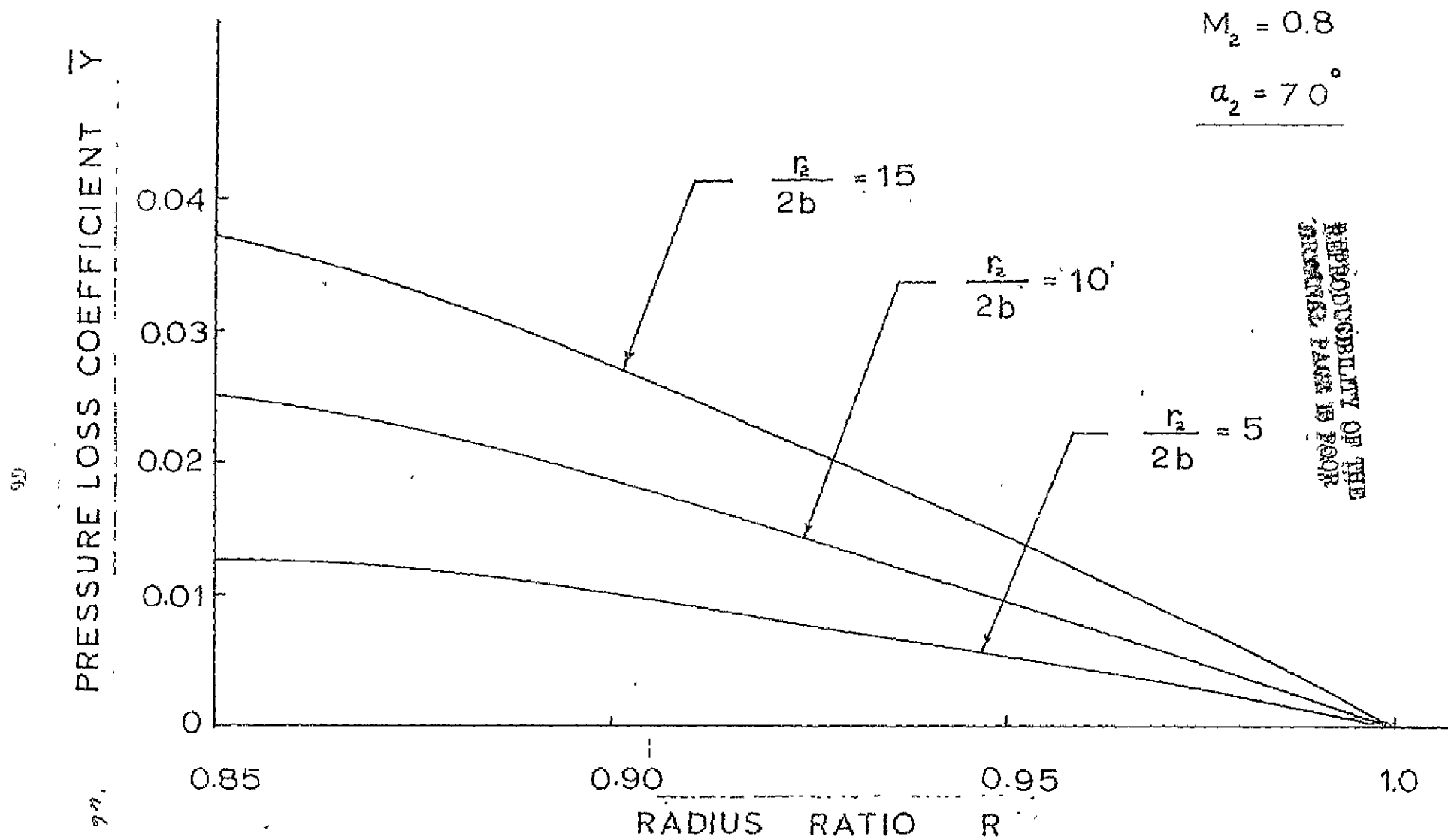


FIG. 28 b EFFECT OF END WALL SPACING..

APPENDIX A

FORMULATION OF RELATIONS BETWEEN INTEGRAL QUANTITIES AND BOUNDARY LAYER CHARACTERISTIC PARAMETERS

A.1 Basic Relations and Definitions

In this Appendix, the integrals which appear in the left hand side of Eqs. (2), (4) and (6) will be determined in terms of the boundary layer characteristics at station 1. To accomplish this, the domain of integral will be divided into a main stream region and boundary region as shown in Figure A1. This is a generalization of the approach used in the two dimensional analysis of Reference [5].

At exit from the nozzle channels the profile boundary layer developed along the vane surfaces is collateral, while the end wall boundary layer is skewed. The velocity vectors within the skewed boundary layer can hence be resolved into a streamwise component v , and a cross flow component w . The displacement and momentum thicknesses are used to describe the boundary layers at station 1. These two quantities for the collateral boundary layer are defined as:

$$\delta = \delta_f - \int_0^{\delta_f} \frac{\rho V}{(\rho V)_\infty} dn \quad (A1)$$

$$\theta = \int_0^{\delta_f} \frac{\rho V}{(\rho V)_\infty} dn - \int_0^{\delta_f} \frac{\rho V^2}{(\rho V^2)_\infty} dn \quad (A2)$$

Where n is the coordinate normal to the vane surface and δ_f is the boundary layer thickness. On the other hand, the streamwise and cross flow end wall boundary layer displacement and the momentum thickness are defined as follows:

$$\delta_x = \delta_f - \int_0^{\delta_f} \frac{\rho v}{(\rho v)_\infty} dz \quad (A3)$$

$$\theta_x = \int_0^{\delta_f} \frac{\rho v}{(\rho V)_\infty} dz - \int_0^{\delta_f} \frac{\rho v^2}{(\rho V^2)_\infty} dz \quad (A4)$$

$$\delta_c = \int_0^{\delta_f} \frac{\rho w}{(\rho V)_\infty} dz \quad (A5)$$

$$\theta_c = \int_0^{\delta_f} \frac{\rho w^2}{(\rho V^2)_\infty} dz \quad (A6)$$

Where z is the coordinate normal to the end wall surface.

The relation between the parameters of equations (A3) through (A6) can be determined for a given boundary layer profile. It is assumed that in the end wall boundary layer the streamwise and the cross flow velocity profiles are given by Reference [6].

$$\frac{v}{V_{fs}} = G \quad , \quad \frac{w}{V_{fs}} = \epsilon G g \quad (A7)$$

In the above equations G and g are functions of the coordinate perpendicular to the end wall, z , normalized with respect to the boundary layer thickness (δ_f), ϵ is the tangent of the angle, Ψ , between the surface shear and the local main flow direction as shown in Fig. A2.

The following streamwise and cross flow parameters are used to describe the end wall boundary layers using the assumed formes of the velocity profiles:

$$H_x = \frac{\delta_x}{\theta_x} = \frac{\int_0^{\delta_f} (1-\mu G) dz}{\int_0^{\delta_f} \mu \{1-G\} G dz} \quad (A8)$$

$$K = \frac{\delta_c}{\epsilon \theta_x} = \frac{\int_0^{\delta_f} \mu (Gg) dz}{\int_0^{\delta_f} (\mu - \mu G) G dz} \quad (A9)$$

$$L = \frac{\theta_c}{\epsilon^2 \theta_x} = \frac{\int_0^{\delta_f} \mu (Gg)^2 dz}{\int_0^{\delta_f} (\mu - \mu G) (G) dz} \quad (A10)$$

Where μ is the nondimensional ratio ρ/ρ_∞ .

In Ref. [7] various families of functions G and g that are most compatible with the experimental data were determined. The corresponding profiles are plotted in Fig. A3, together with the Band, "B", of the experimental data obtained by Johnson [6]. The various parameters of Eqs. (A12), (A13) and (A14) were calculated for the incompressible flow corresponding to the profiles of Fig. A3, and are given in the following table.

Profile	H_x	K	L
A	1.286	0.457	0.0359
B	1.37	2.43	0.968
C	1.40	2.27	0.989
D	1.286	1.249	0.262

TABLE A-1: TYPICAL VALUES FOR THE END WALL BOUNDARY LAYER
CHARACTERISTIC PARAMETERS.

A.2 Evaluation of the Different Integral Terms in the Governing Equations

The integrals in the Governing Equations (2), (4) and (6) will be expressed in terms of the boundary layer parameters of Eqs. (A1) through (A10) based on the following assumptions:

1. Different boundary layers do not interfere with each other, hence corner effects are neglected.
2. The flow is homogeneous outside the boundary layer regions at exit from the nozzle channels.

In accordance with the foregoing assumption, the velocity distribution of Figure A3 due to the profile boundary layers on the vane surfaces will result in the variation of the total pressure in the tangential direction shown in Figure A4. The total pressure and velocity deficiencies in the axial direction caused by the end wall boundary layers will be similar to those indicated in Figures A5 and A6.

Referring to Figure A2, the following equations relate the different skewed end wall boundary layer velocity components and flow angles:

$$V \cos \alpha = v \cos \alpha_1 + w \sin \alpha_1 \quad (\text{A12})$$

$$v^2 \cos \alpha \sin \alpha = v^2 \cos \alpha_1 \sin \alpha_1 - w^2 \cos \alpha_1 \sin \alpha_1 \quad (\text{A13})$$

and $v^2 \cos^2 \alpha$ may be approximated by

$$v^2 \cos^2 \alpha = v^2 \cos^2 \alpha_1 + w^2 \sin^2 \alpha_1 \quad (\text{A14})$$

Where α is the angle between the flow direction and the radial inward direction as before, while α_1 is the same angle for the local free stream at station 1, which is independent of z and θ according to the assumptions.

A.2.1 Evaluation of the Integral $\int_{-b}^{+b} \left[\int_{-\pi/Z}^{+\pi/Z} (\rho V r \cos \alpha)_1 d\theta \right] dz$

Referring to Figure A1, it is more convenient to breakup the above integration into three separate integrals as follows:

$$\begin{aligned} \int_{-b}^{+b} \left[\int_{-\pi/Z}^{+\pi/Z} (\rho V r \cos \alpha)_1 d\theta \right] dz &= \cos \alpha_1 r_1 \int_{-b+\delta_{lf}}^{+b-\delta_{uf}} \left[\int_{-\pi/Z}^{+\pi/Z} (\rho V)_1 d\theta \right] dz \\ &+ r_1 \left\{ \int_{-b}^{-b+\delta_{lf}} \left[\int_{-\pi/Z}^{+\pi/Z} (\rho V \cos \alpha)_1 d\theta \right] dz + \int_{b-\delta_{uf}}^b \left[\int_{-\pi/Z}^{+\pi/Z} (\rho V \cos \alpha)_1 d\theta \right] dz \right\} \end{aligned} \quad (A15)$$

where

δ_{uf} , δ_{lf} are the full boundary layer thicknesses over the upper and lower end wall surfaces.

Referring to Figure A2, the coordinate used in the profile boundary layer equations is related to the circumferential coordinate θ by:

$$d\theta = \frac{dn}{r_1 \cos \alpha_1} \quad (A16)$$

Substituting the above expression for $d\theta$ in the first term in the right hand side of equation (A15), and using the definition of the displacement thickness of Equation (A1) we can arrive at:

$$\int_{-b+\delta_{lf}}^{+b-\delta_{uf}} \left[\int_{-\pi/Z}^{+\pi/Z} (\rho V)_1 d\theta \right] dz = [2b - (\delta_{uf} + \delta_{lf})] (\rho V)_\infty \frac{2\pi}{Z} [1 - \delta^* - \delta_{te}] \quad (A17)$$

where

$$\delta^* = (\delta_s + \delta_p) / \frac{2\pi}{Z} r_1 \cos \alpha_1 \quad (A18)$$

$$\delta_{te} = te / \frac{2\pi}{Z} r_1 \cos \alpha_1 \quad (A19)$$

and

δ_s, δ_p are the boundary layer displacement thickness over suction and pressure surfaces of the vane.

t_e is the vane trailing edge thickness.

$\frac{2\pi}{Z}$ is the angular spacing between two successive vanes.

Using Eq. (A12), the last two terms on the right hand side of Equation (A15) could be rewritten as:

$$\begin{aligned} & \int_{-b}^{-b+\delta_{lf}} \left[\int_{-\pi/Z}^{+\pi/Z} (\rho V \cos \alpha)_1 d\theta \right] dz + \int_{+b-\delta_{uf}}^{+b} \left[\int_{-\pi/Z}^{+\pi/Z} (\rho V \cos \alpha)_1 d\theta \right] dz \\ &= \frac{2\pi}{Z} (\rho V)_{\infty 1} \cos \alpha_1 \left[\int_{-b}^{-b+\delta_{lf}} \frac{\rho (v + w \tan \alpha_1)}{(\rho V)_{\infty 1}} dz \right. \\ & \quad \left. + \int_{+b-\delta_{uf}}^{+b} \frac{\rho (v + w \tan \alpha_1)}{(\rho V)_{\infty 1}} dz \right] \end{aligned}$$

When Equations (A3) and (A5) are used, the above equation reduces to:

$$\begin{aligned} & \int_{-b}^{-b+\delta_{lf}} \left[\int_{-\pi/Z}^{+\pi/Z} (\rho V \cos \alpha)_1 d\theta \right] dz + \int_{+b-\delta_{uf}}^{+b} \left[\int_{-\pi/Z}^{+\pi/Z} (\rho V \cos \alpha)_1 d\theta \right] dz \\ &= \frac{2\pi}{Z} (\rho V)_{\infty 1} r_1 \cos \alpha_1 [\delta_{lx} + \delta_{ux} - (\delta_{lx} + \delta_{ux}) + (\delta_{lc} + \delta_{uc}) \tan \alpha_1] \quad (A20) \end{aligned}$$

where

δ_{lx}, δ_{ux} are the streamwise boundary layer displacement thicknesses over the lower and upper end walls respectively.

δ_{lc}, δ_{uc} are the cross flow boundary layer displacement thicknesses over the lower and upper end walls respectively.

Finally substituting Equations (A17) and (A20) into (A15) we get:

$$\int_{-b}^{+b} \int_{-\pi/Z}^{\pi/Z} (\rho V r \cos \alpha)_1 d\theta dz = (\rho V)_{\infty 1} \left(\frac{2\pi}{Z} \right) r_1 \cos \alpha_1 [2b - (\delta_{u_f} + \delta_{l_f})] \cdot [1 - \delta_{te}^* + (\delta_{l_f} + \delta_{u_f} - (\delta_{lx} + \delta_{ux}) + (\delta_{lc} + \delta_{uc}) \tan \alpha_1)] \quad (A21)$$

If we define the following nondimensional parameters

$$\theta^{**} = \frac{\theta_{ux} + \theta_{lx}}{2b}, \quad (A22)$$

$$\lambda = H_x - \epsilon K \tan \alpha_1 \quad (A23)$$

where

θ_{ux}, θ_{lx} are the streamwise boundary layer momentum thicknesses over the upper and lower end walls respectively.

Equation (A21) can be simplified by neglecting the higher order terms $(\delta_{u_f} + \delta_{l_f})\delta^*$, $(\delta_{u_f} - \delta_{l_f})\delta_{te}$ and introducing the parameters defined by equations (A8), (A9), (A22) and (A23) giving the following relation:

$$\int_{-b}^{+b} \int_{-\pi/Z}^{+\pi/Z} (\rho V r \cos \alpha)_1 d\theta dz = (\rho V)_{\infty 1} \frac{2\pi}{Z} r_1 \cos \alpha_1 2b [1 - \delta_{te}^* - \lambda \theta^{**}] \quad (A24)$$

A.2.2 Evaluation of the Integral $\int_{-b}^{+b} \int_{-\pi/Z}^{+\pi/Z} (r^2 \rho V^2 \cos \alpha \sin \alpha)_1 d\theta dz$

The evaluation of the integral will be divided over the three same regions discussed previously.

$$\begin{aligned}
& \int_{-b}^{+b} \left[\int_{-\pi/Z}^{+\pi/Z} (r_1^2 \rho V^2 \cos \alpha \sin \alpha)_1 d\theta \right] dz = \{ r_1^2 \cos \alpha_1 \sin \alpha_1 \} [2b - \\
& - (\delta_{u_f} + \delta_{l_f})] \int_{-\pi/Z}^{+\pi/Z} (\rho V^2)_1 d\theta + \left(\frac{2\pi}{Z} r_1^2 \right) \left[\int_{-b}^{-b+\delta_{l_f}} (\rho V^2 \cos \alpha \sin \alpha)_1 dz \right. \\
& \left. + \int_{b-\delta_{u_f}}^b (\rho V^2 \cos \alpha \sin \alpha)_1 dz \right] \quad (A25)
\end{aligned}$$

Using Eqs. (A1), (A2) and (A16) into the first term in the right hand side of Eq. (A25), it reduces to:

$$\begin{aligned}
& \{ r_1^2 \cos \alpha_1 \sin \alpha_1 \} [2b - (\delta_{u_f} + \delta_{l_f})] \int_{-\pi/Z}^{+\pi/Z} (\rho V^2)_1 d\theta \\
& = (\rho V^2)_{\infty_1} \sin \alpha_1 \cos \alpha_1 [2b - (\delta_{u_f} + \delta_{l_f})] \frac{2\pi}{Z} r_1^2 [1 - \delta^* - \delta_{te} - \theta^*] \quad (A26)
\end{aligned}$$

where

$$\theta^* = (\theta_s + \theta_p) / \frac{2\pi}{Z} r_1 \cos \alpha_1 \quad (A27)$$

and

θ_s and θ_p are the boundary layer momentum thickness on the vane suction and pressure surfaces respectively.

When Eqs. (A13), (A4) and (A6) are substituted into the second and third term of (A25), it can be deduced that:

$$\int_{-b}^{-b+\delta_{l_f}} (\cos \alpha \sin \alpha \rho V^2)_1 dz = (\rho V^2)_{\infty_1} \cos \alpha_1 \sin \alpha_1 [\delta_{lf} - \delta_{lx} - \theta_{lx} - \theta_{lc}] \quad (A28)$$

and

$$\int_{b-\delta_{uf}}^b (\cos\alpha \sin\alpha \rho V^2)_1 dz = (\rho V^2)_{\infty 1} \cos\alpha_1 \sin\alpha_1 [\delta_{uf} - \delta_{ux} - \theta_{ux} - \theta_{uc}] \quad (A29)$$

where

θ_{uc} and θ_{lc} are the cross flow boundary layer momentum thickness over the upper and lower end walls, respectively.

Finally, substituting Equations (A26), (A28) and (A29) into (A25) and making use of the parameters given by (A8) and (A10) the integral of equation (4) is expressed as follows:

$$\int_{-b}^{+b} \left[\int_{-\pi/Z}^{+\pi/Z} (r^2 \rho V^2 \cos\alpha \sin\alpha)_1 d\theta \right] dz = (\rho V^2)_{\infty 1} \sin\alpha_1 \cos\alpha_1 \frac{2\pi}{Z} r_1^2 2b \cdot [1 - \delta^* - \delta_{te}^* - \theta^* - \eta \theta^{**}] \quad (A30)$$

where

$$\eta = 1 + H_x + \epsilon^2 L \quad (A31)$$

A.2.3 Evaluation of the Integral $\int_{-b}^{+b} \left[\int_{-\pi/Z}^{+\pi/Z} (\rho V^2 \cos\alpha r \cos(\alpha+\theta))_1 d\theta \right] dz$

Using trigometric relations the above integral may be expanded as follows:

$$\begin{aligned} \int_{-b}^{+b} \left[\int_{-\pi/Z}^{+\pi/Z} (\rho V^2 r \cos\alpha \cos(\alpha+\theta))_1 d\theta \right] dz &= \int_{-b}^{+b} \left[\int_{-\pi/Z}^{+\pi/Z} (\rho V^2 r \cos^2\alpha)_1 \cos\theta d\theta \right] dz \\ &- \int_{-b}^{+b} \left[\int_{-\pi/Z}^{+\pi/Z} (\rho V^2 r \cos\alpha \sin\alpha)_1 \sin\theta d\theta \right] dz \end{aligned} \quad (A32)$$

The first integral in the right hand side of Equation (A32) may be rewritten as:

$$\begin{aligned}
& \int_{-b}^{+b} \left[\int_{-\pi/Z}^{+\pi/Z} (\rho V^2 r \cos^2 \alpha)_1 \cos \theta \, d\theta \right] dz = \{r_1 \cos^2 \alpha_1\} \{[2b - \delta_{u_f} - \\
& - \delta_{\ell_f}] \int_{-\pi/Z}^{+\pi/Z} (\rho V^2)_1 \cos \theta \, d\theta\} + r_1 \left\{ \int_{-\pi/Z}^{+\pi/Z} \left[\int_{-b}^{-b+\delta_{\ell_f}} (\rho V^2 \cos^2 \alpha)_1 \cos \theta \, dz \right] d\theta \right. \\
& \left. + \int_{-\pi/Z}^{+\pi/Z} \left[\int_{b-\delta_{u_f}}^b (\rho V^2 \cos^2 \alpha)_1 \cos \theta \, dz \right] d\theta \right\} \quad (A33)
\end{aligned}$$

For unseparated flows, the angular coordinate, θ , does not change appreciably inside the boundary layers formed over the vane surfaces. Consequently, θ , can be considered equal to the angular spacing, π/Z , within these boundary layer regions. Using this value of θ together with Equation (A2), it can be easily deduced that:

$$\int_{-\pi/Z}^{+\pi/Z} (\rho V^2)_1 \cos \theta \, d\theta = -(\rho V^2)_{\infty 1} \cos \frac{\pi}{Z} \left(\frac{\theta_s + \theta_p}{r_1 \cos \alpha_1} \right) + V_{fs1} \int_{-\pi/Z}^{+\pi/Z} (\rho V)_1 \cos \theta \, d\theta \quad (A34)$$

Using the definition of the displacement thickness given by Equation (A1), the second term in the right hand side of Equation (A34) reduces to:

$$\int_{-\pi/Z}^{+\pi/Z} (\rho V)_1 \cos \theta \, d\theta = \frac{2\pi}{Z} (\rho V)_{\infty 1} \left[\frac{\sin \pi/Z}{\pi/Z} - \cos \frac{\pi}{Z} (\delta^* + \delta_{te}) \right] \quad (A35)$$

If Equation (A35) is substituted into (A34) the following relation can be written:

$$\int_{-\pi/Z}^{+\pi/Z} (\rho V^2)_1 \cos \theta \, d\theta = \frac{2\pi}{Z} (\rho V^2)_{\infty 1} \left[\frac{\sin \pi/Z}{\pi/Z} - \cos \frac{\pi}{Z} (\delta^* + \delta_{te} + \theta^*) \right] \quad (A36)$$

Using Equations (A14), (A4) and (A6), the integrals in the right hand side of (A33) reduce to:

$$\int_{-\pi/Z}^{+\pi/Z} \int_{-b}^{-b+\delta_{\ell f}} (\rho V^2 \cos^2 \alpha)_1 \cos \theta \, dz d\theta = 2 \sin \frac{\pi}{Z} \cos^2 \alpha_1 (\rho V^2)_{\infty 1} (\delta_{\ell f} - \delta_{\ell x} - \theta_{\ell x} + \theta_{\ell c} \tan^2 \alpha_1) \quad (A37)$$

$$\int_{-\pi/Z}^{+\pi/Z} \int_{+b-\delta_{u_f}}^{+b} (\rho V^2 \cos^2 \alpha)_1 \cos \theta \, dz d\theta = 2 \sin \frac{\pi}{Z} \cos^2 \alpha_1 (\rho V^2)_{\infty 1} (\delta_{\ell f} - \delta_{u_x} - \theta_{u_x} + \theta_{u_c} \tan^2 \alpha_1) \quad (A38)$$

Substituting Equations (A36), (A37) and (A38) into the right hand side of (A33), we arrive at:

$$\int_{-b}^{+b} \left[\int_{-\pi/Z}^{+\pi/Z} (\rho V^2 r \cos^2 \alpha)_1 \cos \theta \, d\theta \right] dz = 2b \frac{2\pi}{Z} r_1 \cos^2 \alpha_1 (\rho V^2)_{\infty 1} \frac{\sin \frac{\pi}{Z}}{\frac{\pi}{Z}} [1 - \theta^{**} (1 + H_x - \epsilon^2 L \tan^2 \alpha_1)] - \cos \frac{\pi}{Z} (\delta^* + \delta_{te} + \theta^*) \quad (A39)$$

where H_x , $\epsilon^2 L$ are given by the Equations (A8) and (A10).

Following a procedure similar to the one used to obtain equation (A39), it may be easily deduced that:

$$\int_{-b}^{+b} \left[\int_{-\pi/Z}^{+\pi/Z} (\rho V^2 r \cos \alpha \sin \alpha)_1 \sin \theta \, d\theta \right] dz = 0 \quad (A40)$$

Finally, substituting Equations (A39), (A40) into (A33), the required value of the integral in Equation (6) is obtained as:

$$\int_{-b}^{+b} \int_{-\pi/Z}^{+\pi/Z} [\rho V^2 \cos \alpha \, r \cos(\alpha + \theta)]_1 \, d\theta \, dz = 2b (\rho V^2)_{\infty 1} \cos^2 \alpha_1 \frac{2\pi}{Z} r_1 \cdot \left[\frac{\sin \frac{\pi}{Z}}{\frac{\pi}{Z}} (1 - \Gamma \theta^{**}) - \cos \frac{\pi}{Z} (\delta^* + \delta_{te} + \theta^*) \right] \quad (A41)$$

where

$$\Gamma = 1 + H_x - \epsilon^2 L \tan^2 \alpha_1 \quad (A42)$$

Equations (A24), (A30) and (A41) will be used in equations (2), (4) and (6) to express the continuity, the angular momentum and the linear momentum equations in terms of the boundary layer characteristic parameters at station 1.

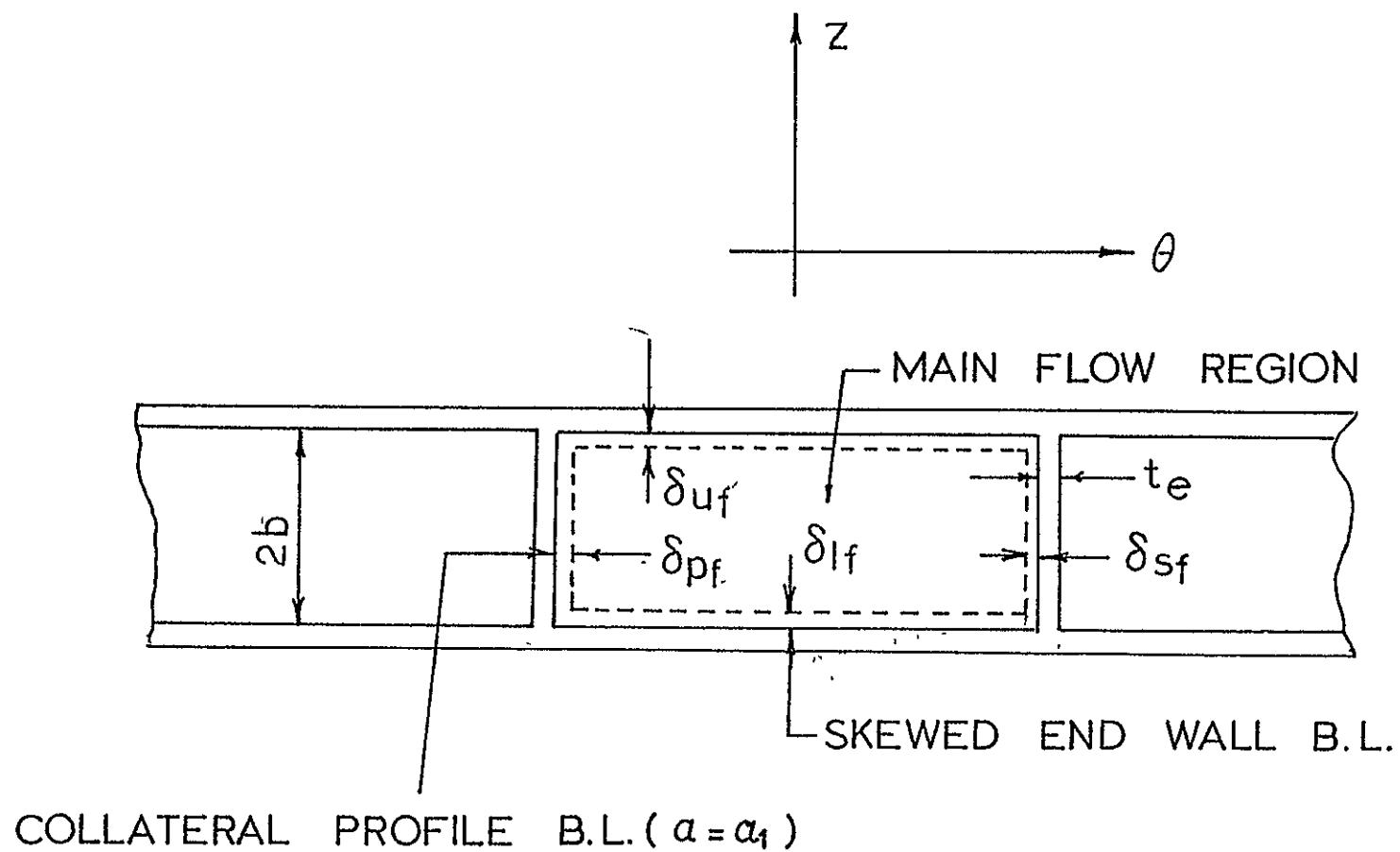


FIG A-1 FLOW REGIONS AT EXIT FROM THE NOZZLE CHANNEL.

FIG. A-2 NOMENCLATURE AND SYMBOLS AT VANES TRAILING EDGE

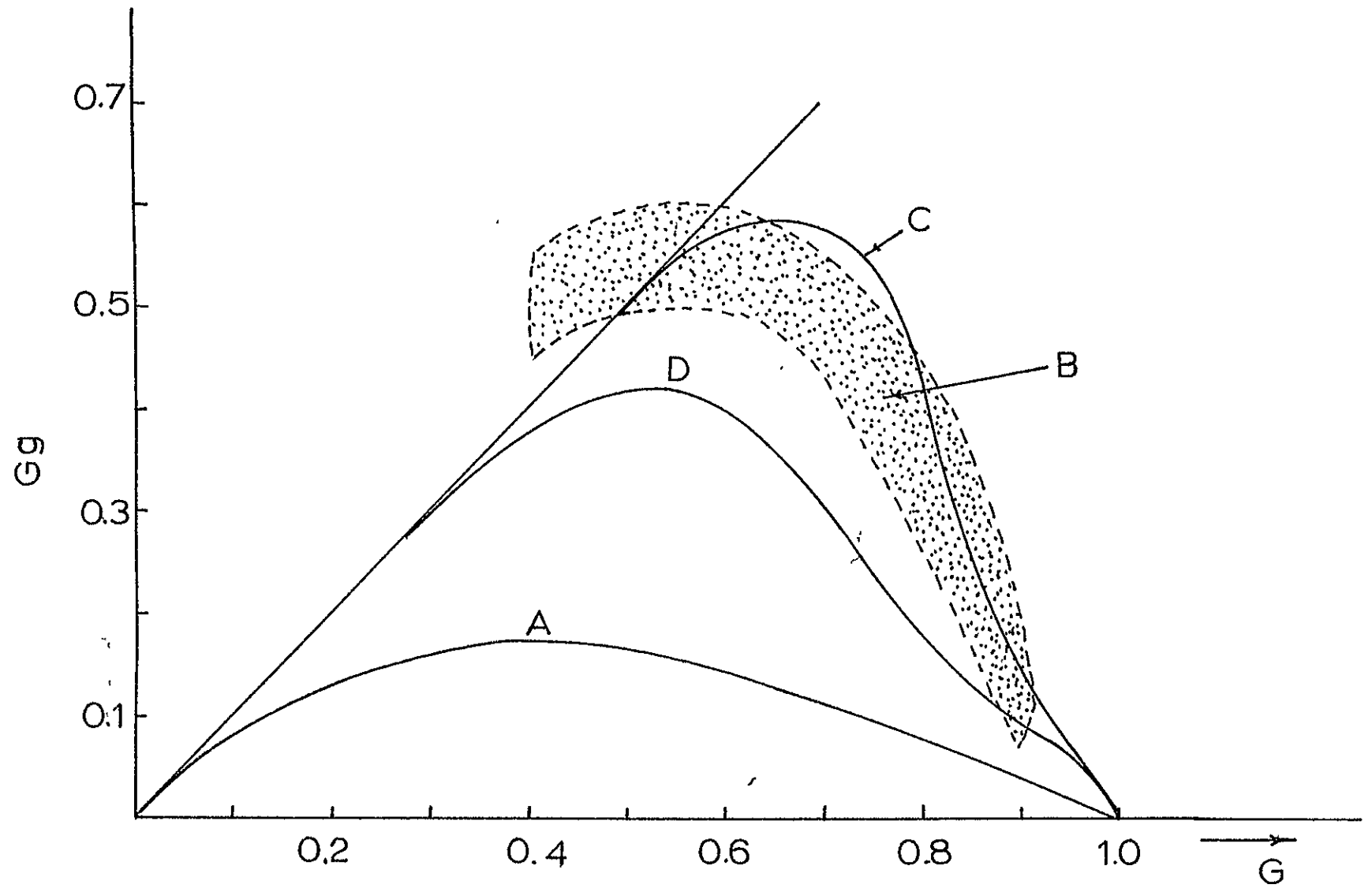


FIG A-3 NORMALISED CROSS FLOW PROFILES

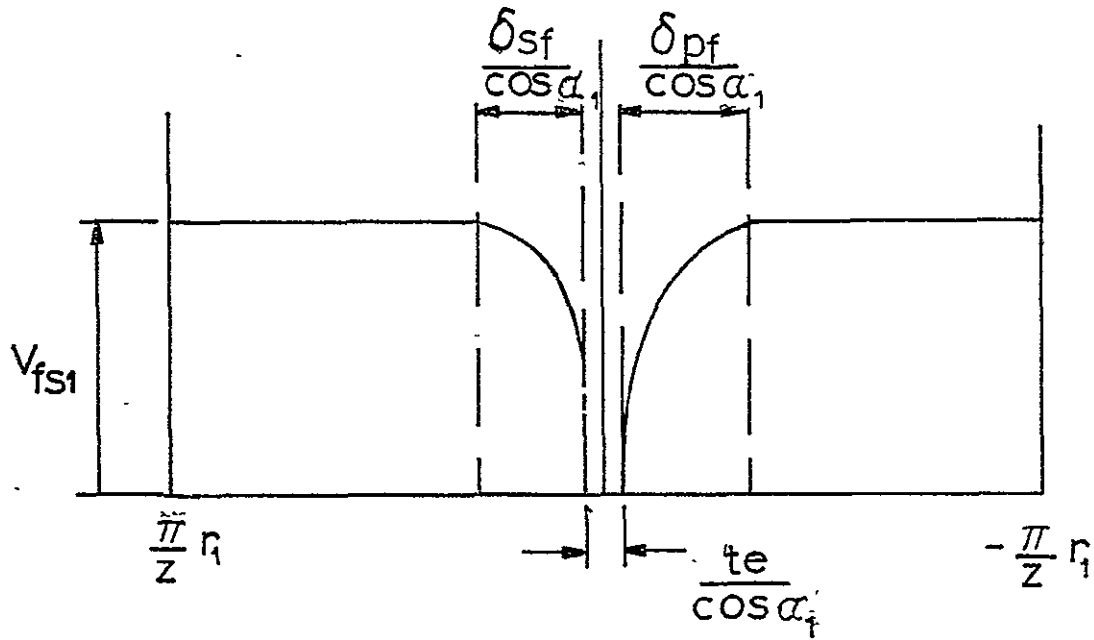


FIG. A-4 : TYPICAL VELOCITY DISTRIBUTION IN CIRCUMFERENTIAL DIRECTION AT NOZZLE EXIT,

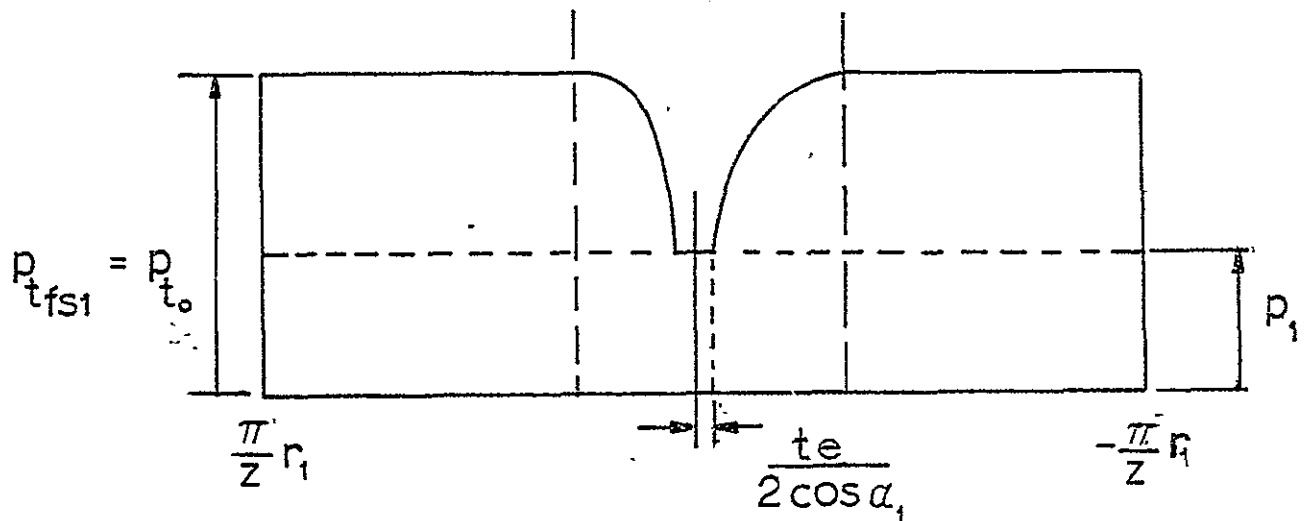


FIG. A-5: TYPICAL PRESSURE DISTRIBUTION IN CIRCUMFERENTIAL DIRECTION AT NOZZLE EXIT.

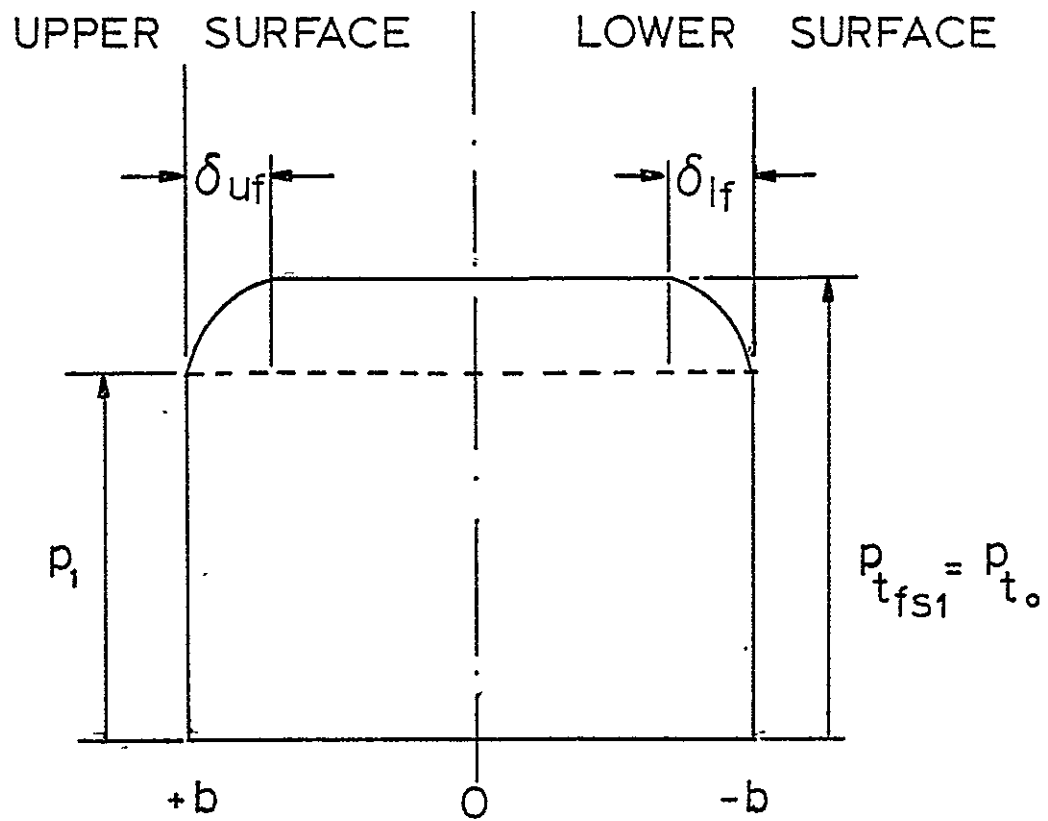


FIG.A-6: TYPICAL TOTAL PRESSURE DISTRIBUTION IN AXIAL DIRECTION AT NOZZLE EXIT.

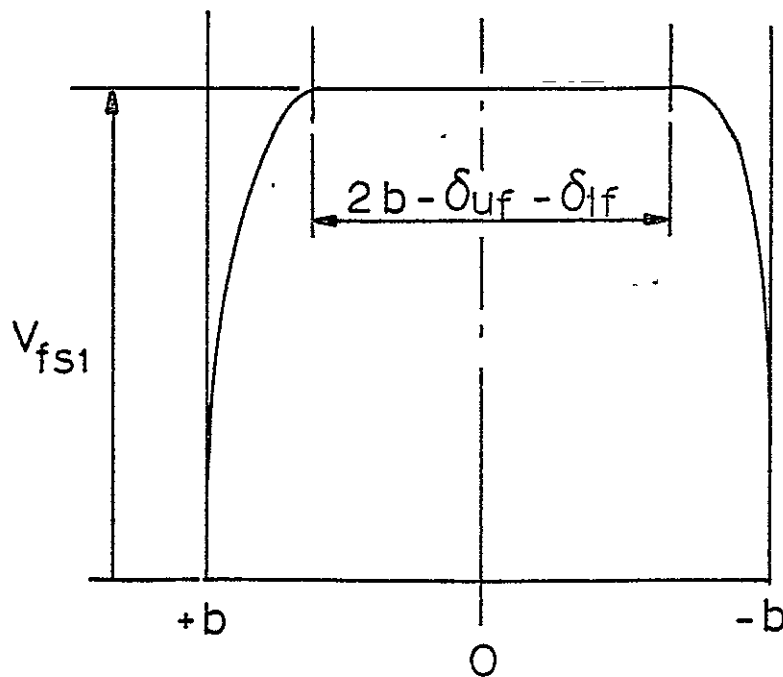


FIG. A-7 TYPICAL VELOCITY DISTRIBUTION IN AXIAL DIRECTION AT NOZZLE EXIT.